The physics of simple metal clusters: experimental aspects and simple models

Walt A. de Heer

Institut de Physique Expérimentale, Ecole Polytechnique Fédérale de Lausanne, Lausanne CH-1015, Switzerland

The study of simple metal clusters has burgeoned in the last decade, motivated by the growing interest in the evolution of physical properties from the atom to the bulk solid, a progression passing through the domain of atomic clusters. On the experimental side, the rapid development of new techniques for producing the clusters and for probing and detecting them has resulted in a phenomenal increase in our knowledge of these systems. For clusters of the simplest metals, the alkali and noble metals, the electronic structure is dominated by the number of valence electrons, and the ionic cores are of secondary importance. These electrons are delocalized, and the electronic system exhibits a shell structure that is closely related to the well-known nuclear shell structure. In this article the results from a broad range of experiments are reviewed and compared with theory. Included are the behavior of the mass-abundance spectra, polarizabilities, ionization potentials, photoelectron spectra, optical spectra, and fragmentation phenomena.

CONTENTS

 0034-6861/93/65(3)/611(66)/$11.60

I. INTRODUCTION

In this age of miniaturization of electronic devices, there is an increasing need to understand the properties of metallic structures with dimensions of the order of nanometers. Metal clusters are particles composed of a countable number of atoms, starting with the diatomic molecule and reaching, with a vaguely defined upper bound of several hundred thousand atoms, into that interesting size range.

Metal clusters are not new. In fact, the glaziers of the Middle Ages discovered how to produce beautiful stained glasses by special treatments of metal-containing glasses. In fact, the earliest investigations are perhaps due to Rayleigh, who recognized that the colors of stained glasses were due to the scattering of light by small metal particles embedded in the glass. His work was followed by an extensive electrodynamic treatment by Mie (1908), which is relevant even today. From those early investigations through the 1970s, much of the metal cluster work concentrated on related systems, where small metal particles were precipitated in glasses and investigated for their electromagnetic properties (Kreibig, 1970).

During the 1960s and 1970s, new cluster sources were developed to produce clusters composed of only a few atoms in the gas phase (Robbins *et al.*, 1967). It seemed that these particles had properties that were unrelated to the bulk. This might be expected from either a molecular or a solid-state point of view, since for these very small particles the surface is important. Even for a cluster with 1000 atoms, about a quarter of the atoms lie on the surface, so that its properties may be importantly modified compared with the bulk.

Because of the large fraction of surface atoms, it is clear that when the cluster is embedded in a matrix of some kind, additional complexity is introduced. Hence an understanding of the properties of isolated clusters of well-defined size in the gas phase is an essential first step towards a description of embedded clusters, which some day may well be of technological importance. These considerations lead to several pioneering investigations giving birth to the now very rich field of cluster physics.

Up to the early 1980s clusters were primarily thought of as small molecules. There was little reason to expect patterns relating the properties of clusters with different sizes or of different metals; as for molecules, every cluster was considered to be essentially unique. In those days the most carefully studied clusters were indeed very small, with at most about a dozen atoms, and no obvious order was discerned. Much larger particles were believed to be essentially bulklike, and the surface was thought to scatter electrons randomly. Hence complex molecular electronic structure was expected to give way to bulk structure, where the increasing complexity ultimately warranted a statistical description (Kubo, 1962).

However, this changed in late 1983 when Walter Knight's group, with Keith Clemenger, Walt de Heer, and Winston Saunders, produced and detected clusters of alkali metals with up to about 100 atoms. They immediately recognized that there was a striking order: the electronic structure of these clusters appeared to reflect that of a spherical potential well (Knight *et al.*, 1984). This fundamental principle was inferred from little more than the cluster abundance spectra: clusters in which the number of valence electrons matched the spherical shell-closing numbers were produced more abundantly, as seen in Fig. 1. By a striking coincidence, Ekardt (1984a, 1984b) independently and virtually simultaneously predicted this shell structure in his model for alkali clusters using the jellium approach, in which the clusters are considered to be uniformly positively charged spheres filled with electrons. Earlier, Martins *et al.* (1981) also had recognized similarities between the electronic orbitals from a molecular calculation with those from a jellium picture.

We now know that these characteristic abundance patterns persist up to very large sizes: electronic shell structure is observable even for clusters with several thousand atoms, as recently made evident by Sven Bjørnholm and his collaborators (Pedersen *et al.*, 1991) and by other groups.

After those early discoveries, electronic shell structure was observed in many simple and noble-metal cluster systems. The initial observations of the electronic shell structure and the theoretical development of the shell model have been reviewed by de Heer, Knight, *et al.* (1987). From then on the development was rapid. Experimentally the electronic shell structure was verified in the electronic response properties (ionization potentials, polarizabilities, collective excitations, etc.), and the jellium model was further developed to a high degree of sophistication.

However, a sphere is a reasonable approximation only for electronically closed-shell clusters. For open-shell clusters the spherical shape is unstable towards distortions due to the Jahn-Teller effect (Jahn and Teller, 1937),

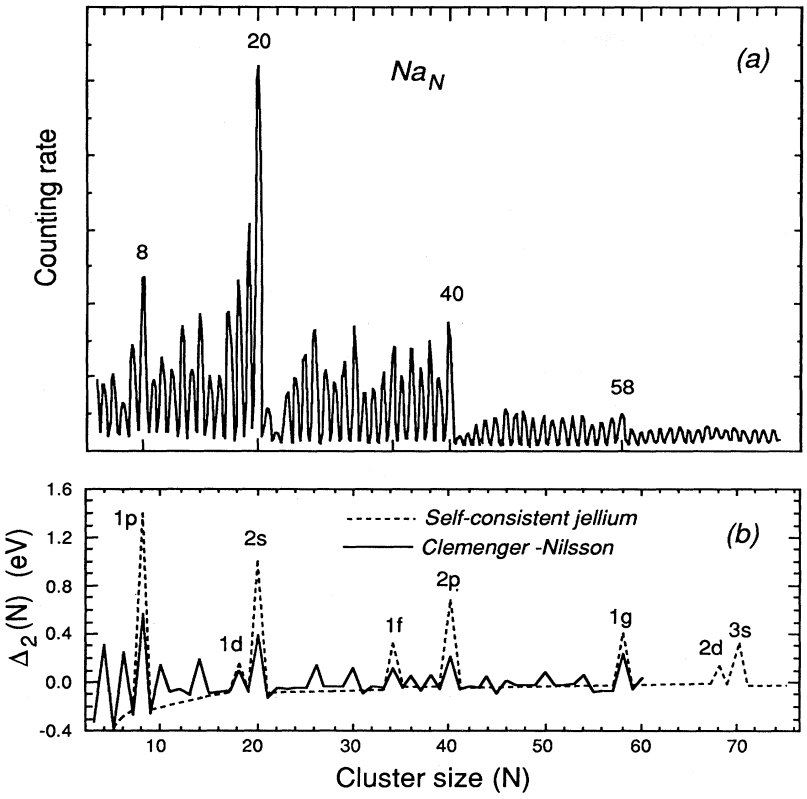

FIG. 1. Sodium cluster abundance spectrum: (a) experimental (after Knight *et al.*, 1984); (b) dashed line, using Woods-Saxon potential (after Knight *et al.*, 1984); solid line, using the ellipsoidal shell (Clemenger-Nilsson) model (after de Heer, Knight, Chou, and Cohen, 1987).

which has important and readily observable consequences. More recent self-consistent models now take this into account, but it was already recognized by Clemenger (1985a, 1985b). Noting that a very similar situation existed for nuclei, he adapted the deformed nuclear shell model of Nilsson (1955) to alkali clusters and found that virtually all the fine structure in the spectrum of Fig. 1 could be related to predictions from this model.

The experimental fact that to first order the detailed ionic core structure is not as important, and that the electrons may be considered to be nearly free and confined in a potential well, can be exploited at various levels. In the self-consistent jellium model, the ionic cores are considered to provide a uniformly charged positive background, and the electronic structure is subsequently calculated using various approximations for the interacting electron gas. However, even thus simplified the many-body problem is still far from trivial, as evidenced by the vast literature based on the jellium model alone. At a much lower level are the "hook and crook" approaches so dear to experimentalists who usually cannot wait for accurate theoretical predictions. For metal clusters, in particular, these have been extremely useful for providing very reasonable first-order interpretations of experimental data. In this review we shall heavily rely on descriptions of this kind. There is no intended implication that these methods can provide much more than rudimentary descriptions. Nevertheless, very often when conceiving and developing an experiment, all the experimentalist wants is a basic understanding of the physical properties involved, with reasonable quantitative estimates.

The review projects an experimentalist's point of view and attempts to present as clear a picture as possible of the experimental situation. However, rather than presenting a dry summary of experimental results, I have tried to unify them as much as possible by relating the observations with the simplest possible models. Of course this has the risk of trivializing the enormously complex many-body problem, which these clusters, after all, represent. I emphasize that this is by no means my intention. The models presented here serve the same purpose they do in all branches of physics, that is, to organize the experimental observations and to establish elementary relationships between observed effects at the most basic level.

Section II introduces the basic concepts of the electronic shell model based on the Clemenger-Nilsson model, and predictions of this model are compared with experiment throughout. I believe that this model and its concepts are so important that it warrants this degree of attention. Details of the model with several applications are given in the appendices. General experimental techniques are reviewed in Sec. III. The discussion is continued with six more or less self-contained sections, each one treating a specific cluster property (Secs. IV–IX). In each of these sections the experimental data are presented, discussed, and compared both with simple models and with detailed calculations.

A serious attempt has been made to touch on the most important developments in the field, but the review is by

no means exhaustive. Often when earlier experimental results have been refined or appended with newer ones, only the more current results are explicitly mentioned, with the understanding that the development can be traced from the cited work. By no means is any judgment on the importance of the earlier work implied. I apologize for any instances in which work was overlooked. Furthermore, in order to achieve as uniform a presentation as possible, figures have often been redrawn from published data, thereby introducing slight distortions. For accurate values, the reader is urged to consult the original figures.

Theory is treated only peripherally. In fact the review originally consisted of two parts, an experimental and a theoretical one. It was decided, however, that it is more reasonable to have two complementary reviews. The theoretical counterpart by Matthias Brack (1993) treats the theory of simple metal clusters in detail and follows this review.

This work covers only one aspect of the vast field of cluster science. For a brief but wide-ranging overview, the reader should consult the recent (although not completely up-to-date) review by Sugano (1991). Among other things, that work treats metal, semiconductor, molecular, and inert-gas clusters. Other invaluable sources of information on all aspects of cluster physics are the proceedings of the ISSPIC conferences (International Symposium on Small Particles and Inorganic Clusters), held at Lyon in 1976 (ISSPIC 1, 1977), at Lausanne in 1980 (ISSPIC 2, 1981), at Berlin in 1984 (ISSPIC 3, 1985), at Aix-en-Provence in 1988 (ISSPIC 4, 1989), at Konstanz in 1990 (ISSIPC 5, 1991), and at Chicago in 1992 (ISSPIC 6, 1983). Additional sources are the proceedings of two conferences at Richmond in 1986 and 1991 (Jena, Rao, and Khanna, 1987; Jena, Khanna, and Rao, 1992). Reviews relating to topics discussed in this work are cited in the text.

II. SHELL MODEL FOR SIMPLE METAL CLUSTERS

For monovalent simple metals, the conduction band is approximately free-electron-like and the Fermi surface is nearly spherical. For sodium, in particular, deviations from a perfect sphere are almost negligible (Ashcroft and Mermin, 1976). Correspondingly, the jellium model ignores the ionic core structure altogether and replaces it by a uniform positive background, and this approach has led to valuable insights into the electronic structure of bulk metals. Surfaces clearly require special attention. However, even assuming that the positive charge abruptly terminates at the surface gives reasonable predictions for electronic properties (Lang and Kohn, 1971). The advantages are obvious, leading to a much more manageable description than one which accounts for the ionic structure in detail.

These considerations motivate the jellium model for metal clusters. Despite the obvious objections that can be raised against such a description, especially for clusters containing only a few atoms, the results are nevertheless impressive. The jellium model for clusters is extensively treated in the theoretical counterpart of this review (Brack, 1993).

We now depart from the jellium model and develop a related semiempirical model, which is used throughout this review. This is a vastly simpler approach and is based essentially on the Sommerfeld model (Ashcroft and Mermin, 1976). In contrast with the jellium calculations, in which the electrons are treated self-consistently, the model takes for granted that a very simple effective single-particle potential (for example, a rounded spherical square well) is a good starting point.

Our aim is to obtain a qualitative description of the properties of the simple metal clusters so that properties can be calculated with a minimum of effort. Not only is this useful when reasonable quantitative values are required, but it also provides invaluable insight into the fundamental physics involved. Detailed explanations are given in the appendices, where a variety of properties are treated explicitly. Here we give only the principle ideas and establish points of contact with sophisticated calculations to give insight into the accuracy that may be expected from this model.

A. Shell model for spherical clusters

The mass-abundance spectrum in Fig. 1 suggests that to lowest order the valence electrons in sodium clusters are independent and are confined in a spherically symmetric potential. Such a potential automatically gives rise to spherical shell structure because of its symmetry, where the valence electrons successively fill the degenerate levels. As for atoms, the electronic system of a cluster with exactly the right number of electrons to complete a shell is very stable. When one more atom is added to the cluster, its valence electron will occupy a state with considerably higher energy, and hence the stability of the cluster is reduced. The reduced stability is reflected in a reduced abundance, explaining the large abundance drops after each shell-closing number in Fig. 1.

In metal cluster physics the quantum numbers follow the nuclear (i.e., not the atomic) convention, so that each shell is characterized by the radial quantum number n and the angular momentum l. For a given quantum number l, the lowest state has $n=1$, etc. Figure 2 shows the energy-level structure for three spherically symmetric wells, and it can be seen that changing the well shape not only changes the relative level spacings, but may even alter their ordering.

For comparison, Fig. 3 shows the calculated self-consistent effective single-particle potential for Na_{40} (Chou *et al.*, 1984; further examples are given by Ekardt, 1984a). The energy levels are also shown and the shell structure is clearly discernable. This particular self-consistent potential well has the shape of a wine bottle, and the energy-level spacings approximately correspond

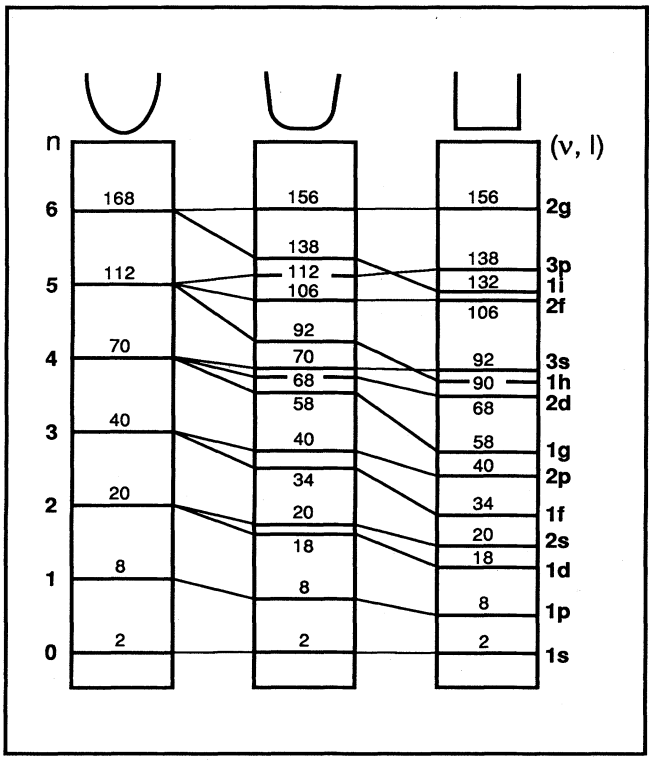

FIG. 2. Energy-level occupations for spherical three-dimensional, harmonic, intermediate, and square-well potentials. After Mayer and Jensen, 1955.

to those of the intermediate case in Fig. 2. Further, the shape of the well (as determined in the jellium model) depends on the cluster in question; however, the energy levels from one closed-shell cluster to the next are found to be closely related.

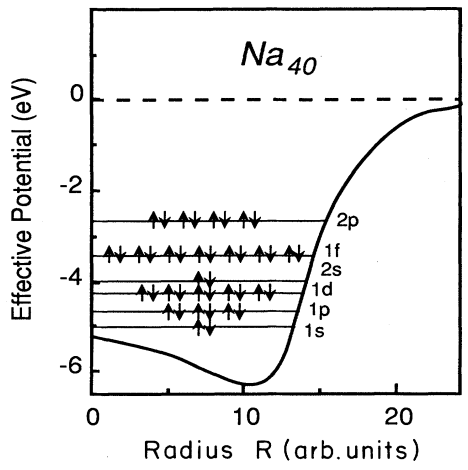

FIG. 3. Self-consistent effective potential of jellium sphere corresponding to Na_{40} with the electron occupation of the energy levels. After Chou *et al.*, 1984.

B. Ellipsoidal Clemenger-Nilsson shell model

Approximating small clusters with spheres can be only be justified for closed-shell clusters. From the Jahn-Teller theorem (Jahn and Teller, 1937) it follows that open-shell clusters must distort. As demonstrated by Clemenger (1985a, 1985b), the fine structure in Fig. 1(a) is a manifestation of these distortions. Clemenger introduced a deformable potential well that is particularly well suited to account for this effect. In fact, he simply adapted the well-known Nilsson model extensively used to estimate the shapes of nuclei (see, for example, Bohr and Mottelson, 1975).

The Clemenger-Nilsson model assumes that the effective single-particle potential is essentially that of a three-dimensional harmonic oscillator. This turns out to be a remarkably good approximation for smaller clusters (i.e., $N<20$). For larger ones, a small anharmonic distortion term is required; however, for most of the analyses here we ignore this refinement, so that the calculations become so simple that they are easily done analytically (Appendix A).

An important feature of the model is that its shape adjusts to the electronic structure while keeping the volume of the cluster fixed. In this way spheroidal clusters (i.e., with two equal axes $R_x=R_y$ and one unequal axis R_z) can be treated; details are given in Appendix A. From this model it is found that the shapes of open-shell clusters are significantly distorted. The cluster shapes and energy-level structure are represented in the Clemenger-Nilsson diagram (Appendix A, Fig. 53).

As in the spherical shell model, the spheroidal shell model predicts enhanced stabilities for closed-shell clusters. However, in addition, the spheroidal distortions cause subshell closings which are also seen in the spectra. Hence this model reproduces not only the main features but also most of the fine structure in the abundance spectrum, as shown in Fig. 1(b). Other features, for example, the abundance maximum at 12, are found in the ellipsoidal Clemenger-Nilsson model, which allows distortions along all three axes of the cluster (see below).

In Sec. IV.A.1 the relation between the abundance spectra and electronic stabilities is treated more carefully. Here we note that the correspondence provides empirical evidence that *to lowest order the fine structure is often caused by the overall shape of the cluster,* and in particular it is not necessarily due to the detailed arrangement of the ionic cores. This surprising property is the basis for the jellium model for metal clusters.

1. Cluster shapes in the ellipsoidal shell model

It is straightforward to extend the Clemenger-Nilsson model by allowing distortions along three axes. Now the shapes are either spheres, spheroids, or ellipsoids, as can be calculated with little effort (ignoring the anharmonic terms, Appendix A).

The cluster shapes are shown in Fig. 4(a) and are readi-

ly rationalized. For example, the atom and dimer are spherical, since only s states are occupied. The tetramer is prolate, since the p_x state is doubly occupied, and the p_x energy is reduced by elongating the cluster in the x direction. Continuing, the 5- and 6-mer are disk shaped, since now both the p_x and p_y states are filled. The 7-mer is the first three-dimensional cluster, since the p_z orbital is singly occupied, followed by the spherical 8-mer with a completely filled $1p$ shell. The midshell crossover from prolate to oblate shapes also occurs as the $1d$ shell fills.

These shapes can be compared with those from theory. We only mention that the self-consistent spheroidal jellium model (Ekardt and Penzar, 1988) and the self-consistent ellipsoidal jellium model (Lauritsch *et al.*, 1991) produce shapes that agree almost exactly with the ellipsoidal shell model.

It is perhaps more relevant to compare the ellipsoidal shell-model shapes with those in which the ionic cores are included. In a particularly simple model, Wang *et al.* (1987) and Lindsay *et al.* (1987) calculated the cluster electronic structure and geometries in the Hückel model and found reasonable correspondence with the jellium model. More accurate molecular calculations, by Martins *et al.* (1985), Moullet *et al.* (1990; Moullet and Martins, 1990), and Bonacic-Koutecky *et al.* (1988), predict geometries depicted in Fig. 4(b), which qualitatively show several of the features mentioned above. Note, for example, the trends: 5 and 6 are planar (although for 6 a slightly nonplanar isomer is also found) and 7 and 8 are three dimensional, while 8 is quite spherical. For 4 the ionic geometry is an elongated planar structure, but one can image the p_x electrons as describing a prolate shape.

Recently Röthlisberger and Andreoni (1991) calculated the structure of small sodium clusters using the molecular-dynamics method developed by Car and Parrinello (1985). Their shapes agree with those from quantum-chemical calculations. Furthermore, Röthlisberger and Andreoni (1991) compared the moments of inertia of the cluster shapes from their calculations with those from the ellipsoidal shell model and found that the two agreed reasonably well.

Although it is difficult to determine cluster shapes experimentally, optical response properties (Sec. VIII) appear to confirm the approximate sphericity of closed-shell clusters and the nonspherical shapes of open-shell clusters.

2. Energy-level structure

The energy levels of the sodium clusters calculated in the ellipsoidal shell model (i.e., with two equivalent axes and one inequivalent axis) are shown in Fig. 5(a) (again the anharmonic term is ignored). The levels have been uniformly shifted (since the vacuum level is not defined in this model). Note that in several cases the level splittings due to deformations are so great (for example, for 12, 13, and 16) that the spherical shell structure is barely discernable.

Comparing the ellipsoidal shell-model levels with those from the molecular-dynamics calculations [Fig. 5(d)] shows similarities in the overall structure. There are some important differences, however, one being that in the molecular-dynamics calculations the spherical shell levels of the 8-mer are split. This is due to ionic core effects not included in the jellium model. The model is further compared with the (electronically) self-consistent

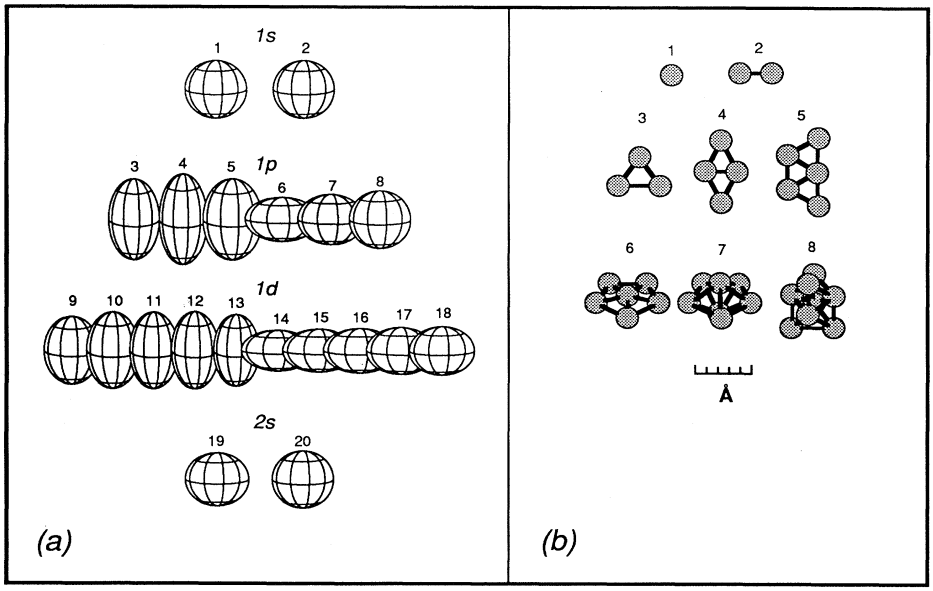

FIG. 4. Cluster shapes (a) according to the ellipsoidal shell model (Clemenger-Nilsson), normalized to the constant volume; (b) from *ab initio* quantum-chemical calculations by Bonacic-Koutecky *et al.* (1988). The midshell change from prolate to oblate predicted in the CN model is also seen in the shapes from *ab initio* calculations.

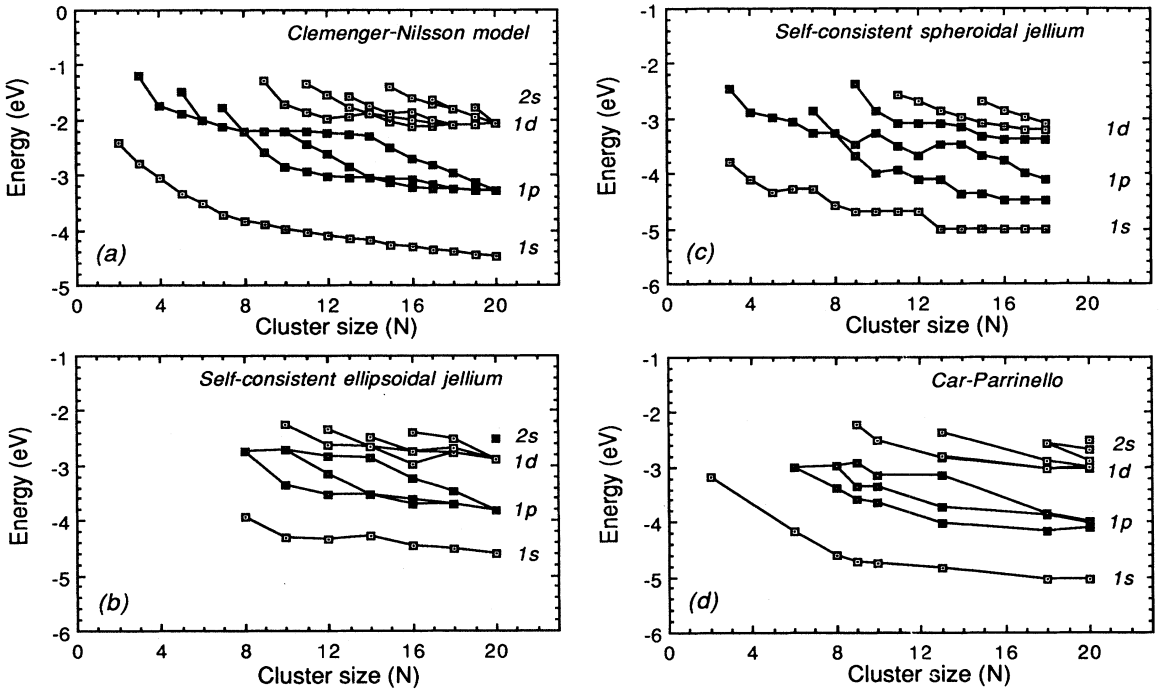

FIG. 5. Single-particle levels of sodium clusters as calculated in various models: (a) the ellipsoidal shell (Clemenger-Nilsson) model; (b) the self-consistent ellipsoidal jellium model (Lauritsch *et al.*, 1991); (c) the self-consistent spheroidal jellium model (Ekardt and Penzar, 1988); and (d) from molecular-dynamics calculations in the local-density approximation (Röthlisberger and Andreoni, 1991).

spheroidal jellium model [Fig. 5(c), Ekardt and Penzar, 1988] and the self-consistent ellipsoidal jellium model (Lauritsch *et al.*, 1991). Agreement is surprisingly good; however, note that the shell-model energy scale is systematically too large. This can be corrected in first order as shown in Appendix A.1.

The electronic energy-level structure found from photoelectron spectra of potassium clusters qualitatively agrees with those in the shell model as shown in Sec. VII.C.1 and in more detail in Appendix C.

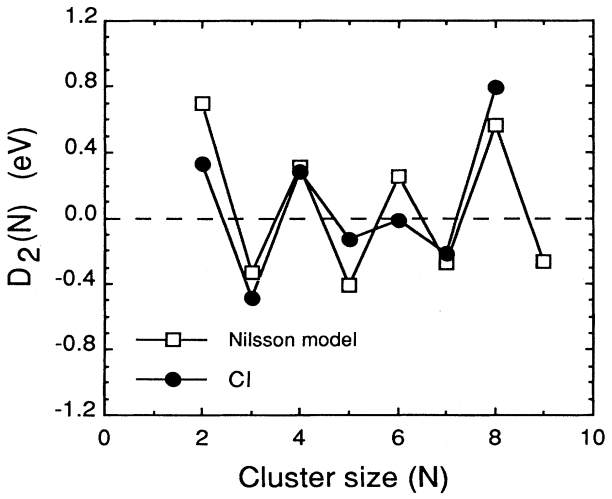

FIG. 6. The second differences in the total energies of sodium clusters: (a) from the CN model, and (b) from quantum-chemical calculations by Bonacic-Koutecky *et al.* (1988).

3. Cluster binding energies

The ellipsoidal shell model does not predict binding energies. However, binding-energy differences may be approximated by the differences in the total electronic energies E_N. In particular, the second differences of the total energies $D_2(N)=2E_N-E_{N-1}-E_{N+1}$ turns out to be quite useful in analyses of mass spectra (see Sec. IV), as, for example, in Fig. 1.

Figure 6 shows the $D_2(N)$ for small sodium clusters as determined from the ellipsoidal shell model and those from quantum-chemical calculations (Bonacic-Koutecky *et al.*, 1991). Again the correspondence is reasonable.

C. Conclusion

In this brief exposition we have shown that simple models, and the ellipsoidal extension of the Clemenger-Nilsson model in particular, admirably reproduce many of the features from much more sophisticated theories. This is certainly a surprising result, especially for very small clusters. We shall not dwell on the reasons, but may safely assume that the ellipsoidal shell model is a very good starting point for understanding the properties of simple metal clusters. This model will be used exten-

sively and will be referred to as the ellipsoidal shell model without further specification.

III. EXPERIMENTAL TECHNIQUES

Progress in cluster physics closely follows the development of new experimental methods. Important advances in production and detection techniques for metal clusters in molecular beams provide the possibility of studying clusters in an interaction-free environment. Consequently, the experimental probes are closely related to methods traditionally used for atomic and molecular studies.

Atomic and molecular beams have been used over the better part of this century, and great progress has been made in their production and detection. (For an excellent recent review treating a wide variety of molecular-beam methods, see Scoles, 1988 and the classic work of Ramsey, 1969.) Nevertheless, there are many aspects particular to clusters that require specific attention. At present, cluster beams of virtually any element (with from several up to several tens of thousands of atoms per cluster) are routinely produced and analyzed.

All molecular-beam experiments on clusters have a cluster source and a cluster detector. The clusters are produced in the source, which is adapted to the experiment at hand. There are a variety of sources available; the most commonly used are described in the following section with a summary of their most relevant characteristics. This section is intended as a reference for successive sections where measurements on clusters produced with specific sources are discussed.

A further section is devoted to mass-sensitive cluster detection, since cluster science requires specific mass-spectroscopic tools to accommodate the large mass ranges encountered in cluster beams. Furthermore, in quite a few experiments the mass-spectroscopic measuring device itself is used to probe a specific property. In those cases a basic knowledge of the detector is helpful.

General molecular-beam and vacuum techniques are not discussed and are treated in the references mentioned above.

A. Cluster sources

1. Overview

For reference the list below summarizes the characteristics of the most commonly used cluster sources and is followed by more detailed descriptions.

(a) Seeded supersonic nozzle sources are used mostly to produce intense cluster beams of low-boiling-point metals. These sources produce continuous beams with reasonably narrow speed distributions. Clusters with up to several hundreds (and, under suitable conditions, with thousands) of atoms per cluster may be produced in adequate abundance. The cluster temperatures are not well known; however, larger clusters are often assumed to be near the evaporation limit.

(b) Gas-aggregation sources are particularly efficient in the production of large clusters ($N < 10\,000$). The intensities are generally much lower than for nozzle sources. The overall cluster size distributions can be adjusted within rather broad limits. These sources are used for low-to-medium-boiling-point materials (< 2000 K). Low cluster temperatures (< 100 K) can be achieved.

(c) Laser vaporization sources produce clusters in the size range from the atom to typically several hundreds of atoms per cluster. These sources are pulsed and, although the time-averaged flux is low compared with the seeded supersonic nozzle source, intensities within a pulse are much higher. In principle, these sources can be used for all metals to produce neutral and positively and negatively charged ionized clusters. The cluster temperatures are expected to be near or below the source temperature, depending on the supersonic expansion conditions.

(d) Pulsed-arc cluster-ion sources are basically similar to laser vaporization sources. Here, however, an intense electrical discharge rather than a laser is used to produce the clusters, resulting in intense cluster-ion beams.

(e) Ion sputtering sources are used primarily to produce intense continuous beams of small singly ionized clusters of most metals. The clusters are hot, typically near the evaporation limit.

(f) Liquid-metal ion sources produce singly and multiply ionized clusters of low-melting-point metals. These clusters are hot, since in-flight evaporation and fission are observed.

2. Seeded supersonic nozzle source

In this source, metal is vaporized in a hot oven. The metal vapor is mixed with (or "seeded" in) an inert carrier gas (Larson *et al.*, 1974; de Heer, Knight, *et al.*, 1987; Hagena, 1991) by pressurizing the oven with the inert gas. Typically the inert-gas pressure is several atmospheres, whereas the metal-vapor pressure is in the range of 10–100 mbar. The vapor/gas mixture is ejected into a vacuum via a small hole, producing a supersonic molecular beam. The expansion into the vacuum proceeds adiabatically and causes cooling of the mixture (Anderson and Fenn, 1985). The cooled metal vapor becomes supersaturated, condensing in the form of clusters. Cluster production continues until the expanding vapor density becomes too low to promote further growth, typically within a few nozzle diameters from the nozzle exit. Likewise, the cooling of the clusters continues until the inert-gas density becomes so low that its flow is molecular rather than hydrodynamic.

The cooling provided by the expanding gas may be adequate to stabilize a cluster against evaporation, but if it is not, the clusters may further cool by evaporating one or more atoms. There is evidence that both processes take place. Spectroscopic measurements on alkali dimers and trimers have shown that very low temperatures can be achieved (Delacrétaz and Wöste, 1985); for example,

under high-pressure conditions, rotational temperatures of 7 K are found for the dimer. Although spectroscopic temperature determinations of large metal clusters are not yet available, there is experimental evidence that the final cooling step of larger clusters involves evaporation of one or more atoms, so that these clusters typically have temperatures close to the evaporation limit (Bjørnholm *et al.*, 1991). In either case the cluster abundances are determined by thermodynamic processes, so that the cluster abundances are sensitive to binding energies. This results in structured mass spectra, as further discussed in Sec. IV.

Experimentally it is found that the more massive the carrier-gas atoms, the better the cluster production (Kappes *et al.*, 1982). This is related to the larger collision cross sections, so that the transition to molecular flow occurs later than for a lighter gas.

Although the inert gas is very important, for historical purposes it is worth mentioning that neat expansions (without carrier gas) also produce clusters. In that case the cluster production is limited to small sizes, with usually fewer than ten atoms per cluster (although under suitable conditions larger clusters have been produced; Herrmann *et al.*, 1978; Delacrétaz *et al.*, 1982).

The seeded supersonic nozzle source is perhaps the most intense cluster beam source available. Material consumption is about 0.1 mole per hour, of which a sizable fraction (estimated in excess of 10% under suitable conditions) condenses into clusters in the beam. The cluster size distribution ranges from the atom to typically about 100-atom clusters, but, using optimal conditions, Pederson *et al.* (1991) produced alkali cluster beams with up to several thousand atoms per cluster.

A typical seeded nozzle source is shown in Fig. 7 (de Heer, Knight, *et al.*, 1987). This version is particularly well suited for metals with boiling points up to about 1300 K. The source consists of a reservoir and a tube terminating in a 100-micron-diameter pinhole nozzle.

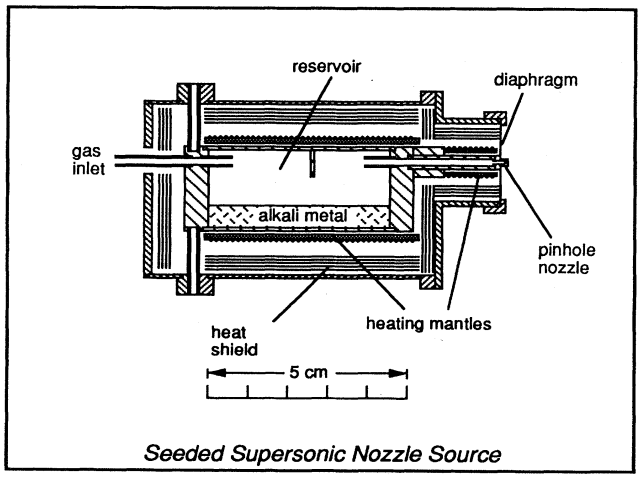

FIG. 7. Seeded supersonic nozzle source (de Heer, Knight, *et al.*, 1987).

These are heated with ceramic heating mantles would with tungsten wire. Heat shields and a water-cooled jacket (not shown) are required to prevent the vacuum chamber from overheating. Recently, using high-temperature alloys and indirect heating, source temperatures exceeding 1500 K have been attained. This source has been used for investigations of Li clusters (Blanc *et al.*, 1991; Dugourd, 1991).

3. Gas-aggregation cluster source

In the gas-aggregation source, metal is vaporized and introduced in a flow of cold inert gas (Fig. 8). This causes the vapor to become highly supersaturated. Due to the low temperature of the inert gas, cluster production proceeds primarily by successive single-atom addition. Since the reverse process (i.e., reevaporation) is negligible, the cluster abundances are not sensitive to the thermodynamic stabilities of the clusters and, consequently, the cluster abundances are relatively smooth functions of the cluster size determined mainly by collision statistics.

The cluster size distribution is determined by the parameters of the source, such as the metal-vapor density, gas flow rate, and dimensions of the various components. The final cluster temperatures are expected to be lower than those from the supersonic nozzle sources (especially for larger clusters) and depend on various source parameters.

Gas-aggregation sources have been used to produce continuous cluster beams of alkali metals and of more refractory metals (the noble metals, for example). The cluster abundances are, however, typically much lower than in supersonic nozzle sources, restricting the applicability of this source to some extent. Nevertheless, alkali clusters with over 20 000 atoms have been produced in sufficient abundances to facilitate a number of landmark experiments (Martin and Bergmann, 1989; see also Sec. IV.B).

Several versions of this source have been developed over the years, following the protoytype by Sattler, Mühlbach, and Recknagel (1980), such as those by Rayane *et al.* (1989), Schulze *et al.* (1988), and Limberger and Martin (1989).

4. Laser vaporization cluster source

The previously discussed sources are continuous and most useful for metals that can be vaporized in an oven. The laser vaporization source, on the other hand, is pulsed and is used to produce small clusters of any metal (Bondybey and English, 1982; Riley *et al.*, 1982; Smalley, 1983). In this source (see Fig. 9), metal vapor is produced by the pulsed-laser ablation of a rod of the material to be investigated. Light from a pulsed laser (i.e., Nd:YAG or excimer, where Nd:YAG is neodymium-doped yttrium-aluminum-garnet) is focused on the rod,

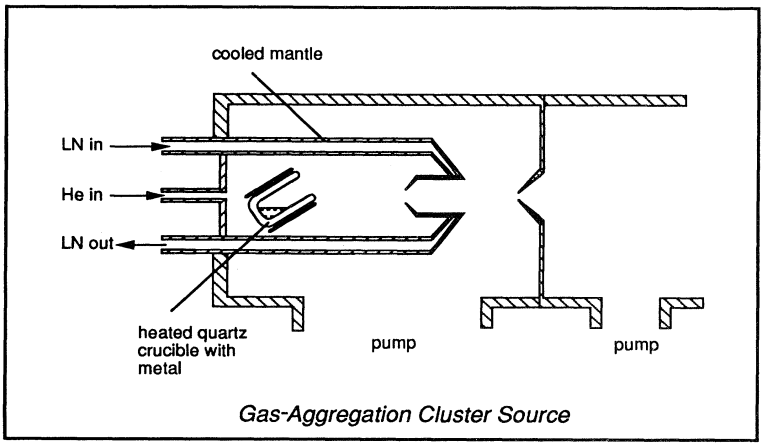

FIG. 8. Gas-aggregation source.

which is driven in a slow screw motion so that a fresh area of the surface of the rod continues to be exposed to the laser. The vaporized material is entrained in a pulse of cold helium gas from a pulsed valve. This cools the metal vapor, causing cluster formation as in the previously discussed sources. The inert-gas/cluster mixture is ejected out of the nozzle.

This source is, in certain respects, a hybrid of the gas-aggregation source and the high-temperature supersonic nozzle source, where cluster formation and initial cooling proceed as in the gas-aggregation source and the adiabatic supersonic expansion is as in the supersonic nozzle source. In fact, the adiabatic cooling is usually stronger than for the seeded supersonic nozzle source, since the cooling depends on the product of the nozzle diameter and the carrier-gas pressure (see, for example, Anderson and Fenn, 1985 and Anderson, 1974), and high instantaneous pressures in the source are achieved while much-larger-diameter nozzles can be used.

Direct evidence that the metal clusters produced in this source are indeed cold has recently been produced in an experiment on iron clusters in which the helium carrier was seeded with a trace of argon (Milani and de Heer, 1991). In these experiments a fraction of the neutral iron clusters were found to have an argon atom attached, which suggests temperatures below 100 K. The clusters can be cooled even further by reducing the temperature of the nozzle or of the entire source.

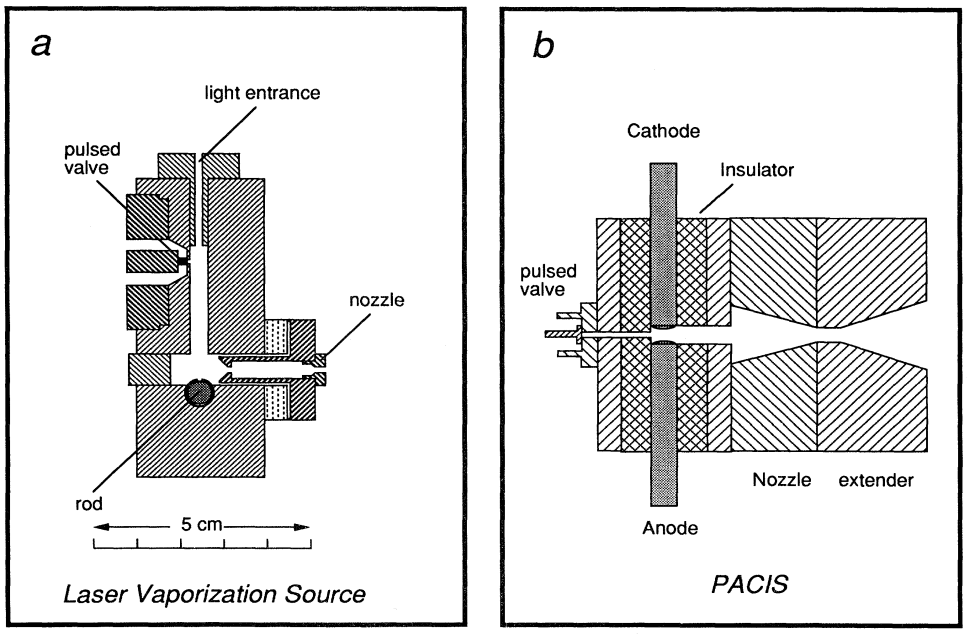

FIG. 9. Vaporization sources: (a) laser vaporization source (Milani and de Heer, 1991); (b) pulsed-arc cluster-ion source (after Siekmann *et al.*, 1991).

Cluster size distributions depend on the source conditions and typically range from atoms to several hundreds of atoms per cluster; under suitable conditions the cluster sizes may reach many thousands. The material consumption is very low (estimated at about 10^{15} atoms per laser shot, i.e., 10^{-3} mole per hour, but strongly dependent on the material used). However, since the beam is pulsed (with repetition rates on the order of 10 Hz), high instantaneous cluster intensities are achieved.

Several designs give good results. For example, the one in Fig. 9 uses a small cavity to optimize cluster growth and cooling of the metal-vapor/gas mixture (Milani and de Heer, 1990). With this source the thermally insulated nozzle may be further cooled to liquid-nitrogen temperatures. Recently Honea *et al.* (1991) succeeded in producing very cold sodium clusters ($N<200$) with a liquid-nitrogen-cooled source, demonstrating that the laser vaporization source is an attractive alternative even for alkali metals.

Closely related to the laser vaporization source is the PACIS [pulsed-arc cluster-ion source, Fig. 9(b)], where the rod is vaporized not by a laser but by an intense electrical discharge (Siekmann *et al.*, 1991). This source has several advantages compared with the laser vaporization source. The beams tend to be very intense; in fact, deposition rates of 2 Å per pulse (for lead clusters) have been reported (Siekmann *et al.*, 1991). About 10% of the emitted material is charged. Furthermore, this source is significantly less expensive, because it does not require a laser. Under suitable conditions the beams can be cold, as observed from the attachment of Ar atoms to the cluster ions (Ganteför *et al.*, 1990).

5. Sputtering source

Cluster-ion beams are produced by bombarding a metal surface with high-energy inert-gas ions (Fig. 10). In contrast to the previously discussed sources, the sputtering source does not rely on condensation in an inert gas. In fact, the cluster-production processes are still not fully understood.

Although the cluster-ion intensities are typically exponentially decreasing functions of the cluster size, still mass-selected beams with hundreds of atoms per cluster can be produced with sufficient intensities to perform mass spectroscopy (Katakuse *et al.*, 1985). For smaller sizes under optimal conditions for some materials the intensities are adequate (i.e., on the order of 10 nA) for mass-selected cluster deposition experiments (Harbich *et al.*, 1992).

For best cluster production, heavier inert gases (Kr or Xe) are typically used, while bombardment energies range from about 10 to 20 keV with currents up to 10 mA (Begemann, Dreihöfer *et al.*, 1986; Begemann, Meiwes-Broer, and Lutz, 1986; Fayet, Wolf, and Wöste, 1986). Hence these cluster sources require intense inert-gas ion sources as well as carefully designed ion optics to steer the intense cluster-ion beams.

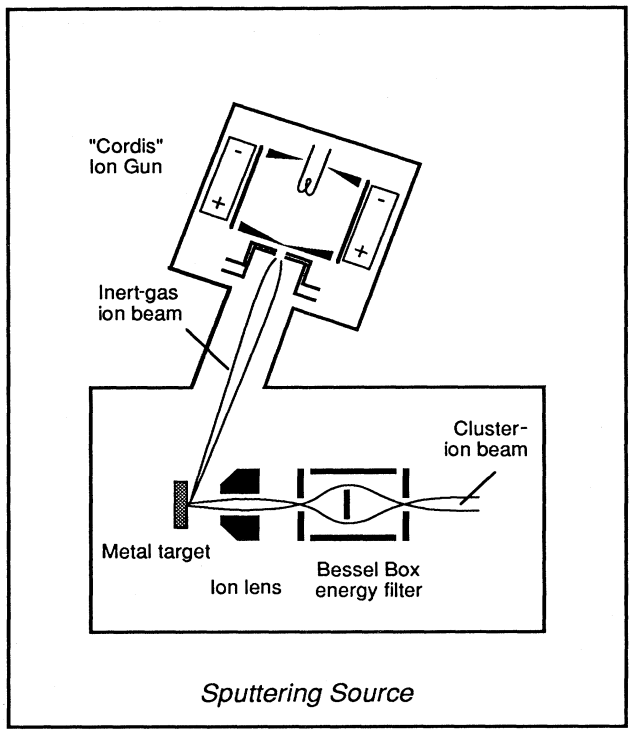

FIG. 10. Sputtering source. The focused ion beam from the Cordis ion gun sputters metal from the target. The cluster ions are focused and energy filtered to produce a monoenergetic cluster-ion beam. After Fayet, Wolf, and Wöste, 1986.

The initial cluster-ion temperatures are very high, and the clusters typically cool by in-flight evaporation (Begemann, Dreihöfer, *et al.*, 1986; Begemann, Meiwes-Broer, and Lutz, 1986). The kinetic-energy spread of the cluster ions is on the order of 10 eV or more. Since the cooling of the cluster ions involves evaporation, the abundance spectra reflect the thermodynamic stabilities related to the cluster binding energies (see Sec. IV.A.1). Accordingly, cluster abundance spectra from sputtering sources have provided evidence for electronic shell structure in several cluster species, notably the noble metals and the IIB metals, as discussed in Secs. IV.A.2 and IV.A.3. For a more detailed description of the properties of this source, see Begemann *et al.* (1989).

6. Liquid-metal ion source

These sources are primarily used to produce multiply charged clusters of low-melting-point metals (Fig. 11). A needle is wetted with the metal to be investigated, heated above the melting point of the metal, and a potential is applied (Sudraud *et al.*, 1979; Wagner *et al.*, 1979; Saunders *et al.*, 1989). Very high electric fields at the tip of the needle cause a spray of very small droplets to be emitted from the tip. The initially very hot and often multiply ionized droplets undergo evaporative cooling

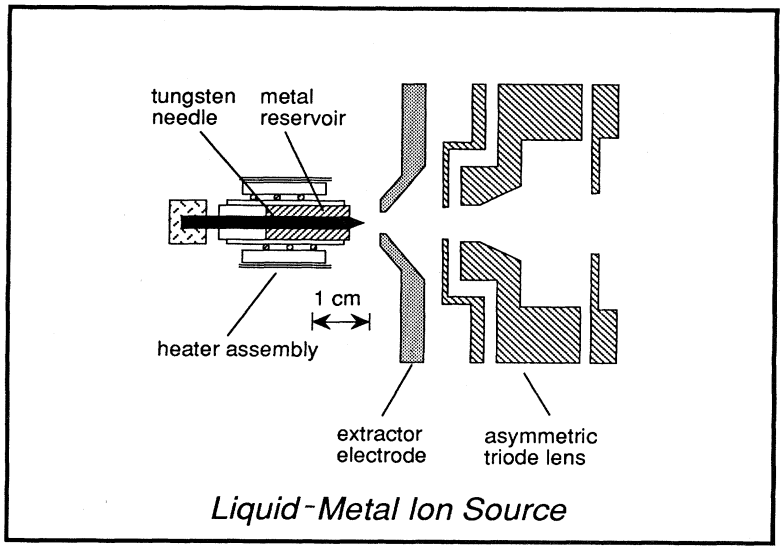

FIG. 11. Liquid-metal ion source. The heated tungsten needle is wetted with metal. A strong electric field extracts cluster ions from the tip. The cluster ions are focused with electrostatic ion lenses. After Saunders and Fredrigo, 1989.

and fission to smaller sizes. Mass-selected cluster-ion currents on the order of 10^4 s^{-1} (after energy filtering and mass analyses) have been reported by Saunders and Fredrigo (1989).

Liquid-metal ion sources are often used in experiments involving multiply charged small clusters. Cluster mass spectra have been analyzed to elucidate shell structure in rubidium and cesium clusters (Bhaskar *et al.*, 1987) and in sodium clusters (Saito *et al.*, 1989).

B. Mass analyzers

1. Wien filter

In the Wien filter (Fig. 12), mass separation is accomplished with crossed homogeneous electric (E) and magnetic (B) fields, perpendicular to the ionized cluster beam. The net force on a charged cluster with mass M, charge Q, and velocity v vanishes if $E=Bv/c$. The cluster ions are accelerated by a voltage V to an energy QV. Passing through the filter, clusters with $M/Q=2V/(Ec/B)^2$ are undeflected. The undeflected cluster ions are selected with appropriately positioned collimators.

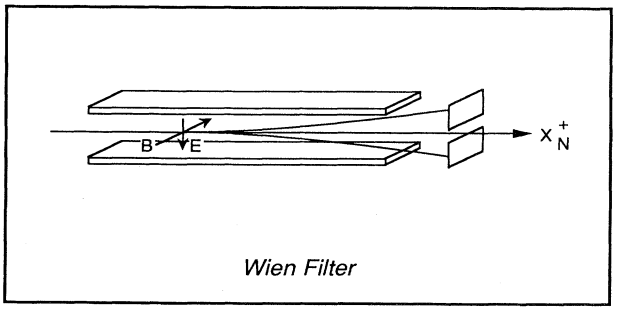

FIG. 12. Wien velocity filter.

The resolution of a Wien filter depends on the velocity spread of cluster ions (which depends on their initial velocity distribution), the strength of the fields, and the collimator widths. To obtain high resolution, narrow collimators and strong fields are required as well as large acceleration potentials to reduce initial velocity effects. In practice, for clusters (with a commercial Wien filter) the resolution $\delta M/M$ is typically on the order of 10^{-2}. The practical mass range is typically 1–5000 amu, limited primarily by the field strengths.

2. Quadrupole mass filter

The quadrupole mass filter (Fig. 13) operates on the principle that ion trajectories in a two-dimensional quadrupole field are stable if the field has an ac component superimposed on a dc component with appropriate amplitudes and frequencies (Paul *et al.*, 1958; Scoles, 1988, p. 181).

From the equations of motion for an ion in these fields (similar to those of an inverted pendulum), it can be shown that, with correctly adjusted fields, the trajectories of singly charged ions are stable only within a very narrow mass range. Although the stability condition does not depend on the ion velocity, high velocities do affect the resolution (see below).

The quadrupole pole pieces are usually precisely machined cylindrical rods, which are held very accurately parallel in a square configuration with ceramic insulators. Pairs of opposing rods are electrically connected. A time-dependent potential $U+V\cos(\omega t)$ is applied to one pair of rods and $-[U+V\cos(\omega t)]$ to the other (Fig. 13). The condition for critical stability is obtained for $U/V=0.168$ (Scoles, 1988).

The resolution is determined by how close to the point of critical stability the quadrupole is operated. In partic-

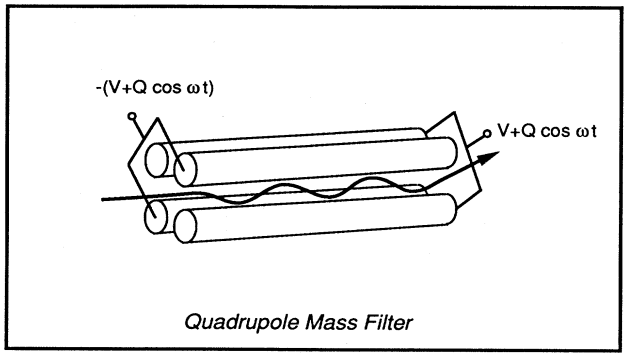

FIG. 13. Quadrupole mass filter. Only cluster ions with a charge-to-mass ratio corresponding to the applied ac and dc voltages will pass through the filter, as shown schematically.

ular, reducing V decreases the resolution, and for $V=0$ all ions are stable. (In fact, by setting $V=0$, one may use the mass filter as an ion guide.) Other factors affecting the resolution and throughput are (1) the velocity of the ions (i.e., the number of rf cycles that the ions spend in the filter), (2) the accuracy with which the ions are introduced into the filter (i.e., on axis with small incident angles and at low velocities), and (3) the alignment of the rods. A resolution of 10^{-3} is typical.

The mass range of commercial devices is usually limited to 1000 amu. Increasing the voltages and reducing the frequency increases the mass range. Mass ranges of devices thus modified may be 8000 amu or more (de Heer, Knight, *et al.*, 1987). However, with reduced frequencies a substantial degradation of resolution may occur. Furthermore, the higher voltages promote electrical discharges.

3. Time-of-flight mass spectrometry

A time-of-flight mass spectrometer consists of an ion gun, a field-free drift space, and an ion detector (Fig. 14). The neutral clusters are first ionized, typically using a pulsed ultraviolet laser or electron beam. A succession of homogeneous electric fields (the ion gun) accelerates the ions that pass through the field-free drift space (the flight tube) and ultimately impinge on an ion detector. The detection electronics, for example, a digital oscilloscope, records the arrival time of the ions. The mass of the cluster (or actually its mass-to-charge ratio) is determined from the measured flight time.

The Wiley-McLaren (1955) time-of-flight mass spectrometer is a typical and widely used configuration consisting of a double field ion gun. This ion-gun arrangement, designed for residual gas analysis, compensates somewhat for the initial velocities and the initial positions of the ions. A more efficient design (de Heer and

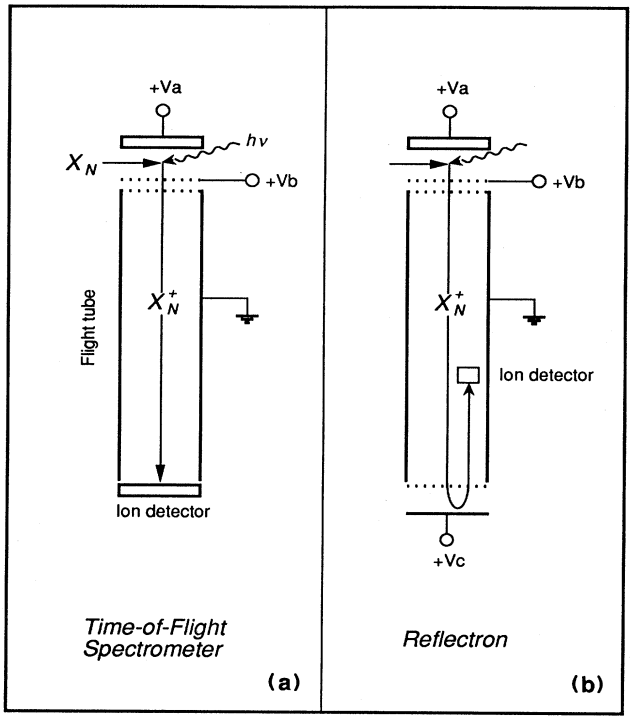

FIG. 14. Time-of-flight mass spectrometer (a) in the standard linear configuration and (b) in the reflectron configuration.

Milani, 1991) uses a triple field ion gun (the second of which is actually field free), improving the initial position compensation by more than an order of magnitude. Other features include position- and velocity-sensitive detection as well as dynamic ion-deflection plates for improved resolution, and a large-area ion detector. For this, as for all time-of-flight mass spectrometers, the resolution is limited primarily by the initial conditions, timing accuracy, and stability of the power supplies.

The resolution of a time-of-flight mass spectrometer is improved significantly using the reflectron scheme [Fig. 14(b)], in which the dispersion due either to initial velocities or to initial positions is compensated to a high degree (Bergmann *et al.*, 1989). In the reflectron the ions are not detected at the end of the flight tube, but reflected back by means of an electrostatic mirror. The reflected ions are detected with an ion detector as before.

The mirror is a uniform electric field at the end of the flight tube, opposing the velocity of the ions and functions as follows. The time necessary for an ion to reverse its direction in the mirror depends on its velocity: the faster ions need more time than the slower ones, so that the slower ions of the same mass have time to catch up. In a reflectron all ions with a specific mass arrive at the detector simultaneously.

This method for compensating the initial velocity variations is very effective, and resolutions of 10^{-5} have been achieved, i.e., at least an order of magnitude better than linear time-of-flight mass spectrometers.

4. Ion cyclotron resonance mass spectroscopy

Ion cyclotron resonance spectroscopy is performed in a three-dimensional ion trap. Ions are confined by a combination of a static quadrupole electric field and a highly uniform magnetic field B. Because of the magnetic field, one component of the motion of the ions is at the cyclotron frequency $\omega_c = QB/Mc$, so that from a measurement of this frequency the mass-to-charge ratio (M/Q) of the ions may be determined.

The cyclotron resonance frequencies are measured by exciting the ion cloud in the trap with an electrical pulse. A sensitive antenna (consisting of a parallel-plate capacitor) then picks up the electric signal from the vibrating ion cloud. This signal is accumulated for as long as possible and is then Fourier analyzed. From an analysis of the frequency components and their amplitudes, the masses and relative abundances of the ions in the cloud are determined.

This kind of mass spectroscopy is extremely accurate, and masses may be measured with a precision of 10^{-6} or greater. It also has the advantage that the measurement is not destructive, so that the constituent cluster ions in the ion cloud may be measured repeatedly over relatively long periods of time. Furthermore, using various sequences of radio-frequency pulses, the ion cloud may be manipulated so that specific ions are ejected from the trap while others are not affected. Moreover, by introducing low-pressure buffer gases into the vacuum chambers, one may achieve a certain degree of temperature control. For reviews of these techniques, see Comisarow and Nibbering (1986), Wanczek (1984), and Mandich (1989). Despite these extraordinary features, this technique has been applied to a limited degree in the study of simple metal clusters.

5. Molecular-beam "chromatography"

Chromatography relies on the separation of molecular species due to their different mobilities in a gas. This method has long been used to separate neutral molecules. Recently, cluster species separations based on cluster mobilities have been achieved for metal and semiconductor clusters by von Halden *et al.* (1991) and Jarrold *et al.* (1991, 1992). In this method, cluster ions produced in a laser vaporization cluster source are mass selected and introduced in a long inert-gas-filled drift tube with 50-micron entrance and exit apertures. The temperature and the pressure of the gas can be accurately controlled. The clusters drift through this tube under the influence of a weak electric field.

Since the cluster mobilities depend on collision rates with the inert gas, they are sensitive to the cluster shape. In this way clusters of a given size but with differing shapes (i.e., shape isomers) are temporally separated in the drift tube. Initial investigations of silicon and aluminum clusters are very promising and show that this undoubtedly will become a very important tool for determining cluster shapes and for identifying isomers.

IV. METAL CLUSTER ABUNDANCE SPECTROSCOPY

In experiments with supersonic seeded cluster sources, cluster formation from the saturated vapor is likely to depend on a balance between growth and evaporation. After the clusters leave the nozzle, they will be stable if the adiabatically expanding carrier gas provides enough cooling so that evaporation does not occur on the time scale of the experiment (de Heer, Knight, *et al.*, 1987). On the other hand, the clusters may be cooled further by evaporating atoms while in the beam (Klots, 1985; Begemann, Dreihöfer, *et al.*, 1986; Begemann, Meiwes-Broer, and Lutz, 1986; Bjørnholm *et al.*, 1991). In either case, the cluster intensity is a very sensitive function of the cluster binding energy. As shown below, these two processes give relative cluster intensities that are enhanced for clusters with relatively larger stabilities. The sodium cluster mass spectrum shown in Fig. 1 reveals this property.

The intensities I_N is a mass spectrum depend on several factors and can be expressed as

$$I_N = (\text{Production})_N (\text{Source-to-ionization transfer efficiency})_N (\text{Ionization efficiency})_N \ (\text{Detection efficiency})_N \ .$$

Each of these factors can contribute, depending on experimental details. Both the production process and evaporation occurring during transfer may be responsible for fine structure in the neutral cluster size distribution.

The mass spectrum in Fig. 1 was obtained with broadband UV light. Under those conditions, structure caused by the ionization efficiency factor is effectively suppressed. Alternatively, with monochromatic light near the photoionization threshold, the ionization efficiency factor may dominate the structure of the mass spectra, since clusters with higher ionization potentials are less efficiently ionized than those with lower ionization potentials. Examples are given below. The detection efficiency, on the other hand, is always expected to vary smoothly with size.

Mass spectra have been recorded for clusters of many metals, using various methods of production and detection. Here we present some examples that are mutually compared and further discussed in terms of simple models. The abundance spectra are presented as $\log_{10}(I_N)$,

i.e., the base-10 logarithm of the intensities of the mass peaks, so that they are more easily compared with each other and with theory.

A. Abundance spectra

1. Group IA: alkali-metal clusters

The sodium abundance spectrum, Fig. 1, was previously discussed and compared with the ellipsoidal shell model in Sec. II.B. Here it is shown on a logarithmic scale together with the potassium abundance spectrum (Fig. 15; Knight *et al.*, 1984, 1985b). The clusters produced in a seeded supersonic nozzle source were ionized with broadband UV and analyzed with a quadrupole mass analyzer (de Heer *et al.*, 1985; de Heer, Knight, *et al.*, 1987).

There are clear similarities in the abundances of corresponding clusters. Both cases show the spherical shell-closing steps. The fine-structure features are systematically smaller in potassium than for sodium. This effect is consistent with the larger Fermi energy of Na compared with K, which, as discussed in Sec. II, determines the energy scale of the electronic structure and consequently the articulation of the fine structure in the abundance spectra (Sec. II.B.2).

The structure in the abundance spectra of alkali cluster beams produced in seeded supersonic nozzle sources reflects the cluster binding energies. Even small variations in binding energy importantly influence cluster production. There are now two possible ways this may happen. In one case, the abundances are determined by an evaporative process; in the other, by thermal equilibrium, i.e., a balance between growth and evaporation.

Assuming that the final cooling step involves evaporation of atoms, Bjørnholm *et al.* (1991; see also Klots, 1988) have suggested that the cluster abundances I_N are determined by

$$\ln(I_{N+1}/I_N)=\Delta_2 F(N)/kT\ , \tag{4.1}$$

where

$$\Delta_2 F(N)=(F_{N+1}+F_{N-1}-2F_N) \tag{4.2}$$

is the second difference of the Helmholtz free energies $F_N=E_N-TS$, and E_N is the total energy of the cluster. This expression takes into account the electronic contributions to the free energy, which are important for larger clusters (or high temperatures) when the shell step sizes are comparable to kT.

Alternatively, de Heer, Knight, *et al.* (1987) suggested

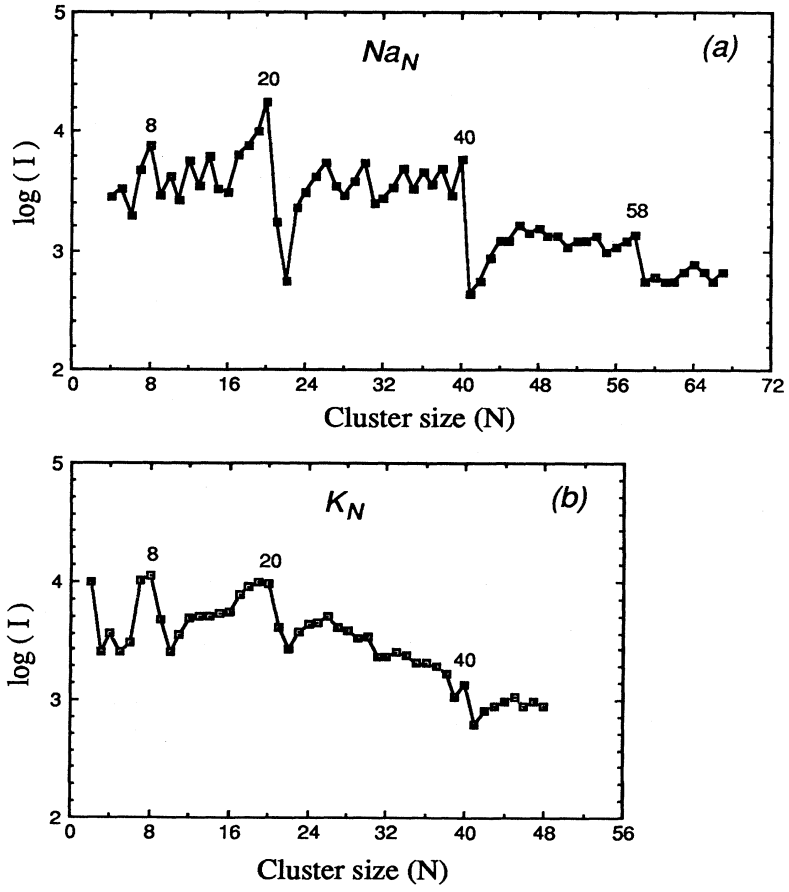

FIG. 15. Alkali abundance spectra: (a) sodium abundance spectrum (from Fig. 1) presented with a logarithmic scale, (b) potassium abundance spectrum (after Knight *et al.*, 1984). Spherical-shell-closing numbers are indicated.

that the cluster abundances may reflect a quasiequilibrium distribution in the nozzle, which is subsequently rapidly frozen in the adiabatic expansion. The relative abundances in the mass spectra (using the law of mass action) are then given by

$$\ln(I_N^2/I_{N+1}I_{N-1})=\Delta_2 BE(N)/kT\ , \tag{4.3}$$

where $BE(N)$ is the total binding energy of the cluster. (Here the electronic contribution to the free energy is ignored.)

Note that these expressions are derived from general thermodynamic considerations. The equations are constructed to emphasize cluster-to-cluster intensity variations in which contributions due to the vibrations of the ionic cores cancel in lowest order.

Comparing the experimentally determined values corresponding to the left-hand sides of Eqs. (4.1) and (4.2) with the second difference of the total energies in the ellipsoidal shell model is instructive (see Fig. 16). It is clear that both the thermal equilibrium model and the evaporative model compare well with the shell-model predictions, and from these data it is difficult to decide which of the two processes, in fact, determines the cluster abundances. Curiously, both models predict very similar structure in the mass spectra [Figs. 16(a), 16(b)]. Further experiments, in particular, those which can detect in-flight evaporation (as, for example, Begemann, Dreihöfer, *et al.*, 1986; Begemann, Meiwes-Broer, and Lutz, 1986), will be necessary to distinguish between the processes in this size regime.

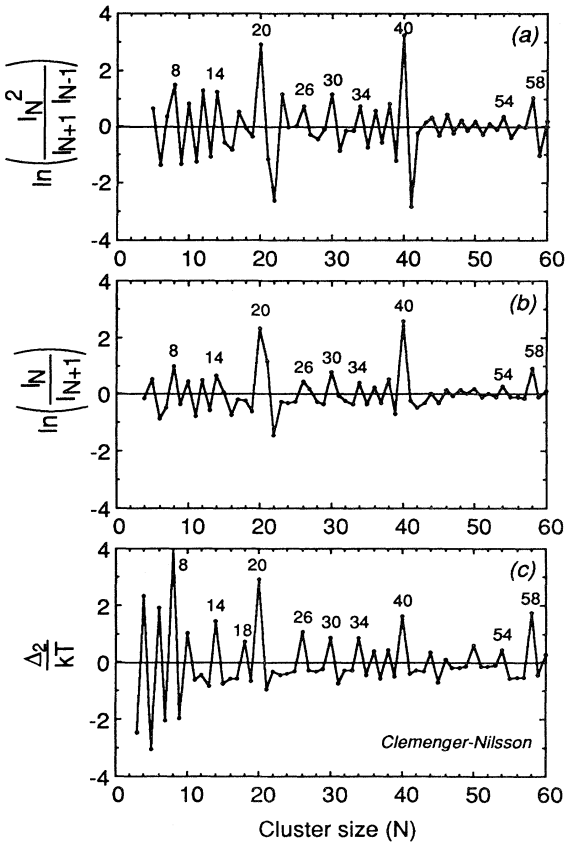

FIG. 16. Comparison between abundance spectra and the ellipsoidal shell (Clemenger-Nilsson) model: (a) the logarithmic ratio from the quasiequilibrium model, Eq. (4.3) (de Heer, Knight, *et al.*, 1987), and (b) the evaporative model, Eq. (4.2) (Bjørnholm *et al.*, 1991). These are compared with the second differences of the binding energies scaled with the temperature, as, for example, in (c) from the Clemenger-Nilsson model.

In either case it can be seen in Fig. 16(c) that the ellipsoidal shell model reproduces the fine structure in the mass spectra quite reasonably. We should point out that this agreement requires a temperature of about 800 K. This is far too hot for clusters to be stable in the beam, but it is consistent with the nozzle temperature and hence with the frozen equilibrium process. This conclusion, however, is speculative.

Spectra of cesium clusters from a gas-aggregation source have been recorded and electronic shell structure observed (Bergmann *et al.*, 1988; Limberger and Martin, 1989). These clusters were not pure, but contained a few oxygen atoms. In this case the shell structure appears in the mass spectra by ionizing the clusters with light close to the ionization potential (Sec. VI). Hence this method is sensitive to small cluster-size-dependent variations in the ionization potentials. Enhanced ionization potentials for $Cs_{2n+N}O_n$, with $N=8$, 18, 34, 58, and 92, and small n are consistent with the shell model (see also Sec. VI.D.1). Shell structure is observed up to at least $N=600$ (Göhlich *et al.*, 1990).

Rubidium clusters produced in a liquid-metal ion source also show steps at the electronic shell closings (Bhaskar *et al.*, 1987). In this source (as in the supersonic nozzle source) the final cooling is caused by evaporation, so that the abundance spectra reflect relative cluster stabilities.

2. Group IB: noble-metal clusters

The cluster-ion abundance spectra of copper, silver, and gold show very pronounced shell structures and are also strikingly similar to each other (Fig. 17). These cluster ions were formed with a sputtering source using a 20-kV krypton ion beam (Katakuse *et al.*, 1985, 1986). Sputtered cluster ions are initially very hot and cool by evaporation, producing the fine structure in the abundance spectra. Since the clusters are created as ions, the abundance spectra reflect the stability of the cluster ions.

An important feature is that the shell steps now occur at 9, 21, 35, . . . , i.e., rather than 8, 20, 34, . . . from the shell model. Since the cations have one less electron conduction than atoms, these electronic shell closings agree with the shell model. Note also that the shell step that should be at 59 is smeared out over several clusters. This reflects the effect of finite temperatures on the (conduction) electron system. As the cluster size increases, the otherwise sharp steps in occupation at the Fermi level be-

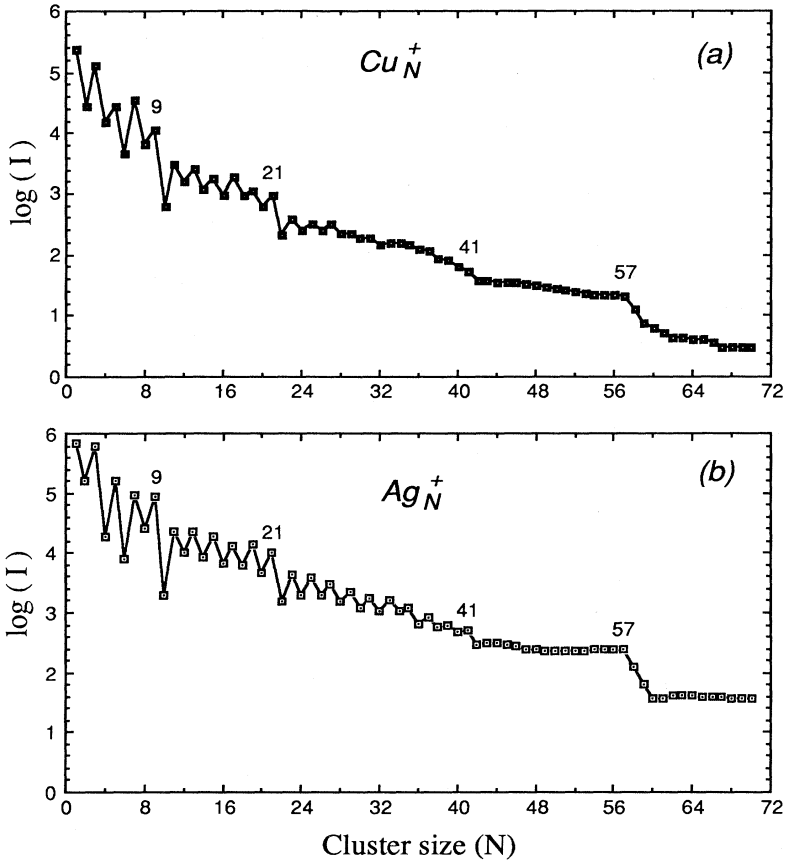

FIG. 17. Logarithmic abundance spectra of (a) copper and (b) silver cluster ions produced in a sputtering source. Numbers correspond to spherical shell closings after Katakuse *et al.*, 1985.

gin to become smeared out (Brack, Genzken, and Hansen, 1991a). The (rounded) shell steps are also observed at 93, 139, and 199 (not shown) and also agree with the shell model.

Comparing these spectra with those of Na and K shows several differences. In Cu and Ag, the fine structure is dominated by odd-even alternations in the intensities, while the sodium spectrum reflects subshell structure predicted by the shall model (Sec. II.B). In any case the noble-metal clusters are excellent examples of spherical shell structure.

3. Group IIB: zinc and cadmium

Cluster mass spectra of these two divalent metals have been obtained with a sputtering source (Katakuse *et al.*, 1986), and the discussion concerning the production conditions also applies here (Fig. 18). The two spectra are very similar: almost all of the structure in one is also found in the other, and there is no obvious difference in the intensities of the various features.

Again the peaks can be compared with shell-model predictions. According to the shell model, for these cluster ions the intensity maxima ought to occur at N=4,9,10,17,20,29,34,35,46,53,56,69,. . . (note that each atom contributes two electrons). In fact, they are observed at 10,18,20,28,30,32,35,42,46,54,70. Although there are many correspondences between the two sets of numbers, perhaps even enough to claim that electronic shell structure alone determines the stabilities, there are at the same time several differences that indicate that other effects could also play a role, so that this interpretation is by no means conclusive. For example, in order for group-IIB materials to become metals, the filled *s* band must first hybridize with the unoccupied *p* band. If this hybridization proceeds slowly with size, then the effects will be apparent in binding energies. In fact, for mercury, this hybridization proceeds so slowly that small mercury clusters are found to be only weakly bonded, essentially by van der Waals forces (Rademann *et al.*, 1987). Although this may be less extreme in the case of Cd and Zn, perhaps some residual effects of this nature could occur (see below and also the discussions of aluminum and magnesium clusters below).

4. Group IB: calcium, magnesium, and barium

Of the group-IIA metals, mass spectra of calcium, magnesium, and barium have been recorded. The barium clusters were produced in a gas-aggregation source and ionized with electron bombardment (Rayane *et al.*, 1989; Fig. 19). The conspicuous mass peaks correspond closely

to the magic numbers found for argon clusters (i.e., 13,19,26,29,32,...). These are not the numbers that result from electronic shell models. In fact, they correspond more closely to magic numbers associated with beams of inert-gas clusters where the stability is due to geometrical packing effects. (For a description of inert-gas clusters, see Echt *et al.*, 1981.) From this observation it was deduced that small barium clusters are close packed, indicating that geometrical effects rather than electronic effects dominate the cluster stabilities (Rayane *et al.*, 1989). In this context it is interesting to note that there is no obvious correspondence between this spectrum and those of Cd and Zn above.

Barium clusters with a few oxygen atoms, $Ba_N O_X$, have been investigated by Martin and Bergmann (1989). They find enhanced stabilities for $N=13$, 19, 23, 26, 29, 32, and 35, independent of the oxygen content ($X=1,2,3,4$).

More recently, mass spectra of magnesium (Martin, Bergmann, *et al.*, 1991a, 1991b) and calcium clusters (Martin, Naher, *et al.*, 1991; Martin, Bergmann, *et al.*, 1991b) extending to very large sizes have been obtained. The clusters were produced in a gas-aggregation source and ionized with intense pulsed-laser light, thereby ionizing the clusters in a multiphoton process. The illumination causes not only ionization but also evaporation due to heating, so that the more intense peaks in the mass spectra reflect the enhanced stabilities (in this case of the cluster ions). Stability peaks are found for 147, 309, 561, 927, 1425, 2057, and 2869, corresponding closely with completed Mackay icosahedra [see Eq. (4.4) below], suggesting that, for the stabilities, geometrical effects dominate the binding energy. Similar results are found for large calcium clusters (with up to 10 000 atoms per cluster; Martin, Naher, *et al.*, 1991).

It is tempting to interpret the observations as evidence

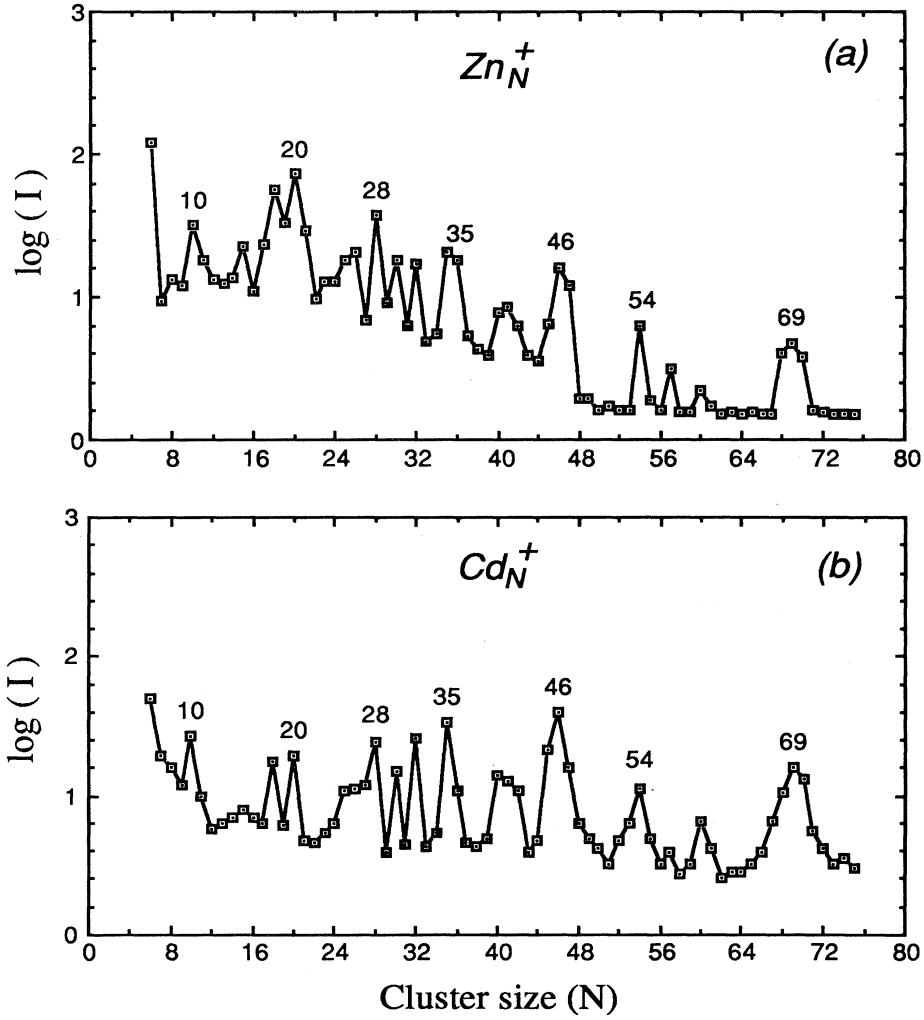

FIG. 18. Logarithmic abundance spectra of (a) zinc and (b) cadmium cluster ions from a sputtering source. Spherical-shell-closing numbers of these divalent metals are indicated after Katakuse *et al.*, 1986.

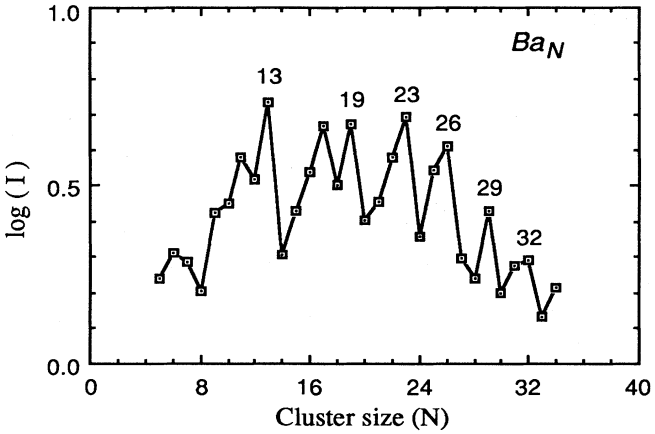

FIG. 19. Logarithmic abundance spectrum of barium clusters produced in a gas-aggregation source (after Rayane *et al.*, 1989). The conspicuous peaks closely correspond to magic numbers found in inert-gas cluster spectra.

that these clusters are nonmetallic. This would be consistent with the fact mentioned above that, in order for a group-II element to be metallic, the filled atomic *s* levels must hybridize with unoccupied *p* levels to produce the *sp* conduction band of the bulk. In fact, theoretical studies (Reuse *et al.*, 1990) bear out that for Mg clusters the hybridization proceeds rather slowly (as determined from a Muliken population analysis); however, electronic shell effects in the binding energies and ionization potentials are apparent. On the other hand, Kawai and Weare (1990) obtained related results for Be clusters and found that the hybridization was essentially complete for $N=6$.

Since there are no detailed theoretical studies on Ba clusters, it is reasonable to assume that geometrical effects dominate the binding energies and that electronic shell effects are of secondary importance, in order to explain the mass spectra. However, it is clear that further study is necessary.

5. Group III: aluminum and indium

Clusters of these trivalent metals have been produced in a laser vaporization cluster source and ionized with a laser (Schriver *et al.*, 1990). Two kinds of experiments have been performed. In one, the clusters are ionized near the ionization threshold, so that clusters with relatively lower ionization potentials (i.e., clusters immediately following an electronic shell closing; see Sec. VI) are ionized with greater probabilities. In the second experiment, the ionization energy is well beyond threshold, so that the spectra more closely follow the abundances in the neutral beam. Thus closed-shell clusters should be more frequently detected.

Both experiments give consistent results showing electronic shell closings for clusters with sizes varying from 138 to 1218 electrons (i.e., 46–306 atoms), as predicted by the shell model. (However, as will be discussed below, other experiments show that for smaller aluminum clusters the electronic shell model does not apply as well.)

B. Supershells

A theory originally developed for nuclei by Balian and Bloch (1972) and applied to clusters by Nishioka, Hansen, and Mottelson (1990) predicts supershell structure, which can be described as a beating phenomenon in the shell structure. The beating effect can be visualized as an interference of two types of semiclassical electron orbits (i.e., triangular and square) inside a spherical potential well. Constructive interference causes large-amplitude oscillations in the binding energies, while destructive interference gives small-amplitude oscillations. This effect should cause corresponding amplitude oscillations in the cluster abundance spectra. Calculations show that the period of the stability oscillations (plotted as a function of $N^{1/3}$) is quite regular (Nishioka *et al.*, 1990). The amplitudes, however, exhibit the supershell beating effect. For example, at about 1000 the shell effects have become very weak, but they reappear and are again very strong at $N=2500$, and so forth.

Conclusive experimental evidence for the supershell beating effect has resulted from very careful analyses of the abundance spectra, in which not only are the intensities measured but attention is also paid to the shell-closing numbers themselves. The beating effect should be seen not only in the abundances, but also in a phase shift in these numbers, best visualized when the shell index numbers are plotted as a function of the cluster radius. This phase shift is experimentally observed, confirming the supershell prediction (Pedersen *et al.*, 1991). Recently the supershell beating effect has also been observed for large lithium clusters (Bréchignac, Cahuzac, de Frutos, Roux, and Bowen, 1992) and aluminum clusters (Lermé *et al.*, 1992). The supershell beating effect and the experimental evidence for it are reviewed in Sec. V.A of Brack (1993).

C. Evolution to bulk crystal structure

The electronic shell structure that dominates the cluster properties for small sizes is expected to become of lesser importance for larger-sized clusters, since the shell steps diminish as the size increases. On the other hand, the electronic structure of bulk materials exhibits finite crystal-field effects, so that it is clear that a transition from an electronic structure dominated by shell effects to one dominated by crystal-field effects should occur at a finite size.

It is obviously important to follow the shell structure for large clusters to determine its practical limit. Figure 20 shows sodium mass spectra up to Na_{600} (Bjørnholm *et al.*, 1991), obtained with experimental methods similar to those used for the sodium spectra above. The logarithmic derivative of the intensities is also shown, because it

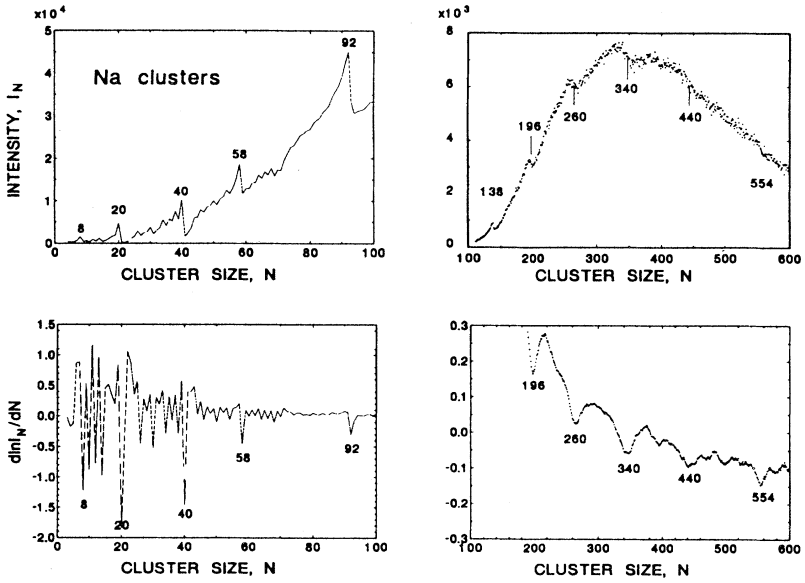

FIG. 20. Sodium cluster abundances. Top panels: abundance spectra for sodium clusters produced in a supersonic nozzle source. Bottom panels: logarithmic differences of spectra in top panels. Bottom left, Eq. (6.1); bottom right, smoothed according to a procedure described by Bjørnholm *et al.* (1991). After Bjørnholm *et al.*, 1991.

brings out the shell structure more clearly. Spherical shell closings are observed throughout this range.

Going much further than this, sodium mass spectra have been recorded up to $N=25\,000$ by Martin *et al.* (1990a, 1990b; Martin, Bergmann, and Mallnowski, 1990; Martin *et al.*, 1991b) using a gas-aggregation source and laser ionization. Portions of the spectrum, for which two different laser-light wavelengths were used, are shown in Fig. 21. In this case the structure is brought out by using light very close to the ionization threshold, so that the shell structure manifests itself as minima in the mass spectra, since closed-shell clusters have relatively larger ionization potentials. Two series of numbers are identified: 340, 440, 560, 700, 840, 1040, 1220, and 1430, which are spaced as the spherical shell-closing numbers, and a second series for larger clusters, 1980, 2820, 5070, and 6550, which is continued with 8170, 10 200, 12 500, 15 100, 18 000, and 21 300, from other spectra, closely following the algorithm

$$N=\tfrac{1}{3}(10K^3-15K^2+11K-3)\ . \tag{4.4}$$

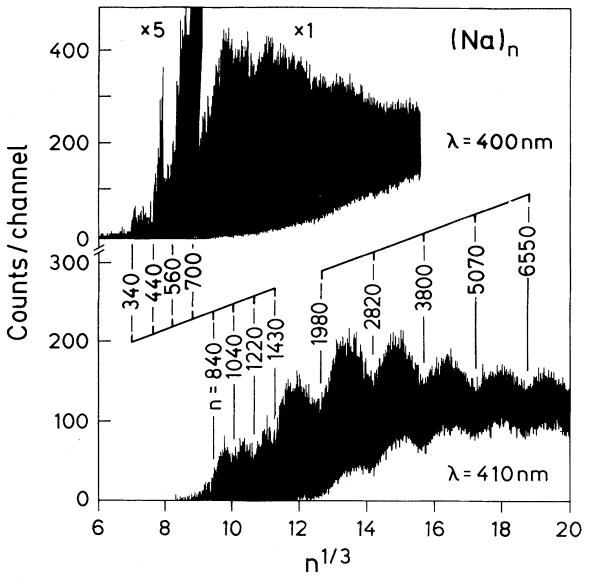

FIG. 21. Mass spectrum of sodium clusters photoionized with 400- and 410-nm light. Two sequences of structures are observed at equally spaced intervals on the $N^{1/3}$ scale after Martin *et al.*, 1990a, 1990b; Martin, Bergmann, and Mallnowski, 1990.

These are not electronic shell-closing numbers, but rather the numbers corresponding to Mackay icosahedra (which are geometrically compact structures analyzed by Mackay, 1962) with K shells of atoms. These results for sodium indicate that at low temperatures the fine structure from electronic shell structure becomes less important compared to geometrical shell structure for sizes near $N=2000$.

It is not yet completely clear why geometrical closed-shell clusters should have higher ionization potentials. In fact, the structures observed may be due to evaporation following the ionization, with the effect of enhancing the signals of the more stable cluster ions. In any case, the correspondence between the experimental and theoretical numbers is so impressive that there can be little doubt about the interpretation.

There has been considerable speculation concerning the transition from electronic shell structure to geometrical shell structure. Martin, Bergmann *et al.* (1991b) suggested that the atoms in small clusters are mobile, so that they will form small spherical droplets (as if they were liquid), while this is not the case for larger clusters, which when cold will grow as small crystallites. When this occurs, the electronic shell effects are no longer observed and instead are replaced by patterns related to the growth of crystallites.

On the other hand, Björnholm *et al.* (1991) have shown that the amplitude of the observed shell steps depends on the temperature and cluster size. At elevated temperatures the shell steps are washed out. This was also borne out in calculations by Brack *et al.* (1991; see also Brack, 1993, Sec. V.A.2).

However, Clemenger (1991) has shown that the crystal structure is reflected in the electronic structure only when the perturbations (on the electronic structure) caused by the crystal shape are larger than the electronic shell steps. He finds that this transition from electronic shell structure to crystalline structure should occur at $N=1640$, in good agreement with experiment.

These three explanations are not equivalent, so that, in principle, the question can be resolved with further experiments—for example, by carefully investigating the temperature dependence of the transition from electronic to geometric shell structure.

D. Conclusion

Mass spectra may provide valuable information on the size-dependent fine structure of binding energies in metal clusters. At first this is surprising, since the absolute values of these quantities vary by relatively very small amounts. Nevertheless, the mass spectra involve Boltzmann factors of these energies, so that at low temperatures small differences are amplified in the abundances.

Perhaps even more striking are the consistent correlations between the binding energies of small clusters and the mean-field electron energies. *A priori* it can hardly be expected that the binding energy of Na_9, for example, is related to that of Na_8, considering that these are entirely different systems from a molecular point of view. The fact that these correlations exist shows the relatively minor importance of the ionic cores other than to provide a neutralizing background for the electrons. This principle is, of course, the basis for the shell model and the jellium model.

The recently discovered supershell effects are magnificent achievements. These experiments indicate how well the mean-field approach works for simple metal clusters, since the crystal-field effects are not sufficient to perturb the subtle coherence in the electronic structure even over very large ranges of clusters sizes. Also very important is the observed transition from electronic shell structure to geometrical shell structure. Although this is an important step towards the bulk phase, the Mackay structures do not have the bcc crystal structure of bulk sodium, so that a second transition may be expected for even larger sizes.

V. STATIC DIPOLE POLARIZABILITIES

Of all the experimental probes available for clusters, few are as straightforward as polarizability measurements (for general reviews, see Hall and Zorn, 1974; Miller and Bederson, 1977). A collimated cluster beam passes through the inhomogeneous electric field produced by two curved pole faces. (Typical field strengths E are on the order of 10^5 V/cm, and field gradients dE/dz are on the order of 10^5 V/cm^2.) The electric field induces an electric dipole moment, and the field gradient acts on the dipole, causing the clusters to experience a force perpendicular to their direction of flight. Hence the clusters are deflected. From the deflections d and velocities v, the forces and hence the polarizabilities α are determined:

$$d = K\frac{\alpha E}{Mv^2}\frac{dE}{dz} , \tag{5.1}$$

where M is the mass and K a constant depending on the geometry of the apparatus. The deflections are typically quite small (a fraction of a mm). The cluster beam is tightly collimated, and the deflections are measured using position-sensitive detection techniques, for example, scanning a narrow slit across the deflected beam and measuring the transmitted cluster intensity.

At present, polarizabilities have been measured for sodium and potassium clusters by Knight, Clemenger, de Heer, and Saunders (1985a) and for aluminum clusters by de Heer, Miľani, and Châtelain (1989).

A. Elementary theoretical considerations

A classical metal sphere responds to a uniform static electric field by a small uniform displacement of the conduction electrons, thereby creating a field that exactly cancels the applied field in the interior of the sphere. The induced dipole moment P is

$$P = \alpha E , \tag{5.2}$$

where $\alpha = R^3$.

Before turning to real clusters, we shall first briefly discuss the static response of simple metal surfaces. In the jellium model for a metal surface, Lang and Kohn (1973) found that the electronic density gradually reduces at the surface and extends significantly beyond the jellium edge. The jellium cluster radius is $R = N^{1/3} r_s$, where r_s is the bulk Wigner-Seitz radius (Kittel, 1976).

The spilled-out electronic charge density at the surface screens external fields. For sodium ($r_s = 4$ a.u.), the center of mass of the induced screening charge is about $\delta = 1.3$ a.u. beyond the planar jellium surface. Hence the image plane is located beyond the surface rather than at the surface as in the classical case. Moreover, the electronic charge density responds to applied fields approximately as if there were a perfect metal surface displaced a distance δ from the jellium surface.

Of course, real surfaces are more complex, and the actual screening lengths as well as ionic core effects may be important (see, for example, Smith *et al.*, 1989). This is especially the case for electronically dense metals (having small r_s). Here we treat the jellium sphere approach in

order to obtain a rudimentary description of polarizability. There have been several attempts to include ionic core effects, as briefly mentioned below, which seem to improve somewhat the correspondence between experiment and theory. Nevertheless, the basic conclusions from the jellium model appear to remain valid.

B. Polarizability of jellium spheres

The response of a jellium sphere to a static electric field is closely related to the response of the bulk surface: again, the charge density spills out and the image surface is located beyond the jellium boundary (Beck, 1984). Consequently the polarizability can be expressed approximately as (Snider and Sorbello, 1983b)

$$\alpha=(R+\delta)^3 . \tag{5.3}$$

From self-consistent polarizability calculations of jellium spheres in the local-density approximation (LDA; Beck, 1984; Ekardt, 1984a; Puska *et al.*, 1985), δ is estimated to be about 1.5 a.u. and depends slightly on r_s, R, and electronic shell structure. Similar results are also obtained in the much simpler Thomas-Fermi approximation (Kresin, 1989). The important conclusion is that the polarizability of small jellium spheres is increased compared with the classical value, caused by an effective increase in the cluster radius due to the spilling out of the electronic charge.

Local spin-density calculations using ionic core potentials by Moullet and Martins (1990b) predict more structure than is implied in Eq. (5.3). Both electronic shell effects and geometrical effects are apparent, giving rise to size-dependent variations in the polarizabilities. See also Sec. IV.B.1 of Brack (1993).

C. Experimental polarizabilities

1. Polarizabilities of sodium and potassium clusters

Polarizabilities of potassium and sodium clusters, originating from a high-temperature source, have been determined by measuring the deflections in a strong inhomogeneous electric field, as described above (Clemenger, 1985b; Knight *et al.*, 1985a; see also de Heer, Knight, *et al.*, 1987). The experimental results for sodium and potassium clusters are plotted in Fig. 22.

It is striking that the polarizabilities for corresponding clusters of sodium and potassium (normalized to their respective atomic polarizabilities) are nearly identical (Fig. 22). Note that even the bulk limits (i.e., r_s^3/α_1) of these two metals approximately scale. The generally decreasing trend agrees qualitatively with Eq. (5.3), and a reasonable fit to the data is obtained with a value $\delta=1.5$ a.u. (Clemenger, 1985b).

The shell structure is clearly borne out, causing a dip at 8 and one near 20. The polarizabilities of the midshell clusters between 8 and 20 rise to a maximum at 16. This is caused partly by the higher polarizabilities of the less tightly bound open-shell electrons (Puska *et al.*, 1985) and partly by ellipsoidal distortions (de Heer, Knight, *et al.*, 1987).

A slight temperature dependence of the polarizability is also discernible. For Na_{20} there are two values obtained with two different source conditions. Measurements on a colder cluster beam result in lower polarizabilities (Clemenger, 1985).

2. Polarizabilities of aluminum clusters

The polarizabilities of aluminum clusters have been measured using the same method as for the alkali clusters (de Heer, Milani, and Chatelain, 1989; Milani, Moullet, and de Heer, 1990). In this case, however, a laser vaporization cluster source was used and deflections were measured using a specially designed position-sensitive time-of-flight mass spectrometer (de Heer and Milani, 1991).

The results are plotted in Fig. 23, together with theoretical values. It is clear that the general trend for the aluminum clusters is quite different from the alkalis. For example, the polarizability increases from the atom to the dimer. Large oscillations are observed up to about

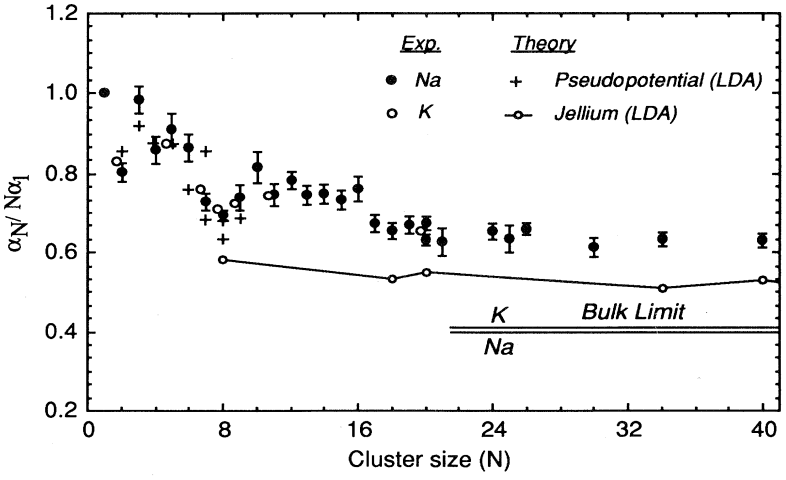

FIG. 22. Experimental polarizabilities of sodium and potassium clusters (after Knight *et al.*, 1985a, 1985b) compared with pseudopotential LDA calculations (Moullet *et al.*, 1990) and with self-consistent spherical jellium calculations (Ekardt, 1984b).

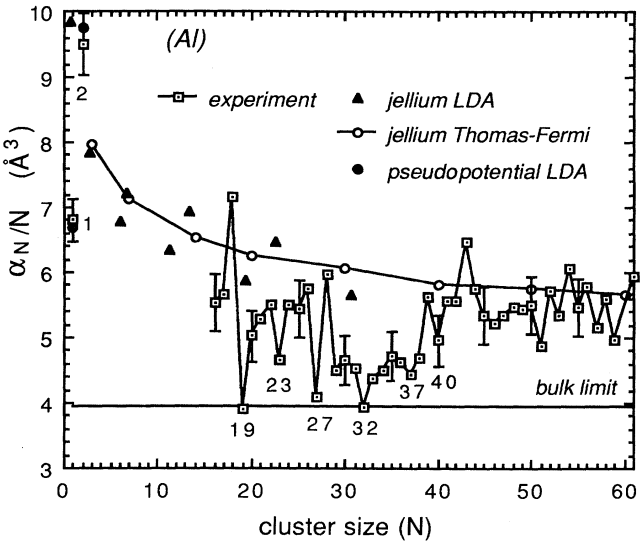

FIG. 23. Experimental polarizabilities of aluminum clusters (after de Heer and Milani, 1989) compared with spherical jellium calculations in the LDA by Puska *et al.* (1985); with spherical jellium calculations in the Thomas-Fermi approximation by Kresin (1992); and with pseudopotential LDA calculations (Milani, Moullet, and de Heer, 1990).

40. From 32 to about 42 the polarizability rises, and then recovers, followed by a gradual decrease. (Clusters between 3 and 15 have not been measured, due to limitations imposed by the ionizing photon energy.) Although the experimental uncertainties are significantly larger in these data than for the alkalis, the experimental trends are reliable enough to draw the general conclusions below.

D. Comparison with theory

Sodium and potassium per-atom polarizabilities have the generally decreasing trend expected from the jellium model (Fig. 22). The spherical jellium model calculated in the LDA, however, systematically underestimates the polarizabilities by about 15% (Beck, 1984; Ekardt, 1984a; Puska *et al.*, 1985).

On the other hand, calculations in the spin-dependent local-density approximation (LSDA), using ionic core pseudopotentials and optimized geometries, give almost perfect agreement with experiment (Moullet *et al.*, 1990a). This suggests that the jellium approximation is the source of the discrepancy rather than the LDA. Note, however, that recent calculations within the jellium model using a nonlocal approximation for the exchange and correlation give better agreement with experiment than the LDA (Rubio *et al.*, 1990, 1991b), supporting the opposite conclusion, so that the situation is not entirely clear.

The relatively enhanced polarizabilities of the open-shell clusters between 8 and 20 have also been approximately reproduced by the jellium model in the LDA. However, the values are again systematically about 15% too low (Puska *et al.*, 1985). In summary, for the alkalis, the jellium model predicts trends that roughly agree with experiment and with the simple picture of a metal sphere with spilled-out electronic charge.

For aluminum, the situation is more complicated. Theoretical predictions for spherical jellium calculations in the LDA (Puska *et al.*, 1985) and in the Thomas-Fermi approximation (Kresin, 1989) (Fig. 23) disagree with experiment most significantly for the smaller clusters. Related discrepancies with the jellium model are also observed in the ionization potentials. See also Sec. III.B of Brack (1993).

VI. PHOTOIONIZATION AND IONIZATION POTENTIALS

Photoionization of alkali and other simple metal clusters has been the subject of numerous investigations over the past 20 years, starting with the investigations of sodium clusters through Na_8 of Robbins *et al.* (1967). These studies have now been extended to clusters with hundreds of atoms per cluster. The photoionization process and the ionization potentials determined from photoionization are reviewed in this section, which is based on selected up-to-date results. Earlier studies are listed in the cited references.

Ionization potentials can also be measured from electron-impact-ionization studies. This method is experimentally somewhat easier to apply; however, the electron-impact phenomena tend to be more complex than those from photonic processes, causing some problems in the interpretation of the experimental data. For a discussion of this subject, see Rabin *et al.* (1991) and Jackschath *et al.* (1992).

By definition the ionization potential [or, more precisely, the adiabatic ionization potential (AIP)] of a cluster corresponds to the energy difference of the neutral and the ionized clusters in their ground states. Information on the adiabatic ionization potential can be obtained from photoionization measurements.

Photoionization involves the removal of an electron by a photon. This is a direct electronic process that does not change the position of the ionic cores; rather, the electronic system as a whole adjusts in the process of removing the electron. Assuming that a cluster is initially in the ground state (and ignoring zero-point vibrational motion), then the lowest-energy photon that can ionize the cluster corresponds to the vertical ionization potential (VIP).

The ground-state geometry of the neutral cluster and the ion are usually different, so that the photoionized cluster is vibrationally excited immediately after ionization. Hence a photoionization measurement on initially cold clusters yields the vertical ionization potential and

not the adiabatic ionization potential. For large clusters, shape differences between the neutral cluster and its ion are small, so that the adiabatic ionization potential and the vertical ionization potential are virtually identical. For small clusters this is not so, and the difference may be important.

In practical measurements the clusters are often initially hot, so that the ionization thresholds are not sharp. Careful analysis is required to determine the vertical ionization potential and the adiabatic ionization potential, as explained in more detail below.

A. Experimental methods

The experimental procedure applied in all of these studies is straightforward. Neutral cluster beams are ionized with light from a tunable laser or with monochromated light from an UV arc lamp source. The cluster ions are mass selected, and the signal is recorded as a function of the photon energy. The ion signal of a selected cluster ion is normalized with respect to the ionizing light intensity, giving the photoionization efficiency, which hence is proportional to the photoionization cross section. Figure 24 shows examples of photoionization efficiency spectra of several alkali clusters. With increasing photon energy, the structure of a typical photoionization efficiency spectrum (of hot clusters, see below) is characterized by a gradual onset at threshold, after which there is a relatively steep rise reaching a maximum after a few tenths of an eV, followed with broad post-threshold features and a gradual decline. For cold clusters, sharper features are distinguished (see below). The interpretation of the photoionization efficiency spectra is discussed below after a general discussion of the photoionization process.

B. Photoionization in clusters

Photoionization spectroscopy has been extensively applied to polyatomic molecules, and the processes involved are treated by Guyon and Berkowitz (1971; Berkowitz, 1979). Their discussions are relevant for metal clusters as well. However, there are several important aspects more specific to metal clusters that are briefly discussed here.

Figure 25 illustrates the photoionization process for Na_9, showing the total-energy curves of the cluster and its ion as a function of shape (as determined from the ellipsoidal shell model; see Appendix C). Note the shape change from the prolate shape of a 9-electron cluster to the spherical shape of an 8-electron cluster as calculated in the ellipsoidal shell model. Large changes of shape are

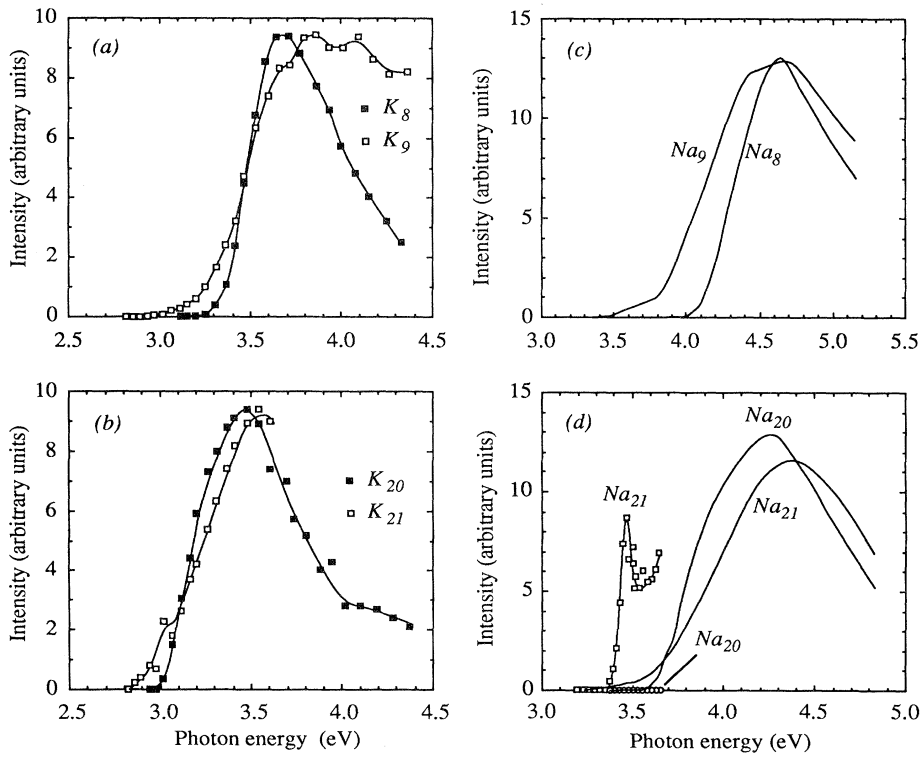

FIG. 24. Photoionization efficiency measurements of sodium and potassium clusters: (a) K_8 and K_9; (b) K_{20} and K_{21} (after Saunders *et al.*, 1985); (c) Na_8 and Na_9; and (d) Na_{20} and Na_{21} (by Kappes *et al.*, 1988). Shown also in (d) are measurements of Na_{20} (boxes) and Na_{21} (circles) by Homer *et al.* (1992), who used a cooled laser vaporization source.

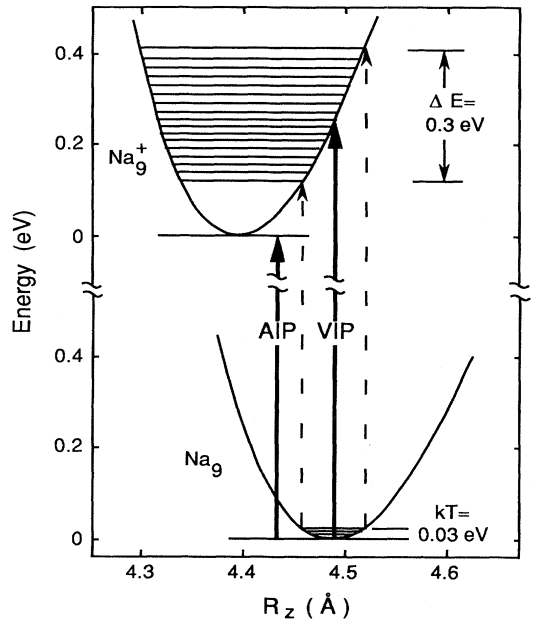

FIG. 25. Schematic diagram of the photoionization process $Na_9 \rightarrow Na_9^+ + e$. The total energy of the cluster as determined in the ellipsoidal shell (Clemenger-Nilsson) model for the ground state, and the ionized state is shown as a function of the long axis of the cluster (R_z). The thermal shape oscillations in the ground state give rise to a large bandwidth of excited vibrational states, causing extended thermal tails in the photoionization efficiency spectra. AIP, adiabatic ionization potential; VIP, vertical ionization potential.

typical for small clusters of simple metals (see, for example, the Nilsson diagram, Fig. 53) and have important consequences for the ionization process. According to the Franck-Condon principle (Berkowitz, 1979), the most probable electronic transitions are those in which the geometry does not change. These correspond to vertical transitions, and the energy required is indicated in Fig. 25. On the other hand, the adiabatic ionization potential corresponds to transitions from the ground state of the neutral cluster to the ground state of the ion. If large shape changes are involved and the cluster is cold, then this transition is quite unlikely.

Nonzero initial temperatures reduce the minimum photon energy needed to ionize the clusters and cause thermal tails on the photoionization efficiency curves, as illustrated in Fig. 25. For a hot cluster the shape oscillates. The magnitude of the thermal quadrupole shape oscillations is estimated from the classical turning points of the shape oscillations, i.e., where the potential energy is kT (for details, see Appendix C). The thermal width of the ionizing transition is estimated as the difference in energy between the vertical ionizing transitions at the two classical turning points, as indicated in the figure. In this case, assuming that $kT=0.03$ eV (≈ 300 K), the extent of the thermal tail is about 0.3 eV (Appendix C). Note that this is an order of magnitude larger than kT. The large amplification is due to the large difference in the equilibrium shapes and the "softness" of the cluster, causing large shape oscillations even at relatively low temperatures. Of course, this model is crude, but it should give a reasonable estimation for this effect.

Other thermal effects include the thermal smearing of the electronic states, i.e., when the energy gaps are comparable to kT, as is the case for larger clusters.

The shapes of the photoionization efficiency spectra are sensitive not only to the vibrational state of the cluster but also to electronic final-state effects. Although Wigner (1948) has shown that at threshold the electronic contribution to the photoionization efficiency is a step function, no simple general statement can be made about post-threshold structure. In fact, due to interference of the outgoing electronic wave function and the initial-state wave function, the ionization efficiency may even vanish above the ionization threshold, producing Cooper minima (Cooper, 1962; Berkowitz, 1979, p. 44). The sodium atom is an important example of this effect.

In summary, with increasing photon energy, the photoionization efficiency spectra of typical simple metal clusters are expected to have very low values at the adiabatic ionization potential, increasing at least up to the vertical ionization potential. The energy difference between the vertical ionization potential and the adiabatic ionization potential generally decreases with increasing size. Hot clusters may have thermal tails that far exceed kT in their extent. The shape of the photoionization efficiency curve near threshold depends on the temperature, the initial and final states of the cluster, and quantum-mechanical details of the transition, such as the final density of states of the emitted electron.

C. Photoionization efficiency spectra and their interpretation

Figure 24 shows photoionization efficiency spectra of K_8, K_9, K_{20}, K_{21}, Na_8, Na_9, Na_{20}, and Na_{21}. The potassium spectra are from Saunders *et al.* (1985; Saunders, 1986; see also de Heer, Knight, *et al.*, 1987) and were obtained using a supersonic nozzle source. The sodium spectra are from Kappes *et al.* (1988) and from Homer, Persson, Honea, and Whetten (1992; see also Persson, 1991 and Whetten *et al.*, 1992). Kappes *et al.* used a supersonic nozzle source, whereas Whetten *et al.* used a liquid-nitrogen-cooled laser vaporization source.

There are clear similarities between the spectra of clusters with the same number of atoms of the two metals. The 9-atom and 21-atom clusters both have extended tails near the threshold, which extend considerably further into low energies than those of the 8- and 20-atom clusters.

The temperature effect on the photoionization efficiency curves is dramatically demonstrated in Fig.

24(d) in the photoionization efficiency curve of Na_{21} obtained with the cold source. Here a sharp feature is found at 3.5 eV, whereas for the hot source only an extended tail is observed. In fact, for larger sodium clusters from a cold source, similar sharp features are observed in the photoionization efficiency spectra of many clusters with an odd number of atoms (Persson, 1991; Homer *et al.*, 1992).

From the above discussion, it is clear that determining the ionization potentials from photoionization efficiency spectra may be complicated, especially if the clusters are hot. Various schemes for analyzing photoionization efficiency spectra have been devised for polyatomic molecules (for reviews, see Guyon and Berkowitz, 1971 and Berkowitz, 1979), and attempts have been made to adapt these for clusters. However, it is unlikely that any one procedure applies for all cases. The smaller clusters, in particular, form a separate group, because the neutral and ion shape differences are greatest. Nevertheless, several general methods are employed.

A method proposed by Watanabe (1954) derives the adiabatic ionization potential from the first post-threshold break from linearity of the logarithm of the photoionization efficiency. In principle this method applies for diatomics, but it has been demonstrated to fail for several polyatomic systems (Guyon and Berkowitz, 1971). Attempts have been made to improve it, as, for example, in the pseudo-Watanabe method (Kappes *et al.*, 1988), but theoretical justification is weak.

More often the ionization potentials are determined by extrapolating the first linear rise in the photoionization efficiency spectrum. The baseline intercept of this extrapolation is assumed to correspond to the adiabatic ionization potential. Although there is no sound theoretical justification for this method either (except for diatomic molecules under certain conditions; Guyon and Berkowitz, 1971), it is at least straightforward and can be consistently applied to extended series of cluster sizes.

A more recent model by Limberger and Martin (1988) assumes harmonic-vibrational oscillations of equal frequencies for the neutral and the ionized cluster, and the ion potential is shifted with respect to the neutral (as in Fig. 25; see also Appendix C). With the further assumption that photoionization efficiency is a step function for the ionizing transition from a specific initial vibrational state to a specific final vibrational state, the position of the first maximum in the first derivative of the photoionization efficiency curve corresponds in this case with the vertical ionization potential.

For large clusters the model is extended and assumes that the net broadening effect may be represented by sums of error functions (Limberger and Martin, 1988). At least four parameters are used to fit the model to the data, from which the ionization potentials are extracted. This model has been used to analyze carefully the photoionization efficiency spectra of large, slightly oxidized Cs clusters (Bergmann *et al.*, 1988; Limberger and Martin, 1989) with convincing results.

D. Experimental ionization potentials

1. Alkali clusters

The ionization potentials of sodium and potassium clusters plotted in Fig. 26(a) have been derived from photoionization efficiency spectra using the baseline intercept procedure described above. Figure 26(b) also shows the highest occupied levels from the ellipsoidal shell model, scaled with the Fermi energy.

For the potassium data (Saunders *et al.*, 1985; Saunders, 1986; de Heer, Knight, *et al.*, 1987) a supersonic nozzle source was used. The sodium cluster ionization potentials were compiled from experimental values from Kappes *et al.* (1988), Homer *et al.* (1992), and Persson (1991), using the linear extrapolation method. Where the measurements overlap, the agreement is generally reasonable. There is an important exception for $N=21$, where Kappes *et al.* conclude from their analysis that the ionization potential of 21 is greater than that of 20. This contradicts Whetten's determinations [see Fig. 24(d) and the discussion above].

Major steps in the ionization potentials are observed at 8, 18, 20, 40, 58, and 92. These are superimposed on a decreasing curve. Also observed are several minor steps. Note that many of these features are qualitatively reproduced in the ellipsoidal shell model. The general decrease is primarily caused by electrostatic effects, which are discussed below.

The large steps correspond to the spherical shell-closing numbers, while the fine structure corresponds to subshell closings in ellipsoidally distorted clusters. Quantitatively (when scaled with the Fermi energy), most of the observed features agree with the ellipsoidal shell-model step sizes within a factor of 2 or better.

Besides the shell-closing steps, strong odd-even alternations are observed over most of the investigated range (Fig. 26). For $N<20$, the fine structure in the sodium data is more pronounced but qualitatively similar to the potassium data. This is qualitatively consistent with the energy scaling in the shell model, although the odd-even alternations found for sodium clusters are substantially larger than expected from the shell model.

Moreover, the odd-even effects are pronounced in photoionization efficiency spectra of sodium clusters. The odd-even alternation observed in the ionization potentials is possibly related to spin-pairing effects, but is not yet satisfactorily explained. In fact, more recent data (Homer *et al.*, 1992) show that the odd-even alternation continues for clusters with well over 100 atoms per cluster.

The tails on the photoionization efficiency curves of sodium clusters from the supersonic nozzle source range from about 0.1 eV (for 12, 13, and 14) to 0.24 (for 6) and 0.35 eV (for 9), with intermediate values for the others (Kappes *et al.*, 1988). These values are consistent with those obtained from analysis of the thermal tails given above in Sec. VI.B. Generally, long thermal tails of hot clusters are due to large differences in the shapes of the

neutral cluster compared with the ion, as determined from the Clemenger-Nilsson diagram. For a further discussion, see Appendix C.

Recently the ionization efficiencies of lithium clusters have been measured by Dugourd *et al.* (1992) on clusters from a high-temperature source. The ionization potentials extracted using linear extrapolation measurements are shown in Fig. 26(d). Large steps are found at 8 and 16, but there are no steps at 18 or 20, in contrast with the shell model. Odd-even alternations persist over the measured range of cluster sizes.

The ionization potentials of pure cesium clusters ($N<15$) and singly oxidized cesium clusters ($N<130$) have been determined by Limberger and Martin (1989) and for cesium clusters with $N<600$ by Bergmann *et al.* (1988). From the combined data electronic shell steps in the photoionization efficiencies are found for systems with 8, 20, (34), 40, 58, 92, 138, 198, 254, 338, 440, and 562 free electrons, in agreement with the shell model.

2. Aluminum and indium clusters

The photoionization efficiency spectra of Al clusters have been measured on clusters produced in a laser vaporization source and photoionized with a tunable UV laser (Schriver *et al.*, 1990; Persson, 1991; Persson *et al.*, 1991). The adiabatic ionization potentials were determined with the baseline intercept method, and the results are shown in Fig. 27.

The ionization potentials (IPs) show steps that correspond with electronic shell closings as shown in Fig. 27. There is some disagreement with the shell model, however. For example, the IPs increase from the atom to the dimer to the trimer is not expected; the steps expected at the 1*g*, the 3*s*, and the 3*p* closings are not observed. The large step at 36 and 37 is not predicted, although this could be due to a slightly altered shell-filling order compared with the model describing alkalis (Sec. II). Other anomalies are thought to be due to crystal-field splittings

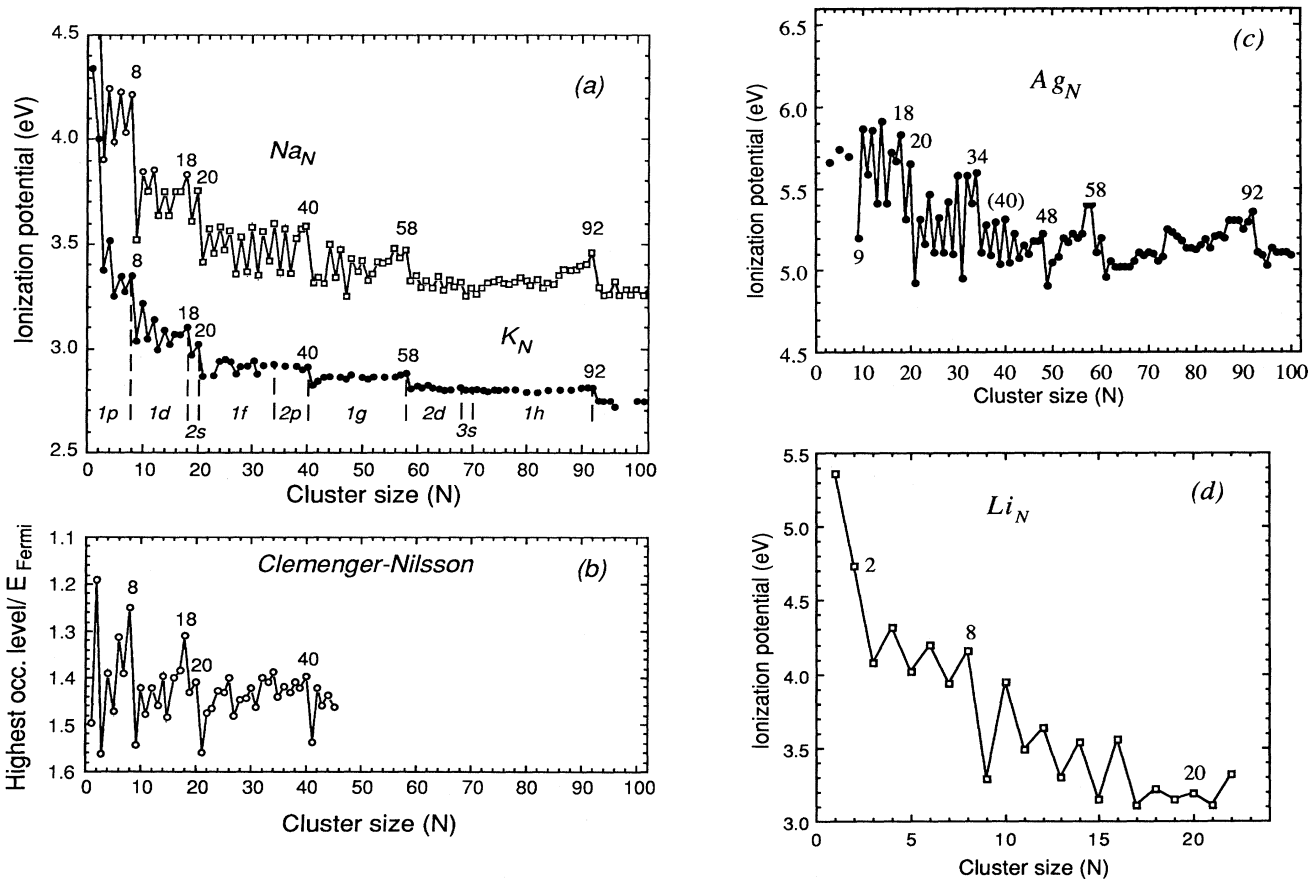

FIG. 26. Ionization potentials of alkali clusters. (a) Ionization potentials of sodium clusters (after Homer *et al.*, 1993, to be published) and of potassium clusters (Saunders *et al.*, 1985; de Heer, Knight, *et al.*, 1987); (b) highest occupied levels in the ellipsoidal shell (Clemenger-Nilsson) model where the electronic kinetic energy is scaled relative to the Fermi energy of the bulk metal; (c) ionization potentials of silver clusters (after Alameddin *et al.*, 1992); (d) ionization potentials of lithium clusters (Dugourd *et al.*, 1992).

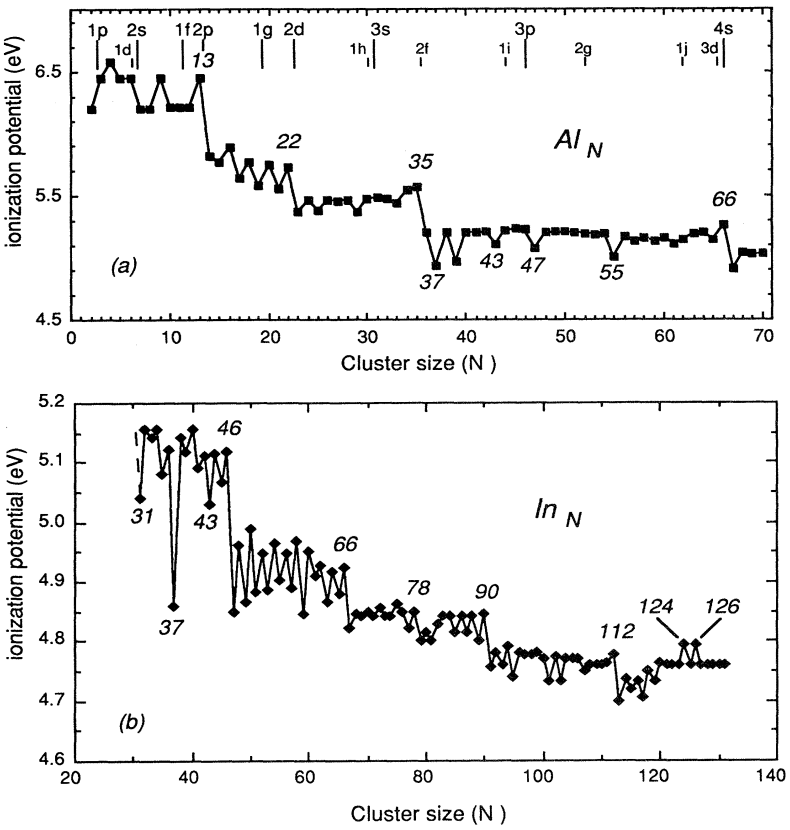

FIG. 27. Ionization potentials of trivalent clusters. (a) Ionization potentials of aluminum clusters (after Schriver *et al.*, 1990). Spherical-shell-closing numbers predicted for this trivalent metal are shown. (b) Ionization potentials of indium clusters (after Pellarin *et al.*, 1992, 1993).

and *sp* hybridization effects. Related discrepancies have also been observed in the polarizabilities of aluminum clusters (see Sec. V.C.2).

The ionization potentials of indium clusters over a comparable size range have been reported by the same authors and are qualitatively similar to those of aluminum (Persson, 1991; Persson *et al.*, 1991). Recent measurements by Pellarin *et al.* (1992, 1993) are shown in Fig. 27(b). The steps at 46, 66, and 112 correspond with electronic shell closings; however, the dip at 37 may be anomalous.

3. Silver clusters

The ionization potentials of silver clusters with up to 440 atoms per cluster were measured by Alameddin *et al.* (1992). The clusters were produced in a liquid-nitrogen-cooled laser vaporization cluster source, and the ionization potentials were determined using the baseline intercept method. The ionization potentials have large steps at $N=8$, 18, 20, 30, 34, 48, 58, 60, and 92 [see Fig. 26(c)], while odd-even steps (similar to those for sodium) are found up to $N=49$. The ionization potentials as a function of size follows a general decreasing trend, as they do for sodium. The ionization potentials of silver clusters from Ag_1 to Ag_{36} have also been measured by Jackschath *et al.* (1992). The clusters were produced in a gas-aggregation source (see Sec. III). The measurements were performed by electron-impact ionization, where the cluster beam was subjected to an electron beam. The ion signal was recorded as a function of the electron energy. Near threshold the ionization efficiency curves have two pairs: a rather extensive (≈ 1 eV) curved section followed by a linear rise. The data were analyzed by extrapolating the linear rise to the baseline, and the lower-energy curved sections were not considered. Hence the baseline intercepts were interpreted as upper limits for the vertical ionization potential (Jackschath *et al.*, 1992). These data roughly agree with those of Alameddin *et al.* (1992). It would be interesting to better understand the reason for the different values resulting from the photoionization and electron-impact ionization studies. However, since the photoionization studies systematically produce lower values for the ionization potentials, it is reasonable to assume that they are more accurate.

E. Comparison with conducting-metal-sphere and semiclassical models

Above we have seen that an important part of the fine structure in the ionization potentials is related to electronic shell effects. Here we discuss the overall decreasing trend found for essentially all metal cluster systems.

A simple model for the ionization potential is to treat the cluster as a classical conducting sphere. In this mod-

el there are two contributions to the energy needed to remove an electron; one is the binding energy of the electron in the metal, i.e., the work function, and the other is the electrostatic contribution, which reflects the electrostatic energy of a small charged system in the ionized state. The electrostatic contribution is found from elementary considerations and is $e^2/2R$, where R is the radius of the sphere; in the infinite limit, the ionization potential approaches the work function. Hence the conducting-sphere model gives for the ionization potential and the electron affinity (EA),

$$\begin{aligned} \mathrm{IP} &= \mathrm{WF} + \alpha e^2/R \ , \\ \mathrm{EA} &= \mathrm{WF} - \beta e^2/R \ , \end{aligned} \tag{6.1}$$

where WF is the polycrystalline bulk work function and $\alpha=\beta=\frac{1}{2}$ in the classical model (Makov *et al.*, 1988; Perdew, 1988; de Heer and Milani, 1990). Note that Eq. (6.1) is most easily derived by assuming a small but nonzero radius for the classical electron and identifying the ionization potential thus derived for infinite R with the work function (de Heer and Milani, 1990).

The simple electrostatic model resembles spherical jellium results which predict that the classical radius should be understood to be equal to $R'=R+\delta$ (Perdew, 1988), where R is the radius of the positive jellium sphere and δ is related to the electron spillout and estimated to be about 1.5 a.u. This correction reduces the IP's compared with the classical result.

In contrast, more recently Seidl *et al.* (1991a, 1991b) found from semiclassical density-variational calculations that the spillout and other quantum-mechanical effects change the classical value of α and β to about $\alpha=0.4$ for the ionization potential and $\beta=0.6$ for the electron affinity (see Sec. V.B.3 of Brack, 1993). They further extended Eq. (6.1) to second order, giving

$$\begin{aligned} \mathrm{IP} &= \mathrm{WF} + \alpha_1 e^2/R + \alpha_2 (e^2/R)^2 \ , \\ \mathrm{EA} &= \mathrm{WF} - \beta_1 e^2/R - \beta_2 (e^2/R)^2 \ . \end{aligned} \tag{6.2}$$

The α and β values depend slightly on the Wigner-Seitz radius r_s (Kittel, 1976). Very similar results for α and β were also found by Engel and Perdew (1991) from a $1/R$ correction to the chemical potential.

To test these predictions, the measured IPs are plotted as a function of e^2/R [Figs. 28(a), 28(b)]. The curves are second-order fits to the closed-shell clusters, and all cases are very reasonable approximations. The fitting values are, for K, $\alpha_1=0.32$, $\alpha_2=0.30$; for Na, $\alpha_1=0.44$, $\alpha_2=-0.27$; for Ag, $\alpha_1=0.34$, $\alpha_2=-0.01$; and for Al, $\alpha_1=0.45$, $\alpha_2=-0.08$, where atomic units are used in the expansion (i.e., $e^2/r_0=1$).

The slopes α_1 are all reasonably close to the value predicted by Seidl *et al.* (1991a); but the second-order terms agree only qualitatively. Note also the important discrepancies for small aluminum clusters, which are probably due to failure of the jellium model for these clusters (de Heer, Milani, and Châtelain, 1989).

Lithium is clearly anomalous [Fig. 28(b)]. Although a linear fit through the measured points has a slope ($\alpha_1=0.41$) reasonably consistent with jellium predictions, it extrapolates to 2.0 eV compared with the bulk work function 2.9 eV. Besides, the missing step at 20 is puzzling. These are important failures of the jellium model and remain to be explained. Note, however, that the *ab initio* quantum-chemical calculations by Boustani *et al.* (1987) correspond very well with the measured values for $N \leq 10$.

It is worth mentioning that the classical values of α_1 and β_1 have been a subject of some controversy (Bréchignac *et al.*, 1989b), and often the value $\frac{3}{8}$ is quoted for α_1 and $\frac{5}{8}$ for β_1 (Wood, 1981). Although the argument leading to these values is erroneous (Macov *et al.*, 1988; Perdew, 1988; de Heer and Milani, 1990), they are

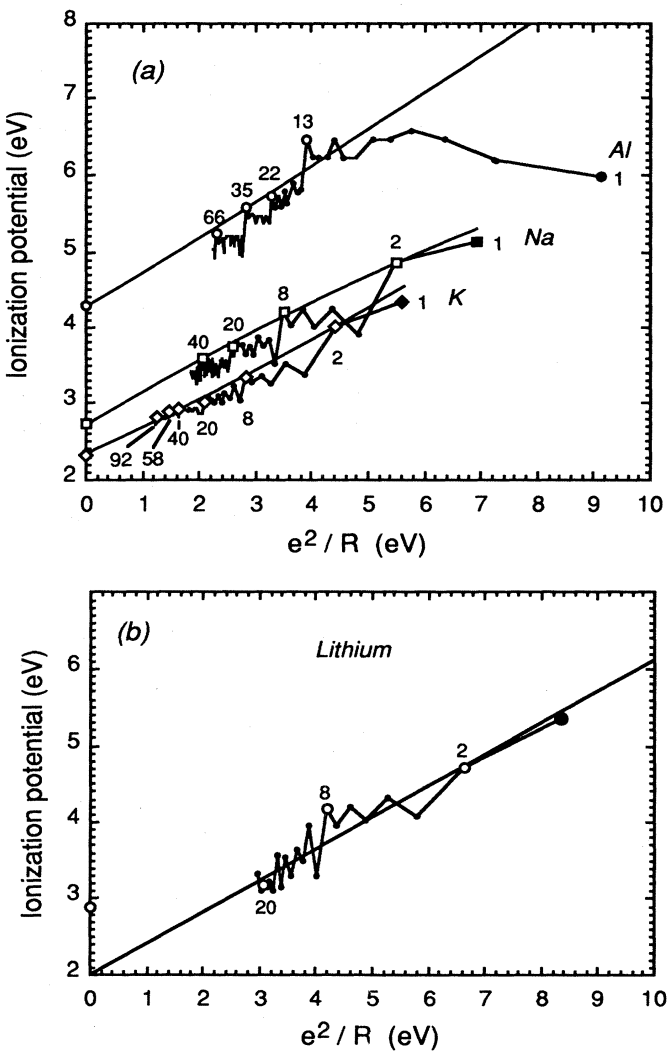

FIG. 28. Experimental ionization potentials (a) for Na, K, and Al clusters plotted against e^2/R, where R is the classical cluster radius. Lines are parabolic fits to the closed-shell clusters and the bulk work function. The fit parameters are given in the text. (b) for lithium clusters, plotted as in (a).

rather close to the values found by Seidl *et al.* (1991a). It is perhaps worthwhile to inspect more closely this curious coincidence. It turns out that the $\frac{3}{8}$ value results when one calculates the work required to remove an electron with radius $r=0$ from a distance d from the *surface* of a classical metal sphere with radius R, where d is taken to be *independent* of the R. The $\frac{1}{2}$ results by calculating the work required to move an electron with infinitesimal r (with r independent of R) from the *interior* of the classical metal sphere to infinity. While the second procedure correctly describes the classical solution, the first appears to more correctly describe the quantum-mechanical one, at least for jellium spheres. It would be interesting to understand why this is so. For further discussions of the classical and semiclassical models, see Sec. V.B of Brack (1993).

F. Further comparison with theory

Self-consistent spherical (Chou *et al.*, 1984) and spheroidal (Penzar and Ekardt, 1991) jellium calculations in the LDA have predicted the ionization potentials for small alkali clusters. For potassium clusters the self-consistent spherical calculations predict steps at the shell closings for 8, 18, 20, 34, 58, and 92 electrons. These steps correspond generally with those found experimentally. An important discrepancy is that the observed step at 40 is not predicted and the predicted large step at 34 is in reality rather weak, corresponding more likely to a subshell closing of a deformed cluster.

The missing step at 40 is important, since experimentally this is certainly a major shell closing (as it is in the shell model). Note, however, that a step at 40 is predicted for clusters with smaller Wigner-Seitz radii r_s (i.e., Na and Li; Chou *et al.*, 1984). These effects remain to be explained.

Measured and calculated ionization potentials for sodium clusters are shown in Fig. 29. It is seen that the values predicted in the self-consistent jellium model are not too impressive [Fig. 29(b)]. In particular, spherical jellium does not reproduce the fine structure partly due to ellipsoidal distortions (Sec. II) and partly to crystal-field effects. More sophisticated approaches are required to understand these.

Self-consistent spheroidal jellium calculations on sodium clusters (Penzar and Ekardt, 1991) qualitatively reproduce some of the fine structure, but the size of the shell steps are much larger than observed [Fig. 29(b)]. The calculations are indeed improved by removing the spherical constraint, but the agreement with experiment is still rather poor. Although large discrepancies might be expected for the smallest clusters, the systematic overestimations up to about 0.5 eV between 9 and 20 are disconcerting. See Brack (1993) for further corrections.

First-principle quantum-chemical calculations (Boustani *et al.*, 1987; Bonacic-Koutecky *et al.*, 1991) prove more realistic than jellium, where they are feasible, i.e., for the smaller clusters [Fig. 29(a)]. Note, however, that

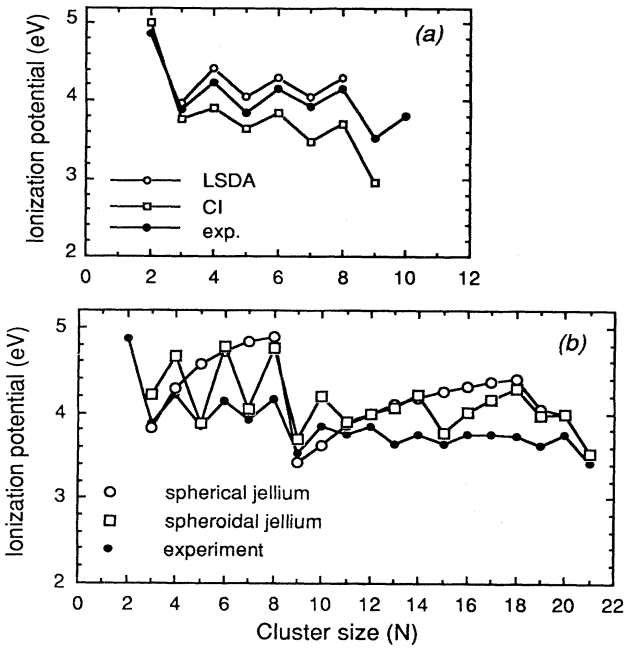

FIG. 29. Comparison of experimental ionization potentials for Na clusters with various theories: (a) with local spin-density calculations (by Martins *et al.*, 1985) and configuration-interaction, *ab initio* calculations by Bonacic-Koutecky *et al.* (1991); (b) with spherical jellium in the LDA by Chou *et al.* (1984) and spheroidal jellium in the LDA by Penzar and Ekardt (1991).

agreement seems to degrade with increasing size, perhaps as a result of the increasing computational difficulties in these already very large systems.

Pseudopotential calculations in the LSDA (Martins *et al.*, 1985) give very good results for the small size range for which they were attempted [Fig. 29(a)]. This is an encouraging result, since it shows that the inaccuracies of the jellium approaches are indeed due to missing ionic structure and not to the LDA. See Brack (1993) for a review.

G. Conclusion

On the basis of very simple models, the ionization potentials of small alkali clusters (except Li) are reasonably well understood. The general decrease is explained from electrostatic considerations. The superimposed fine structure is caused by size-dependent variations of the position of the highest occupied level and is qualitatively explained in the ellipsoidal shell model. Further structure is primarily ascribed to spin- and crystal-field effects. The strong odd-even alternations in Na clusters is particularly intriguing and awaits a convincing theoretical explanation. The anomalous results for lithium clusters are also intriguing.

In the experimental data for aluminum, other factors are also important. Up to $N=13$, the ionization poten-

tial does not decrease, whereafter it generally follows the simple model. Here the ionization potential steps are related to electronic shell structure, with some modifications ascribed to hybridization and crystal-field effects. Correspondence with the jellium model improves with increasing size.

Quantum-chemical calculations are reasonably successful in calculating ionization potentials. Regrettably, they are computationally very difficult for clusters with more than ten or so atoms. Pseudopotential calculations in the LSDA give the best agreement with the experimental values and are at the same time computationally less demanding than first-principles quantum-chemical methods. The much simpler jellium calculations are most useful for larger clusters, but there are important discrepancies for small clusters.

VII. PHOTOELECTRON SPECTROSCOPY AND ELECTRON AFFINITIES

A. Introduction

An important limitation of photoionization spectroscopy is that the final state of the emitted electron is not determined, making it difficult to interpret the photoionization efficiency spectra. For example, photoionization efficiency post-threshold structure may be interpreted in terms of ionization from lower-lying electronic levels, but it may also reflect final-state effects. In contrast, the kinetic energy of the emitted electron is measured in photoelectron spectroscopy. The difference between the absorbed photon energy and the electron kinetic energy represents the energy needed to remove the electron from the cluster, and therefore the vibronic energy difference between the initial and final states.

Extending the spherical model described in Sec. VI.E [Eq. (61)], we find that the energy of the emitted electron is (for an anionic cluster)

$$U=h\nu-\left[E_n-\beta\frac{e^2}{R}\right], \tag{7.1}$$

where E_n corresponds to the single-particle energies. In this simplified model it is assumed that only one electron is removed, leaving a single hole. More complex excitations are ignored. Hence from this point of view the photoelectron spectrum of a specific cluster consists of lines corresponding to the energy levels E_n.

More generally, the correspondence between the photoelectron spectrum and the density of electronic states also involves the electronic and geometric structure of the final state. This causes broadening of the lines (see below) and other features related to higher excited final states (i.e., final states with more than one hole). Other processes, where the electron loses energy while leaving the cluster, are observed, so that the photoelectron spectra are slightly dependent on the energy of the incident photon (see Chesnovsky *et al.*, 1990). Nevertheless, usually photoelectron spectra are plotted with the "electron binding energy" (defined as the difference between the energy of the incident photon and the emitted electron) as the abscissa. Although this is not strictly correct (see below), it is helpful as a first step towards a more complete interpretation.

Usually mass-selected anionic clusters are used for photoelectron spectroscopy studies (as originally suggested by Leopold, Ho, and Lineberger, 1987). Since the electron affinity of a cluster is less than the ionization potential by about e^2/R [see Eq. (6.1)], a photon of given energy can probe energy levels of anions further below the Fermi level than of the corresponding neutrals. Nevertheless, photoelectron spectroscopy can also be performed on neutral cluster beams not selected in mass, but this is more difficult. In that case, not only the electron energy, but also the ion mass, must be determined in coincidence. This technique has been developed primarily by Rademann *et al.* (1987) for mercury clusters. (For a review, see Rademann, 1989.) For a recent review of photoelectron spectroscopy of metal clusters by a researcher active in the field, see Meiwes-Broer (1993).

B. Magnetic-mirror photoelectron spectrometer

For most photoelectron studies on clusters, the energy of the emitted electron is measured using a magnetic-mirror spectrometer (Kruit and Read, 1983). The principle of the magnetic mirror is to direct the photoelectrons towards an electron detector. The flight time of the electrons from the cluster to the detector is measured so that its velocity and hence its energy may be determined.

A schematic diagram of the spectrometer is shown in Fig. 30. Mass-selected cluster anions are illuminated with a short light pulse, usually from an excimer laser. An electron is ejected in a random direction in a high magnetic field. The electron follows the field lines towards the detector (where the magnetic field is low) without changing its speed. The electron detector is typically about a meter away from the ionization region, so that accurate time-of-flight measurements can be made.

The mirror action relies on the invariance of the magnetic moment μ of the electron in a magnetic field and on conservation of energy U,

$$\mu=\frac{mv_{\text{perp}}^2}{2H}, \qquad U=\frac{mv^2}{2}, \tag{7.2}$$

where v_{perp} is the component of velocity perpendicular to the magnetic field. If the cluster is ionized in a strong field, then it will spiral towards lower fields and the velocity will become essentially parallel with the magnetic field. The ratio of the high to low field is large (typically several hundred) to reduce the perpendicular component as much as possible, since only the parallel velocity component can be determined in the time-of-flight measure-

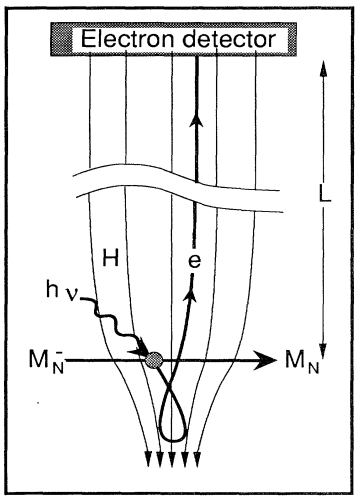

FIG. 30. Magnetic-bottle photoelectron spectrometer. Photoelectrons from cluster anions are repelled out of the high-magnetic-field regions and projected towards the electron detector. The time of flight of the electrons is measured.

ment. The most important feature of this spectrometer is its very large detection efficiency, since almost all electrons are detected irrespective of the direction in which they were originally emitted. Further details may be found in Ganteför *et al.* (1988, 1988b), Chesnovsky *et al.* (1987), and Kruit and Read (1983).

C. Experimental results

1. Photoelectron spectroscopy of alkali clusters

Photoelectron spectra for Na_N^- $(1 \le N \le 5)$, K_N^- $(1 \le N \le 7)$, Rb_N^- $(1 \le N \le 3)$, and Cs_N^- $(1 \le N \le 3)$ have been recorded by Bowen and co-workers (McHugh *et al.*, 1989; Eaton *et al.*, 1992). More recently, spectra for K_N^- up to $N=19$ have been recorded by the same group (Eaton *et al.*, 1992). The clusters are produced in a supersonic nozzle source and negatively ionized by electron attachment with an electron source close to the nozzle. These spectra are taken using a conventional hemispherical electron-energy analyzer (as in Leopold *et al.*, 1987 for Cu clusters).

The photoelectron spectra are reproduced in Figs. 31 and 32. Spectra of different alkali clusters with the same N are clearly related in the four cases, the main difference residing in the overall energy scale, which is largest for Na and smallest for Cs (Fig. 31). The spectra for the smaller clusters (up to K_5^-) have been interpreted by Bonacic-Koutecky *et al.* (1989), who calculated the transition energies (but not the transition strengths) using *ab initio* quantum-chemical methods (see also Bonacic-Koutecky *et al.*, 1991).

The following analysis is based on Eq. (7.1). In this interpretation the structure in the photoelectron spectra is essentially a fingerprint of the electronic density of states, which is further assumed to be crudely represented by the energy levels in the ellipsoidal shell model (Fig. 5). This highly simplified interpretation is justified primarily by its success, since detailed correspondences are found between the experimental data and the model (Eaton *et al.*, 1992). However, this interpretation must be considered with caution. For example, spin effects that may be important are ignored.

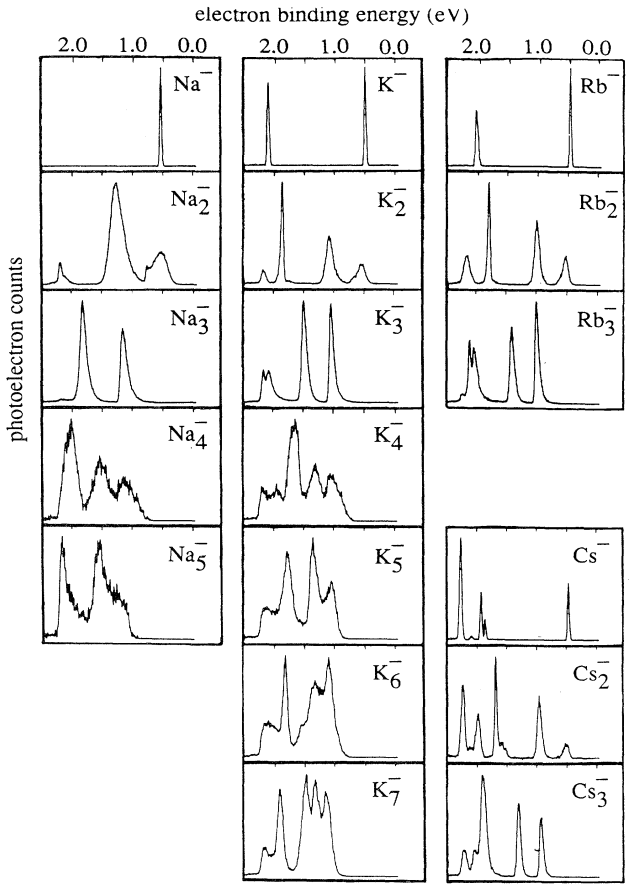

FIG. 31. Photoelectron spectra of small alkali cluster anions. After McHugh *et al.*, 1989.

It is instructive first to consider the alkali atom anions. For Na^-, one peak is observed. For K^- and Rb^-, there are two, and for Cs^- there are several peaks. The peak with lowest binding energy corresponds to a transition from the ground state of the ion to the ground state of the neutral. The higher-energy peaks are caused by higher excitations, where one of the two valence electrons of the anion is emitted and the remaining one is promoted to an excited state (McHugh *et al.*, 1989). Only the lowest-binding-energy peak corresponds with an energy level in the shell model, since it corresponds to a one-electron transition (i.e., from a bound state to the continuum).

Features arising from more complex transitions, i.e., transitions involving several electrons, do not correspond with energy levels in the shell model. Nevertheless, crude estimations can be made of the energies involved. It is found that, generally, single-electron transitions contribute to lower-energy features in the photoelectron spectra compared with those from more complex excitations (since then not only is an electron removed, but, in addition, one or several others are excited). Hence, in this simplified model, the spectra are analyzed assuming that the low-binding-energy features are due to single-electron excitations only.

For the dimers, two low-energy peaks are observed, which may correspond to the occupied states of the dimer anion, i.e., $(1s)^2$ and the $1p_x$ states (using shell-model notation; Sec. II). The two trimer peaks likewise correspond to $(1s)^2$ and the $(1p_x)^2$ states. Again, the peaks at higher energies correspond to more complex final states. Continuing with 4- and 5-atom anions, an additional peak is observed in the spectra corresponding to the $1p_y$ levels in the anion.

This is followed by the filling of $1p_z$ in 6^- and 7^- clusters, giving the corresponding additional peaks in the spectra. In spherical models the p_z, p_y, and p_z states are degenerate; however, in reality, and in particular for the closed-shell 7-cluster, they are split by crystal-field effects (see Sec. II.B, Fig. 5, and Röthlisberger and Andreoni, 1991).

This analysis continues through the $1d$ shell (see spectra in Fig. 32). The electronic binding energies deduced from photoelectron spectroscopy are shown in Fig. 33(a), and the single-particle levels from the ellipsoidal shell

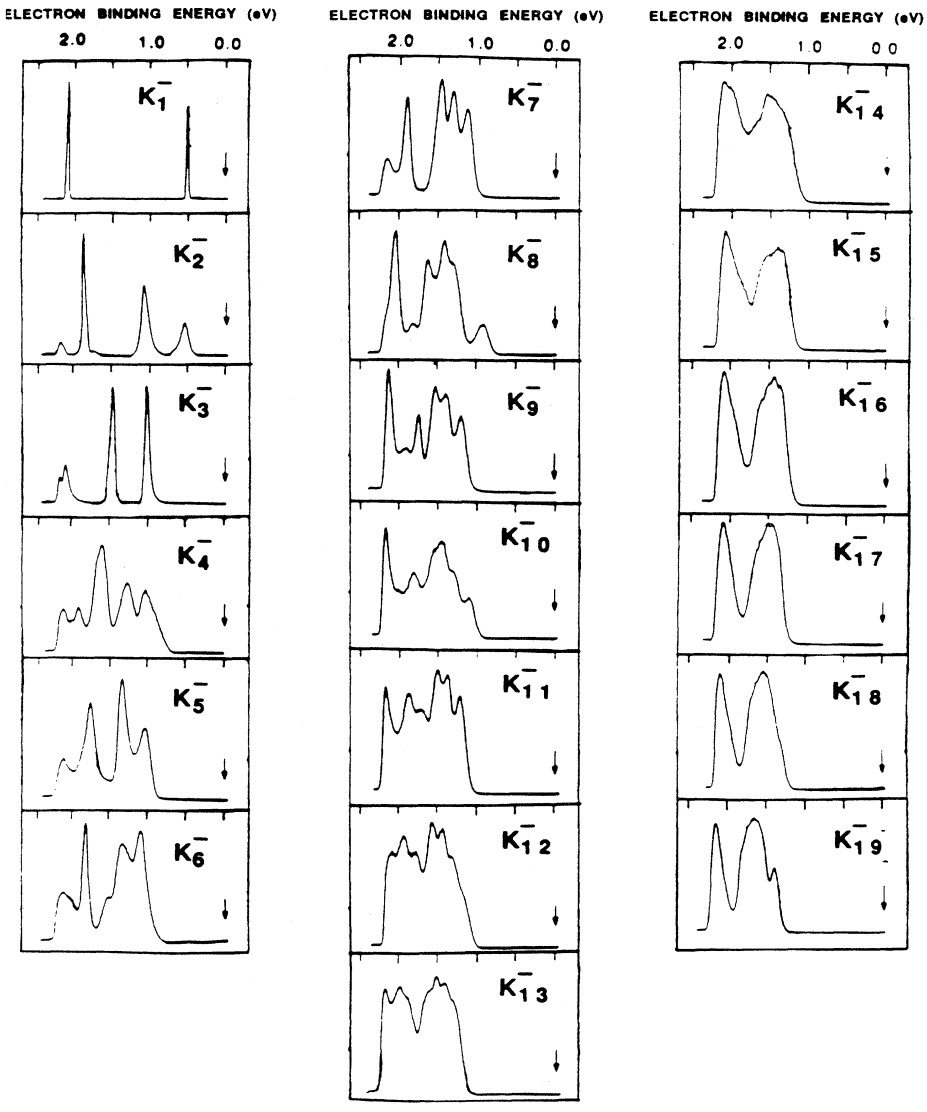

FIG. 32. Photoelectron spectra of potassium cluster anions. After Eaton *et al.*, 1992.

model in Fig. 33(b). The correspondence is very good, suggesting that these spectra in fact primarily reflect the single-particle energies, which in turn are nicely described in the ellipsoidal shell model.

From Fig. 31 it is clear that the spectra of the corresponding small alkali clusters have very much in common, differing primarily in energy scale. Comparing the energy scales of the alkali trimers deduced from the spectra, we find that the $1s$-$1p$ shell splittings are in the proportions 1:0.7:0.6:0.55, for Na_3^-, K_3^-, Rb_3^-, and Cs_3^-, respectively. The bulk Fermi energies of these alkalis in the same order are proportionally 1:0.65:0.57:0.49, in rather close agreement with the scaling in the shell model (see Appendix C).

The linewidths are on the order of 0.1 eV, comparable to the thermal widths of the features in the photoionization efficiency spectra (Secs. VI.B and VI.C). Note that the widths decrease in the order Na, K, Rb, Cs. This corresponds with the scaling arguments in the shell model, where it can be shown that due to vibrational effects (ignoring zero-point motions) the widths should scale as $T^{1/2}E_f^{1/2}$.

Assuming that the clusters are near the evaporation limits (see Sec. III.A.2), then the Na, K, Rb, and Cs trimer peak widths should be in the proportions 1:0.80:0.75:0.7, approximately as observed.

The ideas outlined here are worked out in detail in Appendix C, where an extended model (based on the shell model) which includes vibrations is developed. The agreement with experiment is remarkable.

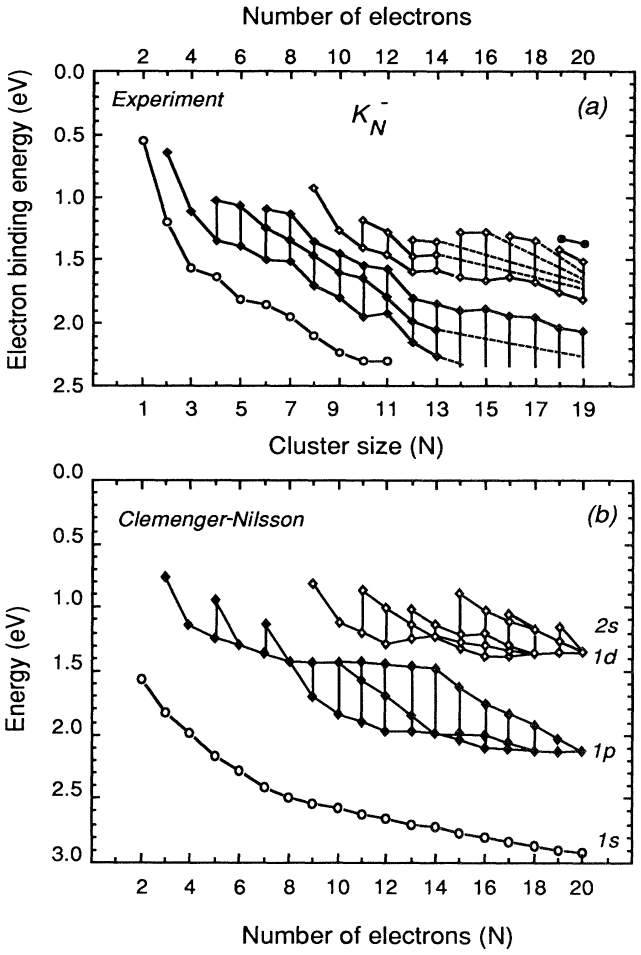

FIG. 33. Systematics of electron binding energies: (a) Experimental photoelectron peaks from Figs. 31 and 32. For $N > 13$ the peaks merge into two bands. Solid lines between clusters follow the measured peaks; vertical lines indicate the bands. (b) Calculated highest occupied orbitals from the ellipsoidal shell (Clemenger-Nilsson) model; note the correspondence to (a) (see also Fig. 5).

2. Photoelectron spectroscopy of copper, silver, and gold clusters

The photoelectron spectra of noble metals have been studied extensively. Although, strictly speaking, the noble metals are not simple, the electronic structure of the conduction band near the Fermi surface resembles that of the simple metals. Photoelectron spectra of copper cluster anions with $N = 6$–21 have been recorded by Pettiette *et al.* (1988) and, for $N = 1$–10, by Leopold *et al.* (1987).

Photoelectron spectra for copper anions up to Cu_{410} have been recorded by Chesnovsky *et al.* (1990). This work has been recently followed with impressively complete work by Taylor *et al.* (1992) reviewing copper (1–411), silver (1–60), and gold (1–233) cluster photoelectron spectra, which are compared with the ellipsoidal shell model.

The copper spectra are reproduced in Fig. 34. The structure of the spectrum for Cu_{410} resembles the bulk photoelectron spectrum. Here one can actually follow the electronic structure effectively from the atom to the bulk. In the copper spectra several interesting features may be discerned. There are clearly two bands, one that grows out of the atomic $4s$ levels and gradually transforms into the conduction band, and a second narrower band that emerges from the atomic $3d$ levels and converges to the bulk $3d$ bands.

The electron affinities (Fig. 35) clearly exhibit shell structure (Pettiette *et al.*, 1988). For example, the electron affinities of 7, 19, and 39 are greater than those of 8, 20, and 40, respectively, as expected from the shell model. Moreover, the predictions of the electron affinities from the ellipsoidal shell model agree qualitatively very well with the experimental results (Fig. 35). Similar agreement is also found for the next-deeper-lying levels (Pettiette *et al.*, 1988). In contrast, shell structure is absent in the $3d$ band (see below, Sec. VII.D), indicating that the $3d$ electrons are localized on the ionic cores, so that the considerations that cause shell structure do not apply.

The electron affinities of silver clusters have been determined by Ganteför *et al.* (Ganteför, Gausa, *et al.*, 1988a, 1988b; Ganteför, Meiwes-Broer, and Lutz, 1988) and, at lower resolution but for a larger size range, by

Taylor *et al.* (1992). As first noted by Ganteför, Gausa, *et al.* (1988a), the electron affinities are strikingly similar to those found for copper (Fig. 35), although silver shows more pronounced odd-even alternations in the electron affinities (see Taylor *et al.*, 1992). For reference, the atomic ionization potentials and the work functions of both these metals are nearly identical, and the Wigner-Seitz radii differ by about 10%. On the other hand, the top of the *d* band of silver is approximately a factor of 2 further below the Fermi level than for copper.

The photoelectron spectra of gold clusters are again qualitatively similar to those of silver and copper, clearly showing ellipsoidal shell effects (Taylor *et al.*, 1992). However, for gold clusters there is a more pronounced odd-even alternation in the electron affinities compared

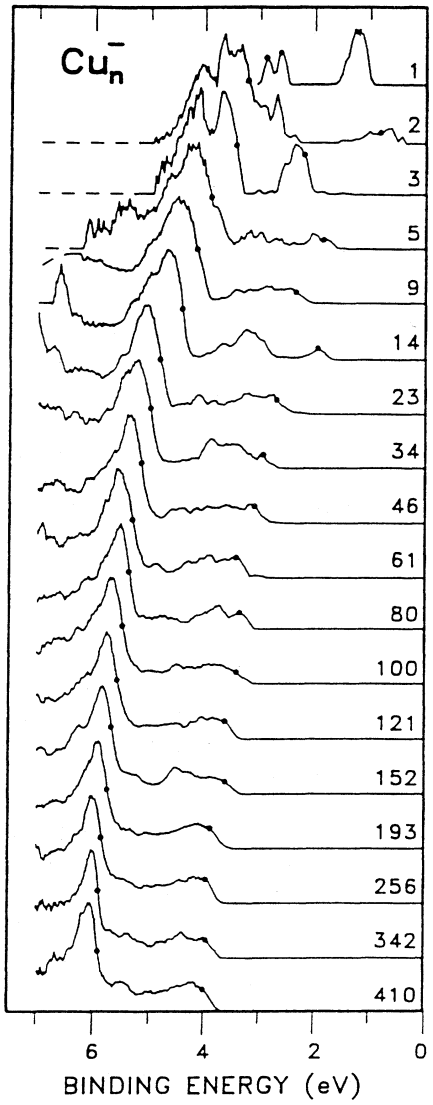

FIG. 34. Photoelectron spectra of copper anionic clusters. Dots indicate the positions of the highest levels corresponding to the two bands. The spectrum of Cu_{410} closely resembles the bulk. After Chesnovsky *et al.*, 1990.

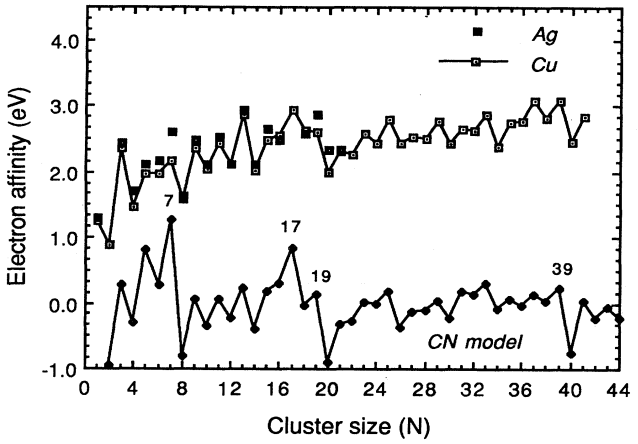

FIG. 35. Experimental electron affinities of copper (Pettiette *et al.*, 1988) and silver (Ganteför *et al.*, 1988) anionic clusters compared with the highest occupied levels from the ellipsoidal shell (Clemenger-Nilsson) model. Note the remarkable similarity in the EAs of these two metals. See also Fig. 17 for related mass spectra.

with copper and silver. As for copper, the states derived from the *d* electrons (in this case the 5*d* electrons) do not show shell structure.

3. Photoelectron spectroscopy of aluminum clusters

The photoelectron spectra of aluminum cluster anions have been recorded by Taylor *et al.* (1988) for $N=3-32$ and by Ganteför *et al.* (Ganteför, Gausa, *et al.*, 1988b; Ganteför, Meiwes-Broer, and Lutz, 1988) for $N=3-14$. The photoelectron spectra of aluminum clusters are interesting in that the hybridization of the 3*s* and 3*p* electrons can be followed. In the atom the 3*s*-3*p* separation is 3.6 eV, and in the bulk the 3*s* and 3*p* bands are hybridized to give the conduction band. Hence the photoelectron spectra of the aluminum atom have two well-separated peaks, while the bulk spectra are nearly featureless.

The change to bulk electronic structure seems to evolve rapidly with increasing cluster size. For clusters with less than about ten atoms, the spectra show a band centered at 3.5 eV binding energy and another at about 6 eV. For larger clusters the band at higher energy seems to merge with the other one, and at about 30 the two form a single structure with only a slightly residual depression at 5 eV (Ganteför, Meiwes-Broer, and Lutz, 1988; Taylor *et al.*, 1988). It is, of course, tempting to relate this observation to the hybridization of the 3*s* and 3*p* bands. In fact, the calculated width of the 3*p* band for Al_{13} of 1.5 eV (Upton, 1986, 1987) corresponds well with the observed width of the 4-eV band, favoring this interpretation.

The electron affinities derived from these spectra have maxima at 6, 13, 19, 27, and 29, which seem to agree

with the electronic shell model, when ellipsoidal distortions are taken into account (Taylor *et al.*, 1988). Nevertheless, this interpretation does not fully agree with the ionization potential observations (see Secs. V.C.2 and VI.D.2 and Schriver *et al.*, 1990).

Although the electronic structure of small aluminum clusters is not as simple as that of the bulk, the reason for the discrepancies is unclear. They could be related to incomplete hybridization, or to ionic core (crystal-field) effects. Further calculations and experiments will be necessary to answer these questions.

4. Photoelectron spectroscopy of mercury clusters

Although mercury is not a simple metal, it is chemically homologous to cadmium and zinc, and both these metals show evidence of electronic shell structure (Sec. IV.A.3). Clusters up to Hg_{70} have been investigated with coincidence photoelectron spectroscopy, in which the neutral clusters are photoionized and both the photoion and the photoelectron are detected (Rademann, 1989, 1991). Hence these experiments give information on the ionization potential and not on the electron affinity. It is observed that the ionization potential decreases with increasing size. For small clusters ($N<17$), the ionization potential approximately follows Eq. (6.1), with α slightly less than 0.5 and an extrapolated work function of about 6.5 eV, i.e., about 2 eV greater than that of bulk Hg. Between 17 and 70 there is a strong departure from Eq. (6.1), and it appears that the ionization potential asymptotes towards Eq. (6.1), with $\alpha\approx 0.5$ and with WF=4.5 eV, which is the bulk work function of mercury.

This behavior is consistent with a metal-nonmetal transition, and it is concluded that this gradual transition occurs between about $N=17$ and 70. For a recent review see Rademann (1991).

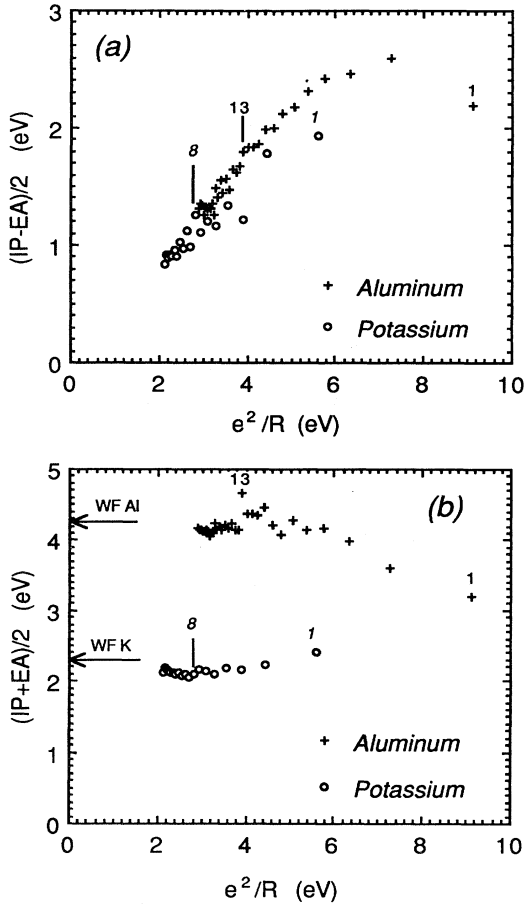

FIG. 36. Analysis of the ionization potential. (a) Half the difference of the IP and the EA for aluminum and potassium clusters as a function of the inverse radii; (b) the average of these quantities. Numbers correspond to N, with italics for K_N and plain roman for Al_N.

D. Comparison with classical and semiclassical models

Both for aluminum and for potassium clusters data are available on the ionization potential as well as on the electron affinities. As in Seidl *et al.* (1991a) and Milani *et al.* (1991), these data are combined in Fig. 36, where $\frac{1}{2}$ (IP-EA) and $\frac{1}{2}$ (IP+EA) are plotted versus e^2/R. From Fig. 36(a) it is clear that, thus plotted, both these metals follow similar trends. According to the chemical model [i.e., $\alpha=\beta=\frac{1}{2}$, Eq. (6.1)], the trend should be given by $0.5e^2/R$, whereas experimentally it is found to be about $0.42e^2/R$. According to Seidl *et al.* (1991b), these values should be $(\alpha_1+\beta_1)/2$ [Eq. (6.2)], which, in fact, turns out to be almost exactly 0.5, as in the classical picture. The experimental curves in Fig. 36(b) are also interesting. Notice that even for very small K clusters $\frac{1}{2}$ (IP+EA) gives very nearly the bulk work function, whereas for aluminum there are clearly two regions. For $N>13$, $\frac{1}{2}$ (IP+EA) is very close to the bulk work function, but for smaller ones there are substantial deviations.

As in Sec. VI.E for the ionization potentials, the experimental electron affinities may be compared with classical and semiclassical models (Fig. 37). The closed-shell clusters of potassium (bulk, 19^-, 7^-, and 1^-) are fitted very well with a parabola, and experimentally it is found that $\beta_1=0.548$, $\beta_2=-1.08$, compared with the theoretical values of $\beta_1=0.633$, $\beta_2=-0.932$ [Eq. (6.2)]. For aluminum the experimental values are $\beta_1=-0.47$, $\beta_2=-0.14$, and the theoretical values are $\beta_1=-0.568$, $\beta_2=-0.734$.

A similar analysis for copper clusters (Fig. 38) shows again that the closed-shell clusters define a parabola very well, giving $\beta_1=0.72$, $\beta_2=0.036$ (Fig. 38); the theoretical values are $\beta_1=0.58$, $\beta_2=-0.02$. Likewise, the top of the $3d$ band also fits a parabola very well (Fig. 38), with the parameters $\beta_1=0.69$, $\beta_2=0.029$. It is very interesting that fitting parameters for the d band are so very close to those of the s electrons. This indicates the primarily electrostatic origin of the curvature term and agrees with Eq. (7.2).

VIII. OPTICAL PROPERTIES

A. Introduction

Over the years optical spectroscopy has been indispensable for elucidating the electronic structure of atoms and molecules. Recently spectroscopic methods have also been developed for metal clusters, and progress is very rapid. In this section the optical properties of simple metal clusters are discussed and compared with the simple models.

In view of the electronic shell structure in simple metal clusters, it might be expected (in analogy with atoms) that the optical spectral features relate to transitions between the single-particle energy levels of the shell model. It turns out, however, that for all but the smallest clusters the spectra are dominated instead by collective resonances, which in many respects resemble the giant resonances observed in nuclei (Bohr and Mottelson, 1975). Single-particle excitations are observed as fine structure near these resonances.

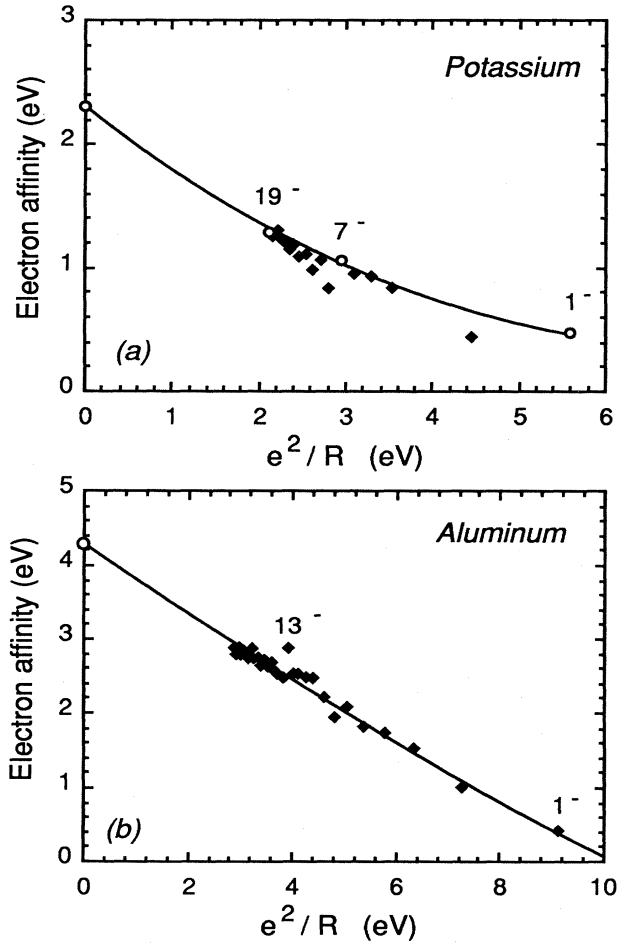

FIG. 37. Electron affinities of (a) K_N and (b) Al_N, plotted against $1/R$. Lines correspond to parabolic fits; the fitting parameters are given in the text.

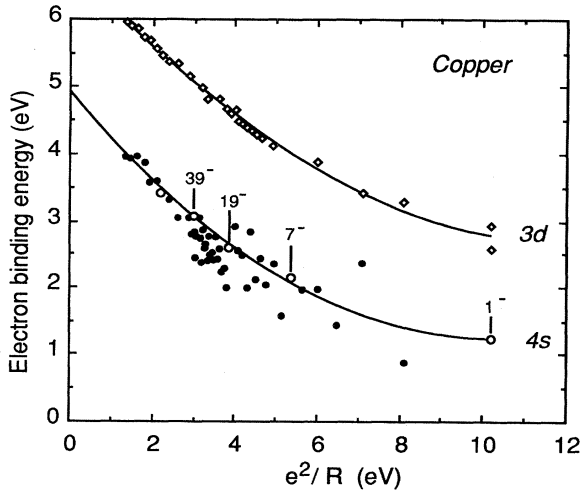

FIG. 38. Electron affinities of Cu_N (i.e., of the $4s$ electrons) and the binding energies of the top of the $3d$ band plotted against $1/R$. The $3s$ electrons show shell structure, whereas the $3d$ electrons do not. Lines correspond to parabolic fits; the fitting parameters are given in the text. The two points for the $3d$ electrons of Cu^- correspond to the $2D^{5/2}$ and $2D^{3/2}$ states.

For the alkali dimers and trimers there is less evidence for the collective resonances, and more complex transitions are found to be responsible for the optical response. This is partly because these clusters have so few electrons that a collective mode is hardly possible; in addition, details of the spectra are actually finely resolved, while for larger particles the spectra are so congested that only the envelopes can be identified.

Special experimental techniques have been developed to investigate the optical properties of clusters in molecular beams; two important ones are described below. The first method uses resonant two-photon ionization. With the first photon an electronic state of the cluster is excited, and the second one further ionizes it. Hence recording the cluster-ion signal strength as a function of the energy of the first photon produces an absorption spectrum of the electronic excited states. This method, of course, requires that the excited state be sufficiently long lived so that the second photon can have the desired effect. At present this has yielded results only for very small clusters (i.e., Li_3 and Na_3).

For larger clusters two-photon ionization spectroscopy has not been successful, until very recently (Sec. VIII.N), because of rapid radiationless decay of the excited states. Although the decay prohibits two-photon ionization spectroscopy, it may be used advantageously as follows. Via internal conversion the electronic energy is dissipated in the cluster, causing heating. If the temperature rise is sufficient to dissociate the cluster, it will be possible to use this disintegration as a signature of the optical excitation, as explained in more detail in Sec. VIII.E.

In the following sections we first discuss two-photon

ionization spectroscopy of the alkali trimers, followed by the spectroscopy of larger clusters.

B. Jahn-Teller effect in alkali trimers

Although the alkali trimers are not representative of simple metal clusters in general, they are of considerable importance in their own right, being quite different from "normal" molecules. This is primarily because the trimers are Jahn-Teller systems with interesting dynamical and optical effects (Jahn and Teller, 1937; Herzberg, 1966; Longuet-Higgins, 1961).

In the discussion of the ellipsoidal shell model (Sec. II.B) it was shown that open-shell clusters spontaneously distort from sphericity, assuming ellipsoidal shapes. This is also a manifestation of the Jahn-Teller effect (Jahn and Teller, 1937).

Alkali trimers are perhaps the simplest examples of Jahn-Teller systems, and the optical spectra have been thoroughly studied (see below). We shall discuss the experimental results after a brief discussion of the Jahn-Teller effect in triatomic systems. A more complete discussion can be found in Herzberg (1966).

To lowest order the Born-Oppenheimer surface of the ground state of an alkali trimer is shown in Fig. 39 (Herzberg, 1966), where the potential energy of the trimer is plotted as a function of its normal coordinates as shown. The central cusp, which corresponds to the electronically degenerate, equilateral configuration, is surrounded by a moat of lower potential, giving the potential surface the appearance of a Mexican hat. (The complete Born-Oppenheimer surface consists of two sheets—a cone-shaped upper sheet and the Mexican-hat lower sheet—representing the two electronic states, which are degenerate at the point of contact at the cusp.) At this level of approximation the bottom of the moat is an equipotential, so that there the potential energy is independent of β. For illustration, Fig. 39 (top) shows the cluster configuration in the moat for an arbitrary β.

One possible excitation of the trimer is represented by the free rotationlike motion of the configuration around the cusp. As far as the cores are concerned, this motion corresponds to a synchronous rotation of the three cores about the equilateral triangle vertices (see Fig. 39) corresponding to an internal rotation, or pseudorotation. The energy levels can be expressed as (Longuet-Higgins *et al.*, 1958; Longuet-Higgins, 1961)

$$E_{\rm pr}=\frac{j^2}{2I}\ ,\qquad j=n+\tfrac{1}{2}\ , \tag{8.1}$$

where I is the effective moment of inertia associated with the motion. Note the resemblance with the energy levels of a rotating particle.

The curious fractional quantization of the pseudorotation j is important and related to the fact that the electronic wave function changes sign upon one full cycle of the ionic cores. For the total wave function to remain single valued, the core wave functions must also change sign—hence the half-odd angular quantum numbers. Recently the geometrical phase associated with taking a quantum system around a closed loop, as in the pseudorotation, has been investigated in general by Berry (1984). For this case, however, it must be stressed that pseudorotation represents only part of the total angular momentum: the cluster as a whole also rotates. Taking this into account, we see that the total angular momentum (apart from spin) must be integral (Longuet-Higgins, 1961). Nevertheless, nontrivial effects related to the phase factor result, and these are, in fact, observed in the optical spectra (Delacrétaz *et al.*, 1986). More recent experiments on Na_3 by Ernst *et al.* (1993) indicate that the effects may be due to the pseudo-Jahn-Teller effect, for which the pseudorotational quantum numbers are integer.

When higher-order effects are considered, the bottom of the moat develops three symmetrically positioned potential wells (not shown in the figure; Herzberg, 1966). If the wells are very deep, then the trimer is usually considered to be statically distorted, since the configuration

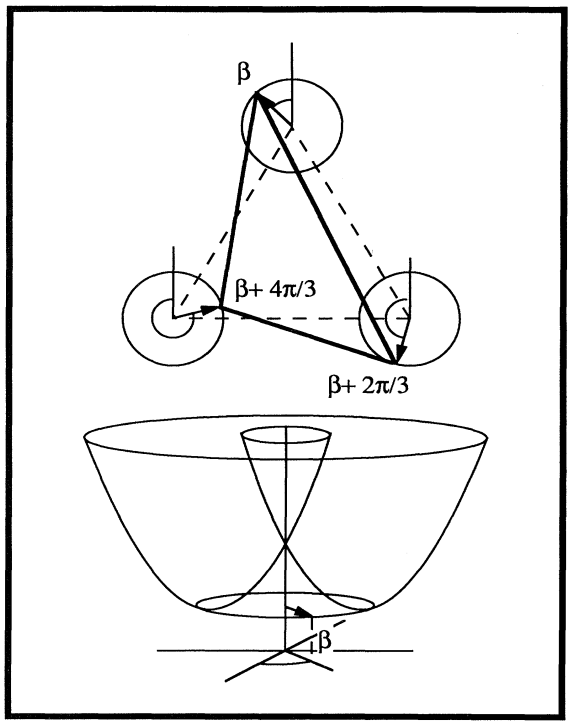

FIG. 39. First-order Born-Oppenheimer surface for alkali trimers, showing the Jahn-Teller effect (lower drawing). Upper drawing shows the trimer configuration in real space, where the circles about the equilateral triangle (dashed line) configuration correspond to the bottom of the "moat" of the Born-Oppenheimer surface. Hence the atoms are free to precess in unison (pseudorotate) about the equilateral configuration. In higher order the Born-Oppenheimer surface develops three symmetrically positioned wells in the moat.

will be localized in one of the three equivalent wells. The pseudorotation is suppressed and replaced instead by vibrations localized within the wells, with small probabilities for tunneling from one well to the next.

Besides the internal rotations, the ionic cores also oscillate radially with respect to the center of mass. This breathing mode is to first order a simple harmonic motion (Longuet-Higgins, 1961):

$$E_b = (n + \tfrac{1}{2})h\omega_b \ . \tag{8.2}$$

From this brief discussion it is clear that large-amplitude anharmonic motion may occur for small excitation energies, or even in the ground state, if the wells are shallow enough.

C. Optical spectroscopy of Na_3 and Li_3

The spectroscopy of lithium and sodium trimers has been performed on clusters from a high-temperature seeded nozzle source using resonant two-photon ionization (for a review, see Broyer, 1989). A quadrupole mass analyzer is used to detect the resulting cluster ions. The trimer ion signal will be proportional to the rate at which the trimers in the intermediate state are produced, and this signal gives a spectrum as shown in Fig. 40 for Na_3 (Broyer *et al.*, 1986).

The Na_3 spectrum consists of several bands: the *A* system around 675 nm, the *B* and *B'* system from 550 to 625 nm, and the *C* system at 475 nm. The *B* system is best understood at present and is a clear example of the dynamic Jahn-Teller effect (Broyer *et al.*, 1986; Delacrétaz *et al.*, 1986).

The Born-Oppenheimer surface of the electronically excited *B* state is found to correspond with the Mexican-hat potential. Note the four vibrational progressions $U(j)$, where the j is the pseudorotation quantum number [see Eq. (8.1)], and U the breathing mode excitation. The energy intervals agree quite well with the approximate expression above. However, the levels labeled with $j = \frac{3}{2}$ are split into two components. The splitting is a second-order effect due to the shallow wells in the moat, as predicted in more detailed theory based on dynamical properties (Longuet-Higgins *et al.*, 1958). An analysis of this band (Broyer *et al.*, 1986) bears out that the Jahn-Teller stabilization energy of this state (i.e., the energy difference from the cusp to the bottom of the moat) is 1050 cm^{-1}. The pseudorotation barrier (i.e., the depth of the wells in the moat) is found to be 26 cm^{-1}. The breathing mode energy is 128 cm^{-1}.

The *B'* system most likely corresponds to the upper (conical) sheet of the Born-Oppenheimer surface (the *B* state being the lower one); however, further analysis is required. Detailed discussions of the other bands can be found in Broyer (1989) and Broyer *et al.* (Broyer, Delacrétaz, Labastie, *et al.*, 1989; Broyer, Delacrétaz, Ni, *et al.*, 1989a, 1989b).

The ground state of the sodium trimer has been investigated through hot-band analysis of the two-photon ionization spectra and more recently in a study using the stimulated-emission-pumping technique (Broyer, Delacrétaz, Labastie, *et al.*, 1989; Broyer, Delacrétaz, Ni, *et al.*, 1989a). For the ground state the pseudorotation is strongly suppressed and more localized vibrations are observed.

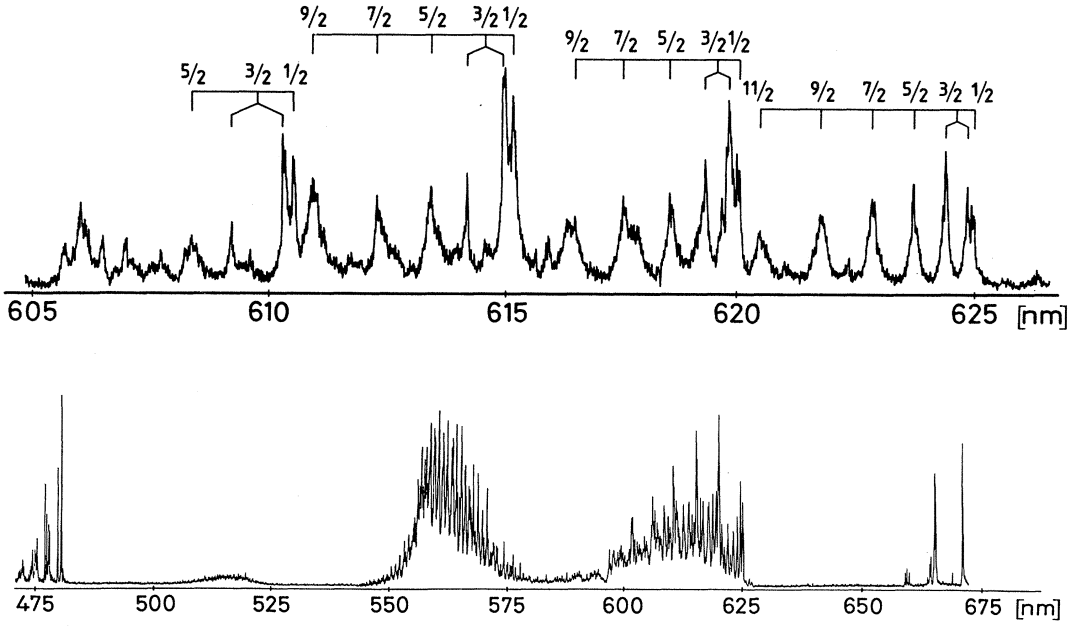

FIG. 40. Resonant two-photon ionization spectrum of Na_3 (bottom), and expanded spectrum in 600–625-nm region with pseudorotation-state labels j (top). After Delacrétaz *et al.* (1986).

Very recently, lithium trimer spectra have been reported (Blanc *et al.*, 1991; Dugourd *et al.*, 1991). For Li_3 the basic physical picture is similar to that for Na_3. Among other things, it is found that for the ground state the pseudorotation barriers are 26 cm^{-1} and the stabilization energy 268 cm^{-1}, so that even in the ground state the Born-Oppenheimer surface for this cluster is very flat, giving rise to pseudorotating states. These results agree reasonably well with calculations by Gerber and Schumacher (1978).

High-resolution spectroscopy of alkali trimers remains a very active field of research, which will certainly have important consequences for understanding larger clusters. Although the vibronic structure of large alkali clusters has not been studied in detail, many are expected to be dynamic Jahn-Teller systems. As pointed out above, the ellipsoidal distortions discussed in Sec. II.B are, in fact, Jahn-Teller distortions, and recent calculations indicate that the Born-Oppenheimer surfaces are very flat, so that dynamic Jahn-Teller effects are expected to be important.

D. Surface plasma resonances in metal clusters: basic model

Studies by Mie (1908) on the classical electromagnetic response of small metal and dielectric spheres explained the colors of stained glasses and colloidal metal solutions. Mie was mainly interested in the response properties (dynamic polarizabilities) of spherical and ellipsoidal particles, and he derived expressions for these in terms of the ratio of the wavelength of light to the particle diameter. As expected, the properties are complex when this ratio is of the order of unity, i.e., for particles with about 10^9 atoms. These sizes are many orders of magnitude larger than what we are concerned with here.

As shown below, Mie resonances are also very important for very small clusters. Often more than half the oscillator strength of the valence electrons are concentrated in a few peaks (de Heer, Selby, *et al.*, 1987; Selby *et al.*, 1989, 1991). Before presenting the experimental data, we briefly described the basic model for these resonances. In fact, for these particles it is simpler than for larger ones, since only the lowest-order term in Mie's expansion is important (Kreibig and Zacharias, 1970).

Following de Heer, Selby, *et al.* (1987), we use the Drude model (Ashcroft and Mermin, 1975) as a starting point for the dynamic polarizabilities of very small metal spheres. Applying a uniform electric field induces a dipole, which in this approximation is described as a small uniform displacement of the electronic cloud to cancel the internal electric fields. In the static limit this displacement is $d=\alpha E$, where α is the polarizability (Sec. IV). The model is easily extended for oscillating fields and, among other things, predicts a resonance at ω_M:

$$\omega_M^2=\frac{Q^2}{M_N\alpha}\equiv\frac{Ne^2}{M_1R^3}\ , \tag{8.3}$$

where Q and M_N are the total charge and mass of the valence electrons, M_1 the atomic mass, R the cluster radius (see below), and α is assumed to be independent of the frequency. The right-hand expression is valid for monovalent metals. For brevity this collective excitation will be called the surface plasmon, conforming with current usage.

Equation (8.3) is rather crude, since it ignores both the effective-mass corrections (Inagaki *et al.*, 1976) and the response of the core electrons (Kittel, 1976). These usually give important shifts (especially for the noble metals) and are often included by introducing an effective dielectric constant for the medium (Kreibig and Genzel, 1985). It turns out that, for sodium, these corrections are small; however, this is not the case for lithium or potassium (see, for example, Kittel, p. 292, Table 2) and most certainly not for the noble metals (Kreibig *et al.*, 1970, 1985).

If the electronic motion is resistively damped in one way or another, then the surface plasmon energy is dissipated in the cluster, leading to a broadening of the resonance. Assuming that the collective mode accounts for all the dipole oscillator strength of the cluster (in fact, this is already implicit in the derivation of ω above), we can give the photoabsorption cross section by

$$\sigma=\frac{4\pi Ne^2}{3m_ec}\frac{\omega^2\Gamma}{(\omega^2-\omega_M^2)^2+(\omega\Gamma)^2}\ , \tag{8.4}$$

where N is the number of electrons and m_e the electron mass.

This is the Mie expression in the small-sphere limit if one uses the classical value for the static polarizability, $\alpha=R^3$, and a damping factor Γ. This result can be refined by using a more accurate value for the polarizability, for example, from quantum calculations or, better still, from experiment. In either case the polarizability is increased [approximately $\alpha=(R+\delta)^3$, Sec. V.B] so that the resonance frequency is reduced. The expression above predicts a single strong absorption peak corresponding with a collective dipole oscillation of the valence electrons. For small clusters it is redshifted compared with the Mie value. Closely related theoretical results were obtained by Bertsch and Ekardt (1985).

Nonspherical clusters need further consideration. Since open-shell clusters tend to be approximately ellipsoidal in shape (Sec. II.B.1), the polarizability has three unequal components along the three principle axes. Accordingly, there are generally three resonances at frequencies given by Eq. (8.3) by replacing α with the polarizabilities along the axes. To first order the frequency ratios between the three components of the polarizability tensor can be found from the axial ratios and the classical expression for the depolarization factors of an ellipsoid (see, for example, Stoner, 1945). The axial ratios can, in turn, be estimated on the basis of the ellipsoidal shell model (see Sec. II.B). Since for sodium the average polarizabilities have been measured, definite predictions of the positions of the surface plasma resonances can be made

(see below and Selby *et al.*, 1989). Results from this model correspond to those from the self-consistent spheroidal LDA model of Ekardt and Penzar (1988, 1991), as well as to the ellipsoidal random-phase-approximation (RPA) calculations of Lauritsch *et al.* (1991) and Bernath *et al.* (1991).

This simplified picture ignores many important aspects of the electronic response. Even in the bulk limit important deviations are observed. For example, Kittel (1976, p. 292, Table 2) shows calculated and observed values for the volume plasmons of alkalis (to obtain the surface plasma frequencies, these values should be divided by $\sqrt{3}$). The Drude value for the volume plasmon is ω_p, and the value corrected for dielectric effects (Raether, 1965) is $\omega_p^* = \omega_p / \sqrt{\varepsilon_\infty}$. Comparing these values, note that the core polarizability effects are most important for potassium and least important for lithium. For lithium, however, there are important shifts in the volume plasmon frequency not due to core polarizabilities. This arises because lithium is not a good free-electron metal: effective-mass shifts (caused by strong interactions with core potentials) are important.

Furthermore, the plasma pole approximation used above predicts one, two, or at most three absorption peaks. Together these exhaust the dipole sum rule; hence there cannot be any other dipole transitions (Jackson, 1975). More realistic treatments predict a more complex response (see, for example, Ekardt, 1985), but for alkali clusters the basic model turns out to be a good first approximation. For an up-to-date review, see Kresin (1992).

E. Longitudinal beam depletion spectroscopy of neutral alkali clusters

As mentioned above, the electronically excited states of alkali clusters with more than three atoms are found to decay so fast by coupling to other degrees of freedom that two-photon ionization experiments have been unsuccessful until very recently (Gerber *et al.*, 1993). The electronic energy is converted into heat, and for small alkali clusters the temperature rise after absorbing an optical photon is sufficient to cause the cluster to evaporate an atom. For example, a 2-eV photon will cause the temperature of a 10-atom cluster to rise by about 650 K, which is more than enough to cause an atom to evaporate from the cluster within a relatively short time (Klots, 1985).

Longitudinal beam depletion spectroscopy (de Heer, Selby, *et al.*, 1987; Selby *et al.*, 1989, 1991) relies on this dissociation of a cluster after the cluster's absorption of a photon. Momentum and energy considerations of the fragmentation process show that the two fragments can be very efficiently removed from the cluster beam provided the beam is tightly collimated. The fractional depletion of clusters from the beam caused by intercepting light is measured, and photoabsorption cross sections can be determined.

The typical experimental configuration for cluster-beam depletion measurements is shown in Fig. 41. A cluster beam is produced in a continuous cluster source and collimated. A counterpropagating pulsed-laser beam envelops the collimated cluster beam. The intensity of a preselected cluster size is continually monitored. Immediately after the laser pulse, the cluster intensity decreases due to the depletion process, recovering again after a time approximately equal to the distance between the source and the detector divided by the cluster speed. An example of a cluster mass spectrum thus depleted is shown in Fig. 42.

A beam depletion measurement is made by measuring the ratio r of the intensities of the clusters in the irradiated cluster beam to those of the unirradiated cluster beam (Fig. 42). If the light flux from the pulsed laser is ϕ photons per unit area per pulse, then the absolute photoabsorption cross section σ is determined from (de Heer, Selby, *et al.*, 1987)

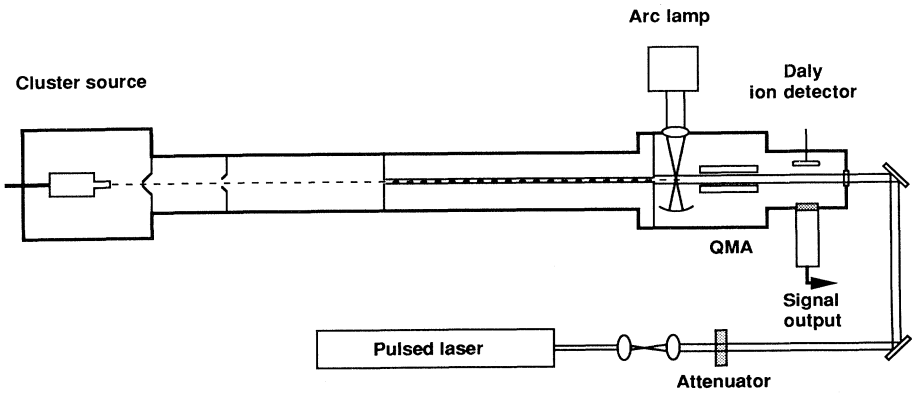

FIG. 41. Apparatus for longitudinal beam depletion experiments. The collimated cluster beam is longitudinally irradiated with light from a pulsed laser, causing photofragmentation. The cluster depletion is measured as a function of wavelength and intensity of the light from which the absolute photoabsorption cross sections are derived.

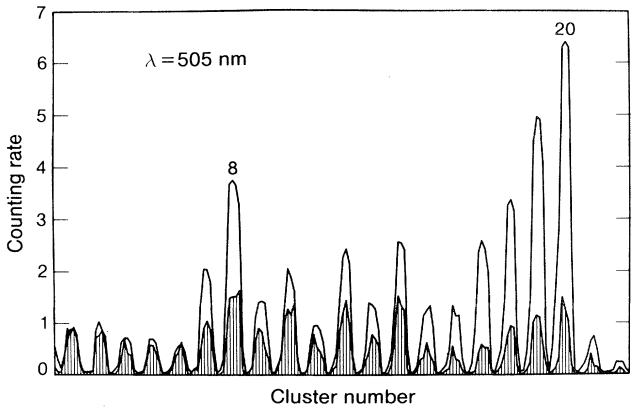

FIG. 42. Example of a depletion spectrum for sodium clusters. Laser heating causes evaporation and depletion (shaded spectrum). After de Heer, Selby, *et al.* (1987).

$$r = e^{-\phi\sigma} . \tag{8.5}$$

In the experiment the photoinduced depletion is measured as a function of the wavelength of the light and as a function of cluster size.

F. Photoabsorption spectra of neutral sodium clusters compared with the basic model

Absolute photoabsorption cross sections for selected sodium clusters with up to 40 atoms are shown in Fig. 43 (de Heer, Selby, *et al.*, 1987; Selby *et al.*, 1989, 1991). Superimposed on the experimental data are the calculated photoabsorption spectra from Eq. (8.4), using the shapes from the three-dimensional oscillator model (de Heer, Selby *et al.*, 1987; Selby *et al.*, 1989, 1991; for a discussion, see Appendix B). The bare mass of the electron and a damping factor of about 0.1 are used. The calculated curves are normalized to 70% of the total oscillator strength.

It is clear that, as far as the position of peaks and the absolute cross sections (adjusted for the 70% reduction) are concerned, the basic model does remarkably well even for clusters with as few as four atoms. The multiple-peaked structures related to the cluster shapes are in overall agreement with those calculated from the shell model (Sec. II.B.1). Note, in particular, the single-peaked structure for Na_8, which agrees with its spherical shape (or, more accurately, its isotropic polarizability tensor); the double peaks of 9 and 10 indicate spheroids, and the (barely resolved) triple peaks of 12 result from its triaxial ellipsoidal shape (Appendix B).

There are, however, several discrepancies with the model. For example, the peak separation of 9 is as large as that for 10, whereas the model predicts that for 10 it should have been twice as large. Furthermore, the closed-shell clusters 20 and 40 have more structure than the model predicts. This effect is discussed below.

Recently measurements on Na_4 and Na_8, by Wang *et al.* (1990), and on Na_{20} by Pollak *et al.* (1991; Fig. 44) have repeated the measurements by Selby *et al.*, using the same experimental method and a similar apparatus. The experimental results agree with those found earlier. These measurements are important, since they were performed over a broader frequency range and with higher resolution than the earlier measurements, thereby bringing out some fine-structure features.

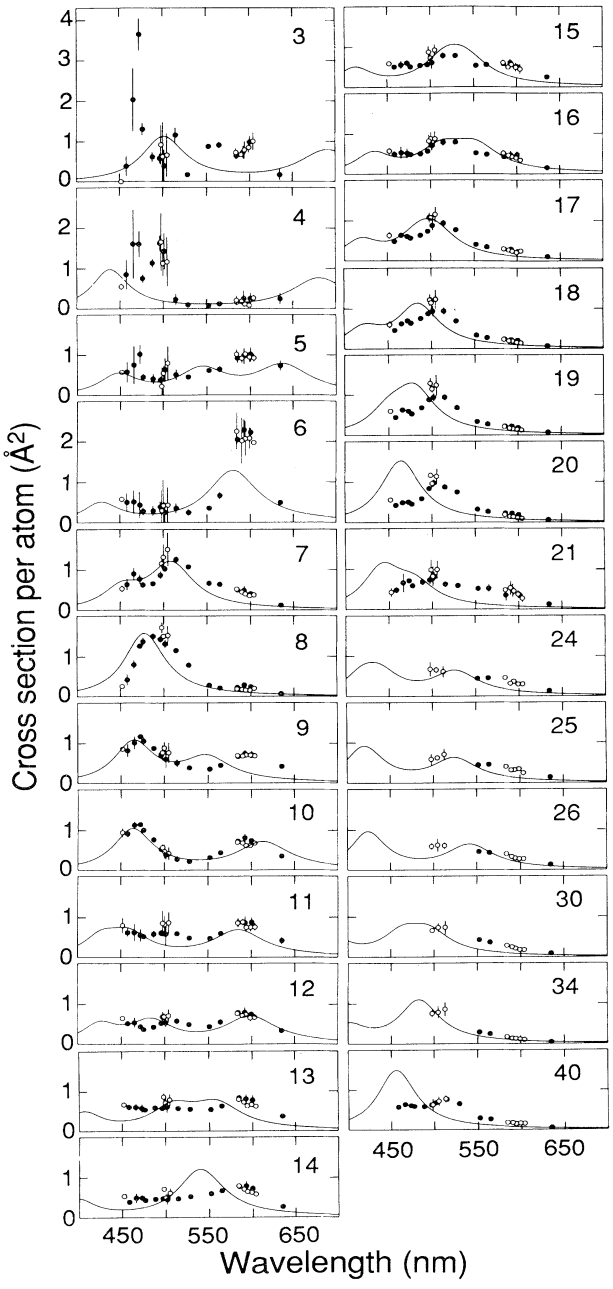

FIG. 43. Photoabsorption cross sections of sodium clusters (after Selby *et al.*, 1991). Continuous curves are calculated using the basic model.

G. Fragmentation and shifts of the surface plasma resonances

Before continuing with other simple metal clusters, we briefly discuss some of the structure in the sodium absorption spectra. The spectra for the closed-shell sodium clusters are shown in Fig. 44. Several have double-peaked or more complex resonance structures, in contrast with the basic model, which predicts single peaks in these cases. This effect, called the fragmentation of the surface plasma resonance, is ascribed to a coupling of the resonance with nearby particle-hole excitations and hence is physically related to Landau damping (see Pines, 1964).

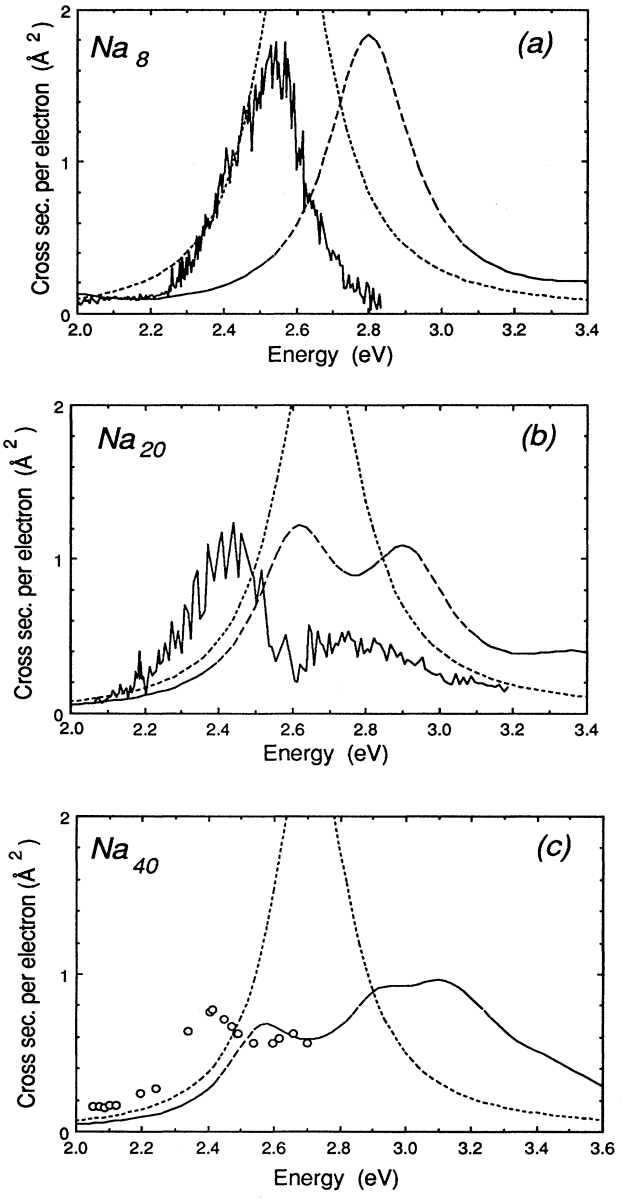

FIG. 44. Photoabsorption cross sections of three closed-shell sodium clusters: (a) Na_8 (Wang *et al.*, 1990); (b) Na_{20} (Pollack *et al.*, 1991); (c) Na_{40} (Selby *et al.*, 1991, open circles). Dotted lines are calculated in the basic model; dashed lines are from RPA jellium calculations by Yannouleas and Broglia (1991a).

For small clusters, couplings with single-particle excitations cause the surface-plasmon oscillator strength to be distributed (or fragmented) among several coupled plasmon–particle-hole excitations. An elementary discussion of the coupled states is given in Appendix B.3 (see also Fallgren and Martin, 1990). The fragmentation phenomenon has recently been carefully investigated within the spherical jellium model by Yannouleas *et al.* (1989, 1990; Yannouleas and Broglia, 1991). It was already apparent in earlier theoretical investigations of the dynamic polarizabilities of jellium spheres in the LDA by Ekardt (1985).

When one compares the spectra of closed-shell sodium clusters (Fig. 44), it appears that the basic model is more accurate for the smaller clusters. This effect has been explained by Yannouleas *et al.* (1989; Yannouleas and Broglia, 1992). Of course, the degree of fragmentation depends on whether there are in fact single-particle transitions nearby to which the surface plasmon can couple, and if there are, whether they have the correct symmetry. It is clear that the density of single-particle excitations increases with the number of valence electrons, though only a subset of these couple to the surface plasmon, as shown by Yannouleas and Broglia (1992).

The jellium calculations (in the RPA) by Yannouleas *et al.* (1989) for Na_8 and Na_{20}, and by Yannouleas and Broglia (1991) for Na_{40}, correspond well with experiments as far as the fragmentation of the resonance is concerned. On the other hand, this result is surprising from a molecular point of view, since ionic core effects might be thought to be most important for the small clusters. However, experimentally they seem to be inconsequential.

For the larger clusters it is clear that the positions of the resonances are redshifted compared with the basic model. Core polarizability effects are a possible cause of a redshift. These are discussed below in Sec. VII.J. Furthermore, for larger clusters it appears that there is progressively less oscillator strength, which is probably due to more important fragmentation of the plasmon, perhaps into volume plasmons at higher energies. These have been predicted by Brack (1989), Reinhard *et al.*, (1990), and Kresin (1989c). However, theoretical evidence is already apparent in earlier work by Ekardt (1985). For a review, see Sec. IV of Brack (1993).

H. Cesium clusters

The surface plasmons of Cs_8 [Fig. 45(b)] and $Cs_{10}O$ have recently been measured with depletion spectroscopy on (initially) cold (about 100 K) clusters by Fallgren and Martin (1990). Note that for $Cs_{10}O$ the oxygen will bind two electrons from the Fermi sea, so that $Cs_{10}O$ is an 8-electron closed-shell cluster.

As for sodium and potassium, these closed-shell clus-

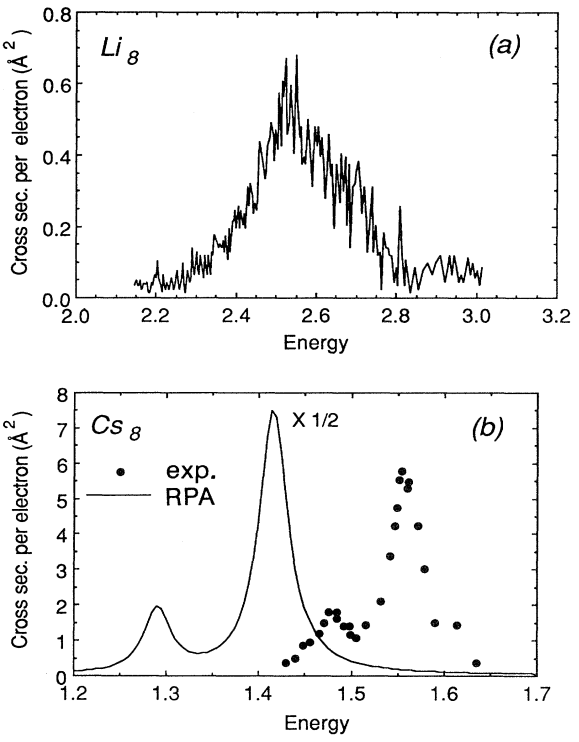

FIG. 45. Photoabsorption cross sections of alkali clusters: (a) Li_8 (Blanc *et al.*, 1991); (b) Cs_8 (Fallgren and Martin, 1990). Solid line in (b) is calculated in RPA jellium by Yannouleas and Broglia (1991b).

ters have essentially one strong resonance, but in these cases, owing to the narrower peak widths at the lower temperature, fragmentation of the resonance is clearly visible as opposed to the other alkali clusters with the same number of electrons [Figs. 44(a) and 45(a)].

I. Optical spectra of lithium clusters: effective-mass corrections

Lithium clusters up to Li_8 (excluding five) have been measured with the beam depletion method by Dugourd *et al.* (1991) and Blanc *et al.* (1991). The spectrum of Li_4 is very similar to that of Na_4 studied by Wang *et al.* (1990), both in structure and in the positions of the peaks. Likewise, the spectrum of Li_8 is dominated by an intense peak at 490 nm and is quite similar to that of Na_8 [Fig. 45(a)]. Correspondences between Na_N and Li_N are also clear for $N=3$, 6, and 7.

Ab initio quantum-chemical calculations (Bonacic-Koutecky *et al.*, 1991) correspond well with the observed features (Blanc *et al.*, 1991). However, the basic model using the calculated static polarizabilities (Puska *et al.*, 1985) gives surface plasma resonances that are too blue by about 20%. This discrepancy is far too large to be explained by inaccuracies in the calculated polarizabilities, nor can it be explained in terms of core polarizabilities. Note, for example, that for bulk lithium the core polarizability correction is very small (see Kittel, p. 292, Table 2). However, note also that there is a significant difference between the Drude value and the measured values of the bulk plasmon.

In the bulk these are partly due to effective-mass effects that hence appear to be important for small clusters as well (Dugourd, 1991). As noted earlier, the optical electronic mass for bulk lithium is $m^*=1.56m$ (Inagaki *et al.*, 1976). If this large optical mass is applied to the small clusters, then the correspondence with experiment is good. This causes the related shift of the volume plasmon in the bulk (Inagaki *et al.*, 1976). Hence it may be tentatively concluded that the mass corrections due to the ionic core potentials have approximately the same effect in the optical properties of small lithium clusters as in the bulk. Effective-mass corrections have recently been treated theoretically by Bernath *et al.* (1993).

J. Closed-shell potassium cluster ions: core effects

Depletion spectroscopy has also been performed by Bréchignac *et al.* (1989a) on potassium cluster ions using two time-of-flight mass spectrometers in tandem. Cluster ions are selected with the first mass spectrometer. The clusters are irradiated with a laser, causing photofragmentation. The beam is then analyzed with the second mass spectrometer. A mass spectrum of photofragmented potassium clusters contains information not only on the fragmentation cross sections but on the fragmentation branching ratios as well. Here we concentrate on the photoabsorption cross sections, and the cluster fragmentation process is discussed in Sec. IX.

The resonances for the closed-shell clusters K_9^+ (with 8 electrons) and K_{21}^+ (with 20 electrons; Fig. 46) are remarkably well defined with a single Lorenzian. According to the basic model, the single peaks result from the spherical polarizability tensor, confirming that, for cluster ions as well, the shape is determined by the number of valence electrons.

Comparing these spectra with the corresponding neutral sodium spectra, we see that here fragmentation of the surface plasmon is not an important effect. This has been recently explained by Yannouleas *et al.* (1990; Yannouleas, 1992), who find that for the cluster ions the single-particle resonances are shifted away from the surface plasma resonances, so that fragmentation effects are strongly reduced. Nevertheless, recent experiments by Bréchignac, Cahuzac, Carlier, *et al.* (1992) also show that Na_{21}^+ has a very sharp hole in the resonance, indicating a very weak transition that is nearly coincident with the surface plasmon (an explanation of this effect is suggested in Appendix B.3).

More recently, Bréchignac, Cahuzac, de Frutos, Kabaili, *et al.* (1992) investigated the plasmons of K_{600}^+ and K_{900}^+. Since now many photons are involved, the absorption cross section is determined not from the depletion but from the size distributions of the photofragments.

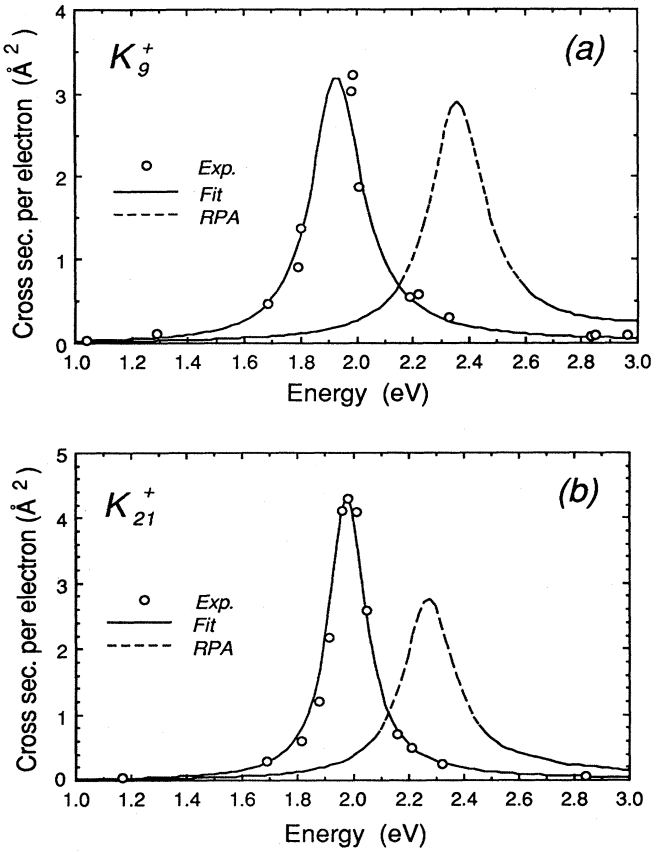

FIG. 46. Photoabsorption cross sections of two closed-shell potassium cluster ions: (a) K_9^+, (b) K_{21}^+ (after Bréchignac, Cahuzac, Carlier, and Leygnier, 1989a). Solid lines are fits to the experimental data; dashed lines are from RPA jellium calculations by Yannouleas *et al.* (1990). We have not shifted the theoretical data as done in the presentation by Yannouleas *et al.* (1990). The reader should refer to the original figure and discussion.

Results of these studies are displayed in Fig. 47, which shows the plasmon peak positions as a function of size. The larger clusters are far from the theoretically predicted positions found from an RPA calculation on jellium spheres (using a program by Bertsch, 1990). Note, however, that the extrapolated bulk value [i.e., $\omega_{\rm pl}(\text{expt})/\sqrt{3}$, where $\omega_{\rm pl}(\text{expt})$ is the measured bulk volume plasma frequency] is also shifted compared with the Drude value, by a comparable amount. The origin of this shift can be traced to the dielectric response of the ionic cores (Kittel, 1976, p. 292, Table 2; Raether, 1965), which has been ignored in the calculations. Shifting the theoretical data proportionally to account for the effect gives good correspondence with experiment.

The resonance of K_{21}^+ has also been measured by Dam and Saunders (1991) on clusters produced with a sputtering source. They find a resonance that is slightly redshifted and significantly broadened compared with those reported by Bréchignac, Cahuzac, Carlier, and Leygnier,

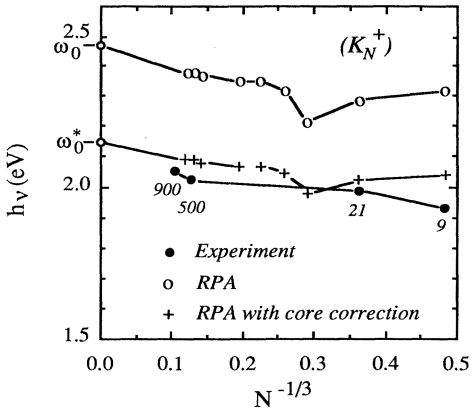

FIG. 47. Measured and calculated plasma resonances of potassium cluster ions. Measurements (solid circles) and RPA jellium calculations (open circles) are after Bréchignac, Cahuzac, Kabaili, Leygnier, Roux, and Sarfati (1992a, 1992b). Core polarizability corrected RPA calculations (crosses) are described in text. Bulk values are shown at $N^{-1/3}=0$.

(1989a), which could be due to higher temperatures of the clusters from the sputtering source.

K. Noble-metal clusters: influence of the *d* electrons

The optical properties of the noble-metal clusters have been studied for over a century, but only recently in molecular beams. The optical properties of embedded clusters have been reviewed by Kreibig and Zacharias (1970) and by Kreibig and Genzel (1985). Surface plasma resonances account for the optical properties of larger noble-metal clusters; however, Eq. (8.3) predicts resonances that are too blue.

For the larger noble-metal particles, Eq. (8.3) needs to be modified to account for the dispersion caused by interband transitions of the *d* electrons (Kreibig and Genzel, 1985). Since the interband transitions for copper and gold are in the visible spectrum (in fact, these transitions give the bulk noble metals their colors) and for silver are in the low UV, strong couplings with the surface plasmons are expected and are primarily responsible for large frequency shifts for larger particles. For example, for silver the basic model above predicts a surface-plasmon energy of 5.18 eV compared with the measured large-particle value of about 3 eV. Note that for silver the optical mass is close to that of the free electron (Ehrenreich and Philipp, 1962), so that mass corrections are not important in contrast with Li clusters.

Recently Tiggesbäumker *et al.* (1992) measured the surface plasmons of small silver clusters by depletion spectroscopy on hot cluster ions produced in a sputter source. For Ag_9^+ and Ag_{21}^+, single peaks were observed at about 4 and 3.8 eV, respectively [Fig. 48(c)], i.e., blue shifted compared with the large-particle value of 3.5 eV. In contrast, however, with the basic model, it was found that the surface plasma resonance should have an energy

of 4.08 eV for Ag_{21}^+ (using $r_s=3.02$ and $\delta=1.4$ a.u. for the electron spillout; see Sec. V.B). Hence the experimental value is only slightly redshifted compared with the basic model value.

The same group also measured photoabsorption spectra of silver anion clusters (Köller *et al.*, 1992; Tiggesbäumker *et al.*, 1992). Single peaks were observed for the closed-shell clusters Ag_7^- and Ag_{19}^-, while multiple peaks were observed for Ag_9^-, Ag_{13}^-, and Ag_{15}^-, in qualitative agreement with the shell model.

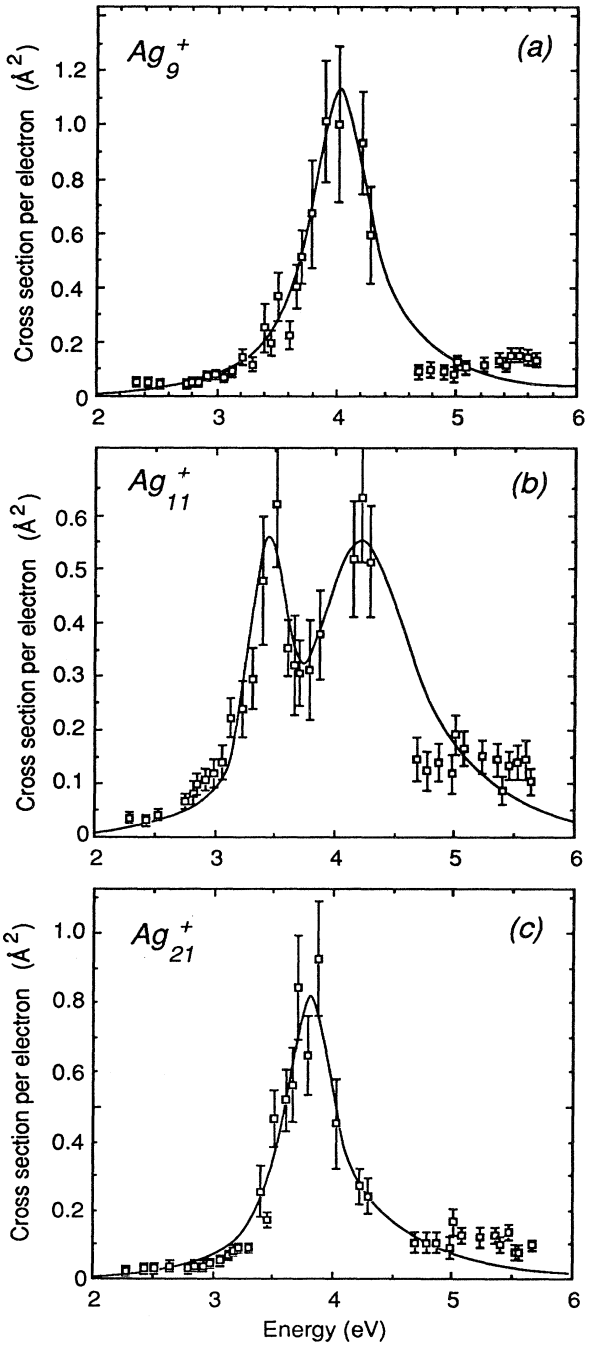

FIG. 48. Photoabsorption cross sections of silver cluster ions: (a) and (c) are closed-shell clusters and have single peaks; (b) the open-shell Ag_{11}^+ has two peaks, as predicted in the ellipsoidal shell (Clemenger-Nilsson) model. Solid lines are fits to the data. After Tiggesbäumker *et al.*, 1992.

Figure 48(b) shows the surface plasmon of Ag_{11}^+, which has two distinct peaks, the higher-energy peak being about twice as intense as the lower-energy one. This agrees with the prolate spheroidal shape of this 10-electron cluster (see Sec. II and Fig. 43). From the ellipsoidal shell model the ratio of the peak separation and the average position is 0.27, compared with the measured value of 0.21. Recently Bréchignac, Cahuzac, Carlier, de Frutos, and Leygnier (1992) also found a double peak for K_{11}^+ which is very similar to that for Ag_{11}^+. The ratio of measured separation to average position is 0.24, remarkably close to the shell-model value.

Finally, optical measurements of mass-selected silver clusters ($N<15$) deposited in a frozen argon matrix have been made by Harbich *et al.* (1992), who observed sharp surface-plasmon peaks. The position of the peaks and the splittings are in qualitative agreement with the basic model given here and with the molecular-beam measurements of Tiggesbäumker *et al.* (1992).

From these observations we can speculate that the interband transitions do not affect the surface plasma frequencies of very small silver clusters as much as they do larger ones. The reduced effect of the *d* electrons is interesting and deserves further investigation. Perhaps for small clusters the transitions from the *d* levels to the Fermi surface are suppressed or shifted. This would reduce the dispersion of the surface plasmon compared with large particles and the bulk.

L. Line shapes of the surface plasma resonances

In the basic model the lifetimes and widths of the resonances are included with an empirical damping factor Γ Theoretically the linewidths are expected to be determined primarily by inhomogeneous broadening effects due to the Franck-Condon factors associated with shape changes upon absorption of a photon. In the ellipsoidal shell model this effect is readily understood by observing that the total energy of the excited state involves the energy of the surface plasmon, which in turn is very sensitive to the shape of the cluster, as discussed earlier. For example, the energy of a cluster excited by a plasmon is approximately related to the ground-state energy $E_0(x)$ by (see Appendix B.2)

$$E(x)=E_0(x)+\tfrac{3}{5}\hbar\omega_M\frac{(x_0-x)}{x_0}\ , \tag{8.6}$$

where x is an axis of the cluster, x_0 is the ground-state equilibrium shape, and $\hbar\omega_0$ is the surface-plasmon energy of the undistorted shape. For $E_0(x)$ the total energy from the shell model can be used. It is clear that the surface plasmon tends to elongate the cluster. Using argu-

ments completely analogous to the discussion of the thermal widths in the photoionization efficiency spectra (Secs. VI.B and VI.C), we can quickly predict from this model a width for the surface plasmon.

This analysis is carried out further in Appendix B.2, giving very reasonable surface-plasmon widths and line shapes (see also Fallgren and Martin, 1990). It is further found that fragmentation of the surface plasmons may also give rise to sharp holelike features (rather than peaks) in the photoabsorption spectra (Appendix B.3).

Other treatments along similar lines also predict widths that compare favorably with experiment. For example, a semiclassical treatment of Bertsch and Tománek (1989) and a calculation by Pacheco and Broglia (1989) yield thermal widths close to those observed experimentally. Ekardt, Penzar, and Rubio (1990) find that the zero-point quadrupole motions give an important contribution. Pacheco, Broglia, and Mottelson (1991) more carefully treat the quantal shape fluctuations, giving low-temperature predictions.

For small clusters the fragmentation of the resonances causes fine structure rather than a broadening. For large clusters, on the other hand, the fragmentation of the resonance will become increasingly important, ultimately resulting in a quasicontinuum of coupled plasmon/single-particle states (Yannouleas and Broglia, 1992). In this limit (corresponding to Landau damping in the bulk), the cluster-radius-dependent part of surface-plasmon lifetime is predicted to be (see, for example, Kawabata and Kubo, 1966; Wood and Ashcroft, 1982; Kreibig and Genzel, 1985)

$$\tau = a\frac{R}{v_F} , \tag{8.7}$$

where v_F is the Fermi velocity and a is a constant of order unity. Corresponding resonance widths with this characteristic radius dependence are observed for larger supported noble-metal clusters, but matrix support effects have been found to contribute as well (Kreibig and Genzel, 1985).

Note that none of the line-broadening mechanisms described above involve the complete thermalization of the electronic motion into all the electronic and vibrational degrees of freedom of the cluster, and, in fact, this aspect has not yet been studied in detail. It is generally believed that the time scales for this nonradiative decay are too long to affect the experimental widths. Nevertheless, since the clusters dissociate rather than radiate, it is certain that the nonradiative decay must occur within the radiative lifetime of the electronic excited state. To what extent lifetime effects contribute to the linewidths remains to be investigated. Perhaps two-photon ionization spectroscopy using laser pulses short enough that the decay of the surface plasmons can be followed in time will shed some light on this very intriguing question (see, for example, Beswick and Jortner, 1990).

M. Plasmons versus molecular excited states

First-principles quantum-chemical calculations for small lithium and sodium clusters reproduce not only the main resonances but also the fine structure (for a review, see Bonacic-Koutecky *et al.*, 1991). This is an important result, considering the extreme complexity of an *ab initio* calculation of such a size. For very small clusters the results are more accurate than those from self-consistent jellium calculations. Nevertheless, as shown above, the spherical and spheroidal jellium calculations also predict fine structure, and the experimental spectra are well reproduced.

Parallel with the two theoretical descriptions, two points of view have been adopted to describe the resonances. One is the plasmon model described above, which is a natural extension of the large-particle picture. Alternatively, the features can, of course, also be described more traditionally in terms of molecular states. There, the transitions are labeled according to the energies and symmetries of the initial and final molecular orbitals. In principle, this description is more accurate for describing detailed spectroscopic features.

However, serious doubts have been raised as to whether the resonances observed in small clusters are, in fact, plasmons, since ultimately the resonances are composed of envelopes of transitions rather than a single spectroscopic feature. But, as is clear from the discussions above, this aspect is also represented in the fragmented plasmon picture. Hence both points of view are probably formally equivalent. Certainly, including the ionic cores introduces additional fine structure in the optical spectra, but the most important features are already apparent in the jellium model.

N. Conclusion

The above survey of the optical properties of simple metal clusters gives an idea of the very rapid progress in this field. The interaction of light with simple metal clusters is reasonably well understood. Still, many outstanding theoretical questions remain only partly answered, for example, the decay of the electronic excited states, the coupling of the collective states with single-particle states, the coupling of these states with vibrational modes, and the effect of temperature on both the position and the widths of the resonances. Very recent femtosecond two-photon ionization experiments on small sodium clusters (Baumert *et al.*, 1992; Gerber *et al.*, 1993) are providing new insights into these dynamical properties.

Cluster spectroscopy up until now has addressed almost exclusively the electric dipole transitions in the visible and low-ultraviolet ranges. Extensions especially towards the infrared should be very interesting, since here magnetic dipole transitions (Devaty and Sievers, 1990), which have not at all been investigated in this size range, may dominate the optical response.

IX. CLUSTER DECAY PROCESSES

In nuclear and subnuclear physics much experimental information is obtained from decay processes. For cluster physics this is also true; in fact, almost all experimental probes involve the destruction or alteration of the cluster investigated. For example, in the photoionization process (Secs. VI and VII) an electron is ejected after photoexcitation, and the optical spectra (VIII) result from photodissociation processes. The focus of this section is the decay process itself.

Clusters dissociate after collisions with other particles or after absorbing photons. Dissociation proceeds spontaneously when clusters are so hot that the free energy is greater than the binding energy of a constituent atom, ion, or possibly larger fragment. This process is symbolically denoted as

$$X_N^* \rightarrow X_M^+ X_{(N-M)} \ , \tag{9.1}$$

where the X_N^* is an excited state of X_N. Usually the dissociation channel with $M=1$ is referred to as evaporation. The fragmentation products are generally vibrationally and/or electronically excited, so that evaporation chains may occur. Successive evaporation events produce an ensemble of hot clusters (for example, from a high-temperature source) ultimately giving rise to structured mass spectra as discussed in Sec. III.

Multiply charged clusters may also decay by fission into charged fragments. For doubly ionized clusters, this process is indicated by

$$(X_N^{++})^* \rightarrow X_M^+ + X_{(N-M)}^+ \ . \tag{9.2}$$

As for dissociation, fission can be induced by light or by collisions, or can occur spontaneously.

Several aspects of the decay processes can be investigated, such as the branching ratios of the various decay channels and their thresholds, as well as the associated decay time constants. For simple metal clusters there are only a few experimental decay studies, limiting comparisons between different systems. We first discuss theoretical aspects, then collision- and photoinduced dissociation of aluminum and potassium cluster ions, followed by the fission of potassium and gold cluster ions.

A. Statistical decay processes

The similarity of the products observed in the photodissociation and collision-induced dissociation of aluminum cluster ions suggests that similar processes are involved (Jarrold *et al.*, 1990). In both cases the excitation ultimately causes heating and dissociation. Hence to a large extent the excitation mechanism is decoupled from the dissociation. With this simplification, the dissociation channels and their rates as a function of deposited energy can be studied.

A particularly simple analysis of the statistical decay process is given by the RRK theory (Rice, Ramsperger, Kassel; see Rice and Ramsperger, 1927; Jarrold *et al.*, 1990), which relates the dissociation rate to the thermal energy and the dissociation energy of the particle. From the vibrational frequency ν and the number of vibrational degrees of freedom of the cluster $s=3N-6$, the dissociation rate can be crudely estimated in the RRK theory (Jarrold *et al.*, 1990):

$$k(E_0)=\nu\left[\frac{E_0-E_D}{E_0}\right]^{s-1} \ . \tag{9.3}$$

Here E_0 is the thermal energy, and E_0 is the dissociation energy of the particle.

To determine E_0 requires a model for the vibrational density of states and partition function. However, assuming a bulklike heat capacity, then $E_0=skT_0$; the RRK expression then gives, in the large-N limit,

$$k(T_0)=\nu\exp-(E_D/kT_0) \ , \tag{9.4}$$

which is the familiar Arrhenius rate equation for the evaporation of a specific atom in the cluster and hence should be multiplied by $N^{2/3}$ to account for the number of surface atoms. A similar expression is also derived by Klots (1991).

The more accurate RRKM theory (Markus, 1952; Engelking, 1987; Ray *et al.*, 1989; Jarrold *et al.*, 1990) treats the thermodynamics more carefully and is to be preferred over the RRK theory; however, for clusters it is often difficult to evaluate the relevant thermodynamic functions, especially at lower temperatures and certainly when phase transitions are important. A further shortcoming of this theory is that it neglects the electronic contribution to the free energies. This is reasonable only when the clusters can be considered to be in the electronic ground state. However, for larger clusters or at high temperatures this is no longer the case, and the theory should be appropriately modified (for a review of these effects, see Brack, 1993, Sec. III.B.3).

A practical approach estimates the evaporation rates from bulk vapor pressure information. For bulk metals it is well known that the evaporation rates are related to the vapor pressures, because of the balance of evaporating atoms and those that recondense on the surface (Langmuir evaporation; see, for example, Maisse and Glang, 1970, Ch. 1). It is found that

$$k(T)=\rho(T)A\left[\frac{kT}{2\pi m}\right]^{1/2} \ , \tag{9.5}$$

where m is the atomic mass, A is the area of the cluster, and $\rho(T)$ is the bulk vapor density at temperature T. This expression (which is essentially a reformulation of the law of mass action) can be further refined by taking the surface tension into account. Classically the internal pressure is σ/R, where σ is the surface tension, and small particles should have large internal pressures and correspondingly important increases in the vapor pressure (using the Clausius-Clapeyron equation).

Closely related to the RRKM theory is the expression

derived directly from the law of mass action, as in de Heer, Knight, *et al.* (1987). Alternatively, Bertsch *et al.* (1991) estimate the evaporation rates from the Weisskopf expression (Weisskopf, 1937) developed for nuclear decays. These theories relate the evaporation rates of small particles to the bulk vapor pressures.

B. Unimolecular decay of sodium cluster ions

Unimolecular decay of clusters in a molecular beam was first observed by Begemann *et al.* (Begemann, Dreihöfer, *et al.*, 1986; Begemann, Meiwes-Broer, and Lutz, 1986), who detected in-flight fragmentation of Al, Cu, and Si clusters. This mostly qualitative work was followed by several experiments that yielded qualitative information.

In a study of the thermodynamic properties of small sodium cluster ions, Bréchignac *et al.* (Bréchignac, Cahuzac, Leygnier, and Weiner, 1989; Bréchignac, Cahuzac, Leygnier, Pflaum, *et al.*, 1989) have investigated the decay rates of these clusters as a function of size. In this experiment clusters are produced in a high-temperature source in a neat expansion (i.e., without carrier gas).

They are subsequently subjected to an intense laser pulse that not only ionizes but also superheats the clusters, which then further decay primarily by evaporation of atoms and dimers. The kinetic energy of a cluster that evaporated during the acceleration phase in the time-of-flight analyzer will be reduced, so that from a subsequent measurement of these energies the evaporation rates can be extracted. These rates can be compared with the predictions from statistical decay theory (Engelking, 1987) to give the cluster dissociation energies for atom and dimer evaporation.

For sodium cluster ions Na_N^+ up to $N=36$, the dissociation energies for atom evaporation as function N is sawtoothlike, with maxima at $N=9$ (1.3 eV), 21 (0.93 eV), and 35 (0.95 eV) and minima at $N=4$ (0.6 eV), 10 (0.6 eV).

C. Photo- and collision-induced dissociation of aluminum clusters

Studies of decay processes of aluminum clusters have been carried out by Begemann *et al.* (Begemann, Dreihöfer, *et al.*, 1986; Begemann, Meiwes-Broer, and Lutz, 1986), Jarrold and co-workers (Jarrold *et al.*, 1986, 1987, 1990; Ray *et al.*, 1990), and Saunders *et al.* (1989). In these experiments cluster ions were mass selected with a quadrupole mass analyzer and passed through an ion guide. In the ion guide the clusters were either illuminated with laser light or collided against a controlled background of atoms. The ionic cluster fragments were mass analyzed by the second quadrupole. With this arrangement the dissociation rates and the fragmentation channels of mass-selected cluster ions could be measured as a function of photon energy or of collision energy.

The cohesive energies per atom for small aluminum cluster ions have been determined by measuring the evaporation rates as a function of absorbed photon energy and using the RRKM theory (Jarrold *et al.*, 1990). Results are shown in Fig. 49 and are compared with various theories. The simple classical model calculation in Fig. 49 (Ray *et al.*, 1989; Jarrold *et al.*, 1990) estimates the cohesive energy from bulk constants, i.e., assuming the bulk heat of evaporation H_0 and the bulk surface energy γ, to give

$$E_c(N)=NH_0-(4\pi)^{1/3}(3N)^{2/3}\gamma r_0^2 , \tag{9.6}$$

where r_0 is the radius of one atom in the bulk (i.e., for Al, $r_0=3^{1/3}r_s$). The agreement for larger clusters is reasonable.

Further information on the cluster properties is obtained from the branching ratios to different final states. For example, to determine ionization potentials, Jarrold *et al.* (1987) considered the branching ratios of the collision-induced dissociation channels,

$$\begin{aligned} Al_{N^+} &\rightarrow Al_{N-1}+Al^+ \\ &\rightarrow Al_{N-1}^+ + Al , \end{aligned} \tag{9.7}$$

and showed that

$$\ln I(Al^+)/I(Al_{N-1}^+)=(IP_{N-1}-IP_1)/kT , \tag{9.8}$$

where I is the measured intensity and IP the adiabatic ionization potential. Hence, from the branching ratio and an estimate of the temperature of the dissociating cluster, the cluster ionization potentials may be derived.

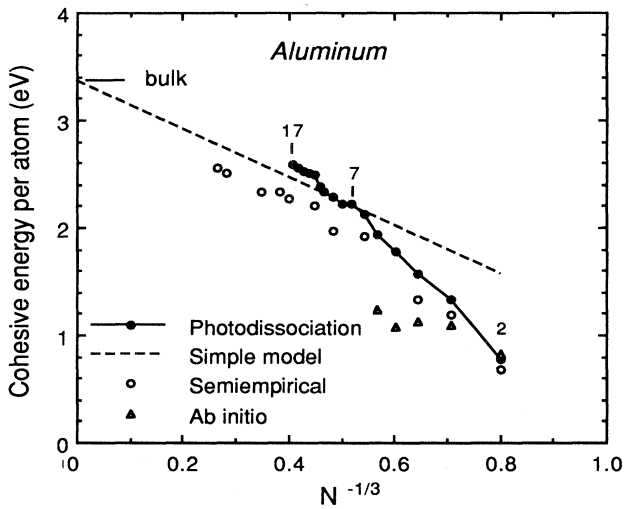

FIG. 49. Cohesive energies per atom for aluminum clusters determined in photodissociation studies: solid circles, experimental (Ray *et al.*, 1989); open circles, semiempirical model by Pacchioni and Fantucci (1987); triangles, *ab initio* calculations by Upton (1987); dashed line, classical model. After Ray *et al.*, 1989.

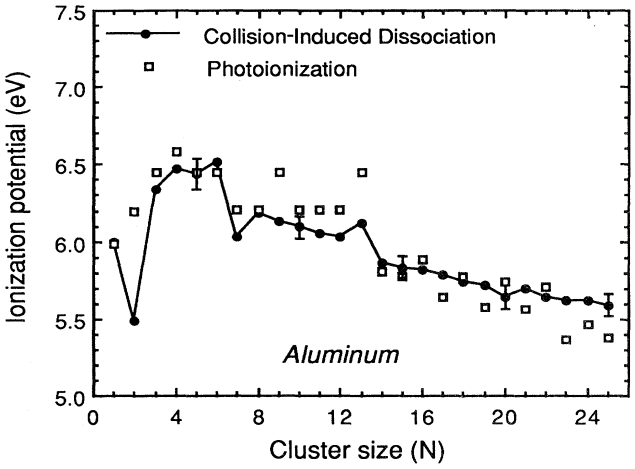

FIG. 50. Ionization potentials of aluminum clusters as determined from collision-induced dissociation studies compared with those found from photoionization studies. After Jarrold *et al.*, 1987.

Results are shown in Fig. 50. Despite the indirectness of this method, the cluster ionization potentials thus determined agree well with the photoionization studies discussed in Sec. VI.D.2. Moreover, this method should give directly the adiabatic ionization potential (Sec. VI).

D. Fission

Multiply charged clusters are produced with relatively high abundances in liquid-metal ion sources, sputtering sources, or, alternatively, by photoionizing neutral clusters. Multiply charged clusters have a tendency to fission, i.e., to disintegrate into two large charged fragments, due to the Coulomb repulsion. In contrast, disintegration of neutral clusters usually proceeds by evaporation of atoms and dimers, as mentioned above.

Fission may be induced by photon absorption or by collisions with background gas atoms, or it may occur spontaneously if the clusters are initially hot enough. As in the dissociation processes discussed above, important conclusions can be drawn from both the dissociation rates and the branching ratios. An interesting aspect of multiply charged clusters is that there should be a limit to how small the cluster may be and still be stable.

The fission of doubly charged silver (Katakuse, 1990), gold (Saunders, 1990; Saunders and Dam, 1991), and sodium (Bréchignac *et al.*, 1990) have been studied. Some results are discussed below.

1. Fission of multiply charged sodium clusters

Clusters produced with a high-temperature nozzle source have been multiphotoionized with a high fluence of 4.66-eV photons, producing both singly and doubly charged clusters (Bréchignac *et al.*, 1990). The cluster ions are mass selected. After a drift time of 50 μs, a mass analysis of the selected clusters is performed. The ionic daughters of those clusters that dissociated or fissioned during the drift time will be detected, and from their intensities the fission probabilities and branching ratios are determined.

For doubly charged sodium clusters, two effects are observed. One is that the smallest positively identified doubly charged sodium cluster is Na_{27}^{2+}. It is observed that Na_{27}^{2+} may fission to $Na_{13}^{+}+Na_{14}^{+}$ or evaporatively by dissociate to $Na_{26}^{2+}+Na$. These processes proceed with comparable probabilities. For larger clusters, evaporation dominates. Using simple arguments, this has been taken as evidence that for Na_{27}^{2+} the fission barrier approximately equals the dissociation energy for evaporating one atom (see below).

More recently, Martin *et al.* (1992) investigated the fission of highly charged sodium clusters. The clusters were produced in a gas-aggregation cluster source and multiply ionized with light from an ArF excimer laser (6.4 eV photon energy). The ions were subsequently heated, causing evaporative shrinking. In this process the final mass spectra reveal the multiply charged sodium clusters Na_N^{z+}, which for each charge state z show a reasonably well defined critical size N_c. The critical sizes for $z=2$, 3, 4, 5, 6, and 7 are found to be approximately 27, 64, 123, 208, 321, and 448, respectively.

2. Fission of gold clusters

Saunders (1990) produced mass-selected beams of multiply charged gold clusters from a liquid-metal ion source. The clusters were collided against inert-gas

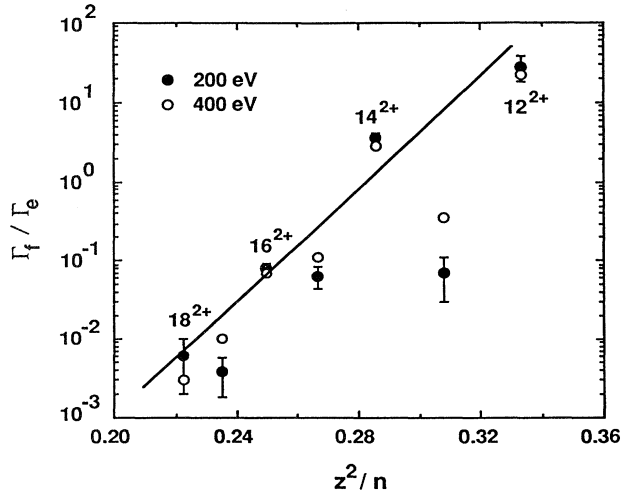

FIG. 51. Ratio of the total fission rate Γ_f to the evaporation rate Γ_e for Au_N^{2+} clusters (i.e., the charge $z=2$). Data are taken for two center-of-mass collision energies, and the ratio depends only weakly on the collision energy. After Saunders, 1990.

atoms, and the ionic fragments were subsequently mass analyzed. The branching ratios to various final states were determined.

An analysis of the daughter clusters from parents in the range Au_9^{2+} to Au_{18}^{2+} shows several regularities:

(1) There is a strong odd-even alternation in the fissionability of the clusters, with the probability of fission relative to evaporation for even clusters being larger than for the neighboring odd clusters;

(2) As the parent size decreases, the probability of fission relative to evaporation increases strongly.

Details of the fission branching ratios are discussed by Saunders (1990). Figure 51 shows the ratio of the fission rate Γ_f to the evaporation rate Γ_e for small doubly charged gold clusters, plotted versus Z^2/N. These results are discussed below (see also Saunders and Dam, 1991).

3. Liquid-drop model for fission

In nuclear physics several simple models are used to explain nuclear properties. The nuclear shell model explains the nuclear stabilities and energy-level structures. It is essentially this model that was adapted for simple metal clusters, and it seems that for these systems it applies even better than for the nuclei.

Complementary to the shell model is the liquid-drop model used for nuclear fission processes (Bohr and Wheeler, 1939). This model has been adapted for clusters by Saunders (1990; see also Saunders and Dam, 1991), who considered the cluster as a uniformly charged liquid drop. The shape is determined by a competition between the surface tension, which tends towards spheres, and electrostatic energy, which tends towards elongated shapes. An analysis of the total energy as a function of shape shows that fission requires an energy barrier to be overcome. Saunders (1990) found that this barrier vanishes, and spontaneous fission occurs if the value of (Z^2/N) exceeds the critical value

$$\frac{Z^2}{N_c}=10\frac{4\pi}{3}\frac{r_s^3\sigma}{e^2}\ , \tag{9.9}$$

where σ is the surface tension and e is the electronic charge. For Au, the calculated critical size for doubly charged clusters is $N=5$, which is reasonably consistent with the smallest experimentally observed $N=9$. For sodium clusters investigated by Martin *et al.* (1992), it was found that the multiply charged clusters were stable when $(Z^2/N)\leq 0.125$.

From the liquid-drop model it is possible to estimate fission barrier heights from the branching ratios between evaporation and fission channels (Saunders, 1990). For example, for Au_{14}^{2+}, the branching ratio is close to unity, indicating that the fission barrier height is about equal to the evaporation energy. In this case the liquid-drop model predicts a fission barrier of 2.3 eV, which is close to the gold dimer binding energy and hence considered to be a reasonable value. Saunders (1990) also applied this model to Na_N^{2+} and found reasonable agreement with the experimental critical size of Bréchignac *et al.* (1990). The fission of sodium clusters has been studied theoretically by Nakamura *et al.* (1991) and by Lipparini and Vittori (1990). A review of cluster fission can be found in Sugano (1991).

Despite the success of this model, it must be cautioned that the shell structure effects are not taken into account. Certainly the fission process is a complex phenomenon involving details of the electronic and geometrical structure as the cluster passes over the fission barrier. Indeed, the fission process should be considered as an important frontier of metal cluster physics.

X. CONCLUSION AND OUTLOOK

Throughout this review shell-model concepts have been used extensively to illuminate the observed cluster properties. The electronic shell structure is the unifying principle tying together cluster systems as diverse as lithium and gold. The experimental evidence for electronic shell structure is overwhelming, and the shell model will certainly survive further experimental and theoretical tests. However, electronic shell structure is, in fact, simply a consequence of the boundary conditions of the nearly free electrons in small particles of simple metal clusters. Its success hinges on little more than that the free electrons dictate the geometrical configuration of the ionic cores. The cores respond to the electric forces and ultimately provide a neutralizing background for the electrons. It is as if the cores are drifting in the Fermi sea, held in place by the electric forces. Since the volume occupied by the free electrons is much greater than that of the cores, this is not far from reality.

Historically the nearly-free-electron theory for bulk simple metals was used as a starting point for understanding the electronic properties of metals. However, the model is quite sterile, making all metals essentially alike, with the electronic density being the only parameter. As for the bulk, the limitations of this description are obvious and become apparent when a property is investigated in more detail. For example, the Wigner-Seitz radius of lithium is only slightly greater than that of gold, and yet these two metals could hardly be more different: lithium is highly reactive, gold is chemically almost completely inert; gold is colored, lithium virtually colorless; lithium is the lightest metal, gold is one of the heaviest, etc. The lack of subtlety and nuance of the free-electron models is obvious. Electronic shell and related effects are certainly pervasive, but give little more than the basic electronic structure, just as the nearly-free-electron approximation gives only the basic electronic structure of the conduction electrons in the bulk.

The greatest merit of the shell model is that it provides a guiding principle for further experiments and theories.

In fact, most likely the most interesting developments will be those which reveal deviations from the simple picture.

Although it is not possible to predict which directions will be most fruitful in illuminating the multitude of variations and deviations of the simple models, certain investigations along several avenues are clearly indicated. There are, for example, the chemical properties, the dynamic and thermodynamic properties, questions concerning phases and phase transitions, and questions concerning transport properties including electrical and thermal conductivities, as well as the radiationless decays of electronic excitations.

This review has concentrated on the simple metal clusters, and perhaps we may conclude that they live up to their name. But then there are, of course, the clusters of nonsimple metals. These metals have traditionally been most important for their chemical and physical properties. Taking iron as an example, we see that clusters of this metal are ferromagnetic down to the smallest sizes. Their magnetic properties are not only fascinating, but could also become of great technological importance. Not only do iron clusters lack shell structure, even their ionization potentials depart from the behavior found for simple metal clusters. A detailed discussion of the physical and chemical properties of nonsimple metal clusters investigated to date would fill several volumes (and to my knowledge does not exist). In fact, even a brief survey of this field leaves one with a sense of its enormous richness (Sugano, 1991) and at the same time an awareness of its apparent lack of unity, in stark contrast with the subject of this review.

Although theoretically the foundations of the physics of simple metal clusters are well understood, much work remains to be done. In the text are many examples of less understood properties. However, since a solid foundation exists, it is clear that, continuing along the current paths, answers to most if not all of these questions will be found, contributing substantially to our understanding of condensed matter.

ACKNOWLEDGMENTS

First and foremost I want to thank my wife, Patty, and my daughter Wendy for their support in all phases of this very difficult task. Of the many people who helped, I am particularly grateful to George Bertsch, Sven Bjørnholm, Pietro Ballone, and Karl Heinz Meiwes-Broer for encouragement and for their many helpful suggestions and corrections in the manuscript. I also thank Rob Whetten, Karl Heinz Meiwes-Broer, Kit Bowen, Martin Jarrold, Manfred Kappes, Pat Martin, and Vitaly Kresin for figures and for providing experimental results prior to publication. Last but certainly not least, I am deeply indebted to Matthias Brack for his participation in this project and for the many helpful suggestions he provided.

APPENDIX A: SHELL MODEL FOR METAL CLUSTERS

1. Three-dimensional isotropic oscillator

The effective single-particle potential of a cluster can be approximated in various ways. Our purpose here is to construct one simple enough that order-of-magnitude estimates of physical properties can be obtained with very little effort. First, we examine the properties of a three-dimensional harmonic oscillator on which the Clemenger-Nilsson model is based. This model for clusters was originally proposed by Clemenger (1985) and is based on the nuclear model of Nilsson (1955; see also Gustafson *et al.*, 1965 and Bohr and Mottelson, 1975, pp. 231–233). It is used extensively in this review.

Hence the effective single-particle Hamiltonian for electrons with mass m is

$$H=\frac{\mathbf{p}^2}{2m}+\frac{m\omega_0^2\mathbf{q}^2}{2}-Uh\omega_0[l^2-n(n+3)/6]\ , \tag{A1}$$

where p and q are single-electron momentum and coordinate operators, l is the angular momentum, and n is the shell number. The third, anharmonic correction term modifies the shape of the well and is constructed to keep the average shell energy constant. The spatial extent of the electronic charge density $\langle r^2\rangle$ is determined by the shape of the well and by the oscillator frequency ω_0 (see also Clemenger, 1985 and de Shalit and Feshbach, 1974, pp. 194–199). Relating $\langle r^2\rangle$ to the size of the cluster, $R_0=r_sN^{1/3}$ fixes $\hbar\omega_0=E_F/N^{1/3}$, where E_F is the bulk Fermi energy and r_s is the Wigner-Seitz radius.

While this energy scaling is reasonable compared with jellium calculations and correctly describes the large-N limit, it is often useful to adjust the energy scale for smaller clusters by comparing with jellium calculations. From those calculations it is noticed that the shell steps are smaller than predicted above. This can be understood as arising from a decreased electronic density, which in turn is related to the fact that the electronic cloud extends beyond the jellium surface. In particular, it is known from jellium calculations on bulk surfaces (Lang and Kohn, 1973) and for clusters (Ekardt, 1984) that the effective radius of the electronic cloud is larger than the jellium sphere radius, due to the spilling out of the electronic charge. Consequently the electronic density and hence the Fermi energy is reduced, compared with the bulk value. In particular, if the effective electronic radius is $R_0+\delta$, then the above argument gives

$$h\omega_0(N)\approx E_F^*N^{-1/3}=\frac{E_FN^{-1/3}}{(1+\delta/R_0)^2}\ . \tag{A2}$$

The spherical shell model predicts an energy eigenvalue spectrum

$$E_n=h\omega_0\{(n+\tfrac{3}{2})-U[l^2-n(n+3)/6]\}\ . \tag{A3}$$

These levels as a function of U are displayed in Fig. 52 in units of $h\omega_0$. With appropriate choices for U (which may

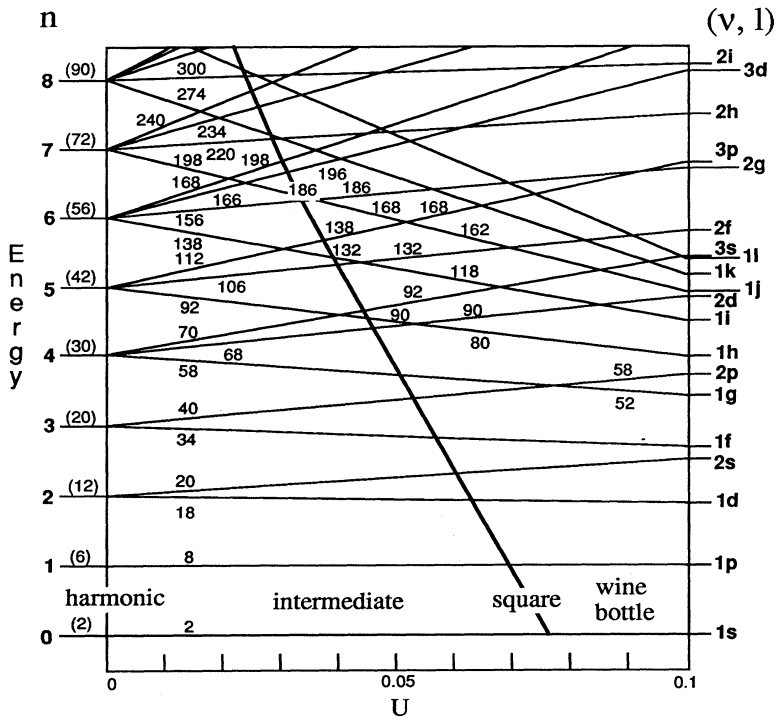

FIG. 52. Single-particle energy levels as a function of the anharmonic distortion parameter U. $U=0$ corresponds to the harmonic oscillator; for positive values of U, the curvature of the bottom of the well is reduced as indicated. The unit of energy is approximately $E_F/N^{1/3}$, as described in the text.

depend on n), this model can roughly reproduce the level structures of the various wells (Fig. 52). Moreover, if the level diagram is extended to negative values of U, the energy shells of the Coulomb potential are approximately reproduced. Positive values of U increase the energies of the lower angular momentum states and decrease the higher ones, thus having an effect similar to that of decreasing the curvature at the bottom of the well (i.e., from harmonic to square and continuing to wine-bottle shaped). Note further that the U values are rather small. In fact, assuming $U=0$ is a reasonably good approximation for small clusters.

2. Ellipsoidal shell model

a. Clemenger-Nilsson model

The basic assumption of the Clemenger-Nilsson (CN) model (Clemenger, 1985; de Heer, Knight, *et al.*, 1987), as in the Nilsson (1955) model, is that for fixed volume the cluster shape adjusts to minimize the total electronic energy. Ignoring the anharmonic term [i.e., $U=0$, Eq. (A2)] gives the eigenvalues as a function of the shape,

$$E(n_x,n_y,n_z)=\hbar\omega_0\left[(n_x+\tfrac{1}{2})\frac{R_0}{R_x}+(n_y+\tfrac{1}{2})\frac{R_0}{R_y}+(n_z+\tfrac{1}{2})\frac{R_0}{R_z}\right], \tag{A4}$$

where R_x, R_y, and R_z are the semiaxes of the ellipsoid, and n_x, n_y, and n_z are the harmonic-oscillator quantum numbers [i.e., for the $1s$ state, $(n_x,n_y,n_z)=(0,0,0)$; for the $1p$, they are (1,0,0), (0,1,0), and (0,0,1); for the $n=2$ corresponding to the $1d,2s$ levels, they are (2,0,0), (0,2,0), (0,0,2), (1,1,0), (0,1,1), etc.]. The volume is constrained by $R_xR_yR_z=R_0^3$.

If the shapes are further constrained to spheroids ($R_x=R_y$), then the single-particle energy levels can be expressed in terms of the distortion parameter

$$\eta=2\frac{R_z-R_x}{R_z+R_x}\ . \tag{A5}$$

The Clemenger-Nilsson diagram, Fig. 53 (Clemenger, 1985a), shows the single-particle energies as a function of η, as mentioned in Sec. II. (Here the anharmonic distortion is included with $U=0.04$, so that the spherical shell splittings correspond with those calculated in self-consistent spherical jellium calculations.)

The CN diagram hence represents the single-particle energies as a function of the cluster shape. The reduction of the symmetry from spherical to spheroidal lifts orbital degeneracies, as can be seen in the CN diagram for $\eta\neq0$. Besides the spin degeneracies, the remaining degeneracies (i.e., for $l_z\neq0$, which are twofold degenerate) are lifted in the ellipsoidal model, below.

The total electronic energy can be expressed in terms of the single-particle energies. For the harmonic single-particle potential it can easily be shown that the total electronic energy is related to the sum of the single-particle energies (see, for example, Preston and Bhaduri, 1975, p. 421):

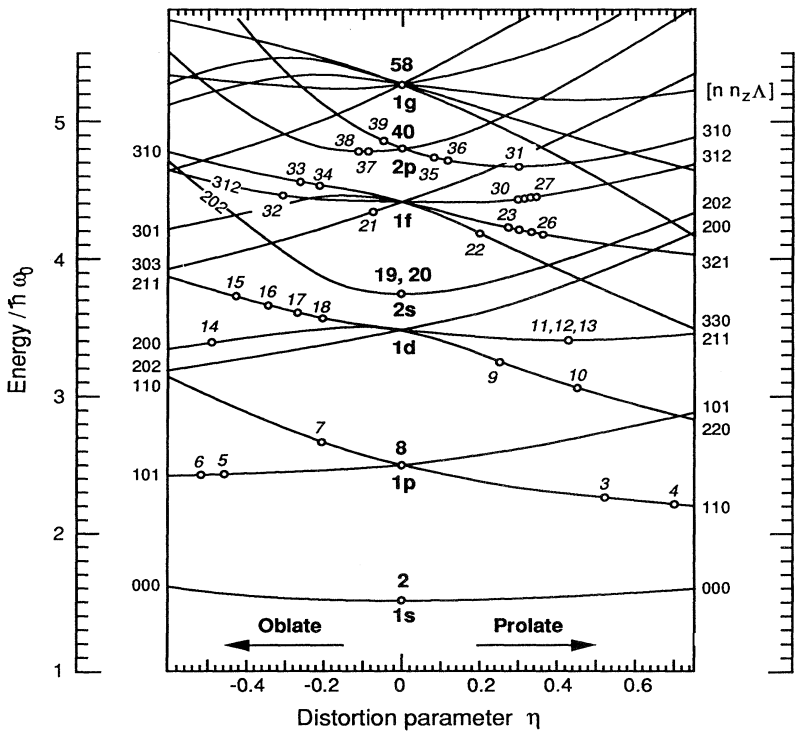

FIG. 53. Clemenger-Nilsson diagram (after Clemenger, 1985). Cluster numbers are positioned at the highest occupied levels and at the equilibrium configuration η. For a detailed description, see the text.

$$E_{\rm tot}(\eta,N)=\tfrac{3}{4}\sum E(\eta,n_x,n_y,n_z)\ . \tag{A6}$$

The resulting total electronic energy curve has a minimum at $\eta_0(N)$ and is indicated by a dot at the highest occupied level in the CN diagram. By this procedure we find that the closed-shell clusters, i.e., 2,8,20, . . . , are spherical ($\eta=0$) and that open-shell clusters are either oblate or prolate spheroids. An interesting exception (there are many others) is 34, which in the CN model is ellipsoidal and a subshell closing rather than a spherical shell closing. In addition, 18 is spheroidal when $U=0$, but spherical for $U>0.02$.

To obtain the energy levels of a specific cluster, one draws a vertical line through $\eta_0(N)$, and the interceptions with the energy-level curves correspond with the energy levels of the cluster. The CN diagram is truly a remarkable (although obviously highly simplified) device representing at once the single-particle energy-level structures for all clusters.

Figure 54 shows the energy-level structure for spheroidal clusters including the energy scaling as in Eq. (4.2). The agreement with theoretical approaches is improved over Fig. 5 due to the inclusion of electronic spillout effects.

Including the anharmonic term is important mainly for larger clusters and causes splittings in the spherical harmonic-oscillator shells, for example, between the $1p$ and the $2s$ levels. With this term the analysis is slightly more complicated.

b. Ellipsoidal distortions

The cluster shapes in the previous subsection were constrained to be spheroidal, i.e., $R_x=R_y$. Removing this constraint allows the clusters to assume ellipsoidal shapes. If the anharmonic term is neglected (i.e., $U=0$), the total energy is

$$\begin{aligned}E_{\rm tot}&=h\omega_0R_0\sum_{\rm occ}\left[(n_x+\tfrac{1}{2})\frac{R_0}{R_x}+(n_y+\tfrac{1}{2})\frac{R_0}{R_y}\right.\\&\qquad\left.+(n_z+\tfrac{1}{2})\frac{R_0}{R_z}\right]\\&=h\omega_0R_0\left[\frac{C_x}{R_x}+\frac{C_y}{R_y}+\frac{C_z}{R_z}\right],\end{aligned} \tag{A7}$$

where $R_xR_yR_z=R_0^3=Nr_s^3$. It is trivial to find the equilibrium cluster shapes analytically [i.e., $(R_{x0}/R_0)^3=C_x^2/C_yC_z$, etc.] as given in Table I (see also Selby *et al.*, 1989). Alternatively (following Hill and Wheeler, 1953; Saunders, 1986b), for ellipsoidal clusters it is sometimes convenient to define the shapes in terms of the parameters β and γ, which, expressed in terms of the principle axes, gives

$$\begin{aligned}R_x&=R_0\exp\{-5/4\pi\beta\cos(\gamma-2\pi/3)\}\ ,\\R_y&=R_0\exp\{-5/4\pi\beta\cos(\gamma-2\pi/3)\}\ ,\\R_z&=R_0\exp\{-5/4\pi\beta\cos(\gamma)\}\ .\end{aligned} \tag{A8}$$

Note that β is related to η in the spheroidal case by $\beta=(8\pi/15)\ln(2-\eta)/(2+\eta)$. This coordinate system is particularly useful for describing the shape vibrations of the system (Hill and Wheeler, 1953).

The ground-state total-energy surfaces may also be represented simply as functions of R_x and R_y ($R_z=R_0^3/R_xR_y$). Figure 55 shows examples (assuming $U=0$). Here it is evident that Na_8 is spherical (since the lowest energy occurs for $R_x=R_y=R_z=R_0$), Na_9 and Na_{10} are spheroidal, and Na_{12} ellipsoidal. Further, note that the three wells in Na_9, Na_{10} and the six wells in Na_{12} are equivalent, involving only interchanges of the axes.

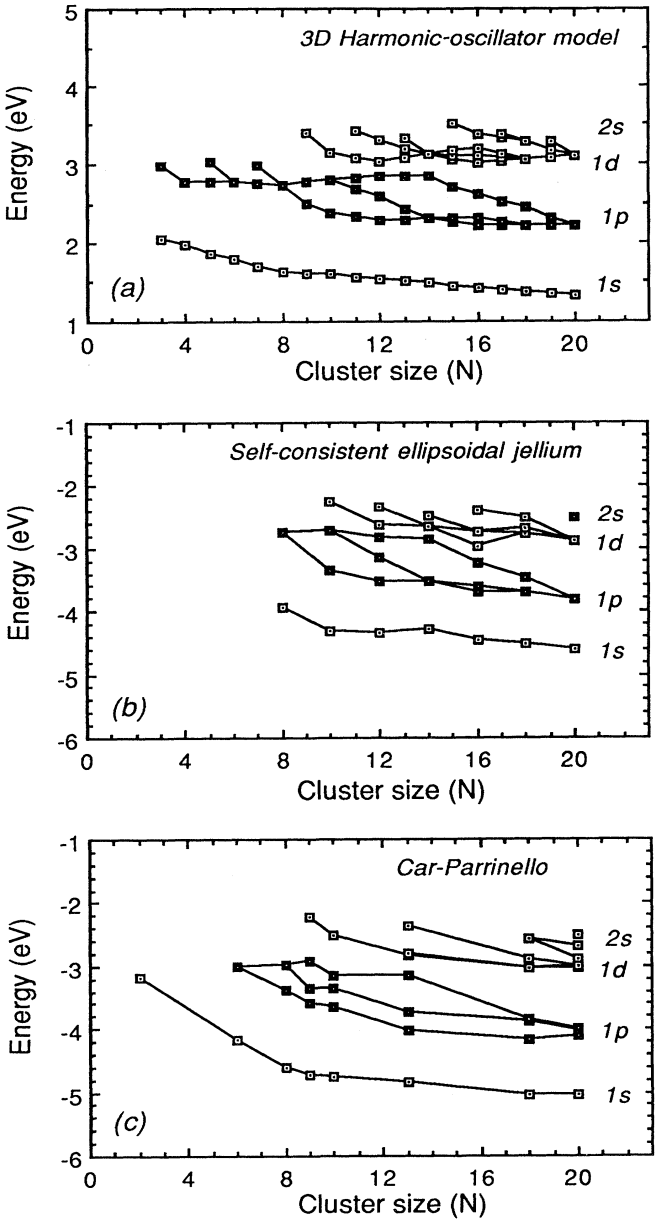

FIG. 54. Energy eigenvalues from the ellipsoidal shell (Clemenger-Nilsson) model: (a) the self-consistent spheroidal jellium calculations (from Lauritsch *et al.*, 1991); (b) the Car-Parrinello molecular-dynamics calculations (from Röthlisberger and Andreoni, 1991).

APPENDIX B: SURFACE-PLASMON LINE SHAPES

1. Elastic properties in the ellipsoidal shell model

For small clusters the surface plasma resonances are thermally broadened by couplings to the vibrational states. In order to find the thermal widths of electronic excitations in the cluster, one must first determine the elastic properties. The dependence of the total energy with respect to ellipsoidal deformations in which the total volume is conserved is explicit in the ellipsoidal model (Appendix A); hence the elastic constants associated with the corresponding quadrupole vibrational modes can be found immediately from Eq. (A6).

It is important to note that the cluster shapes result only from considerations of the total electronic energies of the nearly free electrons. In particular, there is no explicit surface-tension term that would tend towards more spherical shapes; however, the good agreement of the shapes calculated in this model and those from the self-consistent spheroidal jellium model indicates that surface effects are already adequately represented. Hence we may assume that the shape dependence of the total energy is reasonably well described for deformations that conserve the total volume (as for the quadrupole vibrations to first order) and where the shapes are constrained to ellipsoids.

Besides the quadrupole vibrations, the breathing vibrations (i.e., vibrations in which three axes uniformly expand and contract: $\delta R_x/R_x=\delta R_y/R_y=\delta R_z/R_z$) also contribute to the linewidth, as shown below. To determine the elastic constant of this vibrational mode, recall that the electron-gas estimation of the bulk modulus for the alkali metals (except lithium) reproduces the experimental values within about 10% (Ashcroft and Mermin, 1976). This estimate assumes that the restoring force upon a deformation is dominated by the contribution of the kinetic energy of the electrons, so that the bulk modulus $B=\frac{2}{3}\rho E_F$ (Ashcroft and Mermin, p. 39), where ρ is the electron density. Applying the same reasoning to clusters within the model presented here yields for the monopole deformations about the equilibrium configuration

$$\frac{d^2E_{\rm tot}}{dR_i^2}=\frac{9}{2}\frac{\hbar\omega_0(C_xC_yC_z)^{1/3}}{R_i^2}\ , \tag{B1}$$

where the C_i are defined in Appendix A. Although this is certainly a crude estimation at best, it does lead to reasonable predictions, as demonstrated in Appendix C. Unfortunately, no corresponding jellium model values are available.

TABLE I. Cluster shapes from the ellipsoidal shell model. The C_i are defined in Eq. (A7), and R_i are the normalized axes ($R_xR_yR_z=1$). The electronic configuration follows a sequential *aufbau* scheme, and the last added electron is given in the Conf. column. The one-electron configurations $a=(n_x,n_y,n_z)$ correspond to $s=(0,0,0)$; $p1=(1,0,0)$; $p2=(0,1,0)$; $p3=(0,0,1)$; $sd1=(2,0,0)$; $sd2=(1,1,0)$; $sd3=(0,2,0)$; $sd4=(0,1,1)$; $sd5=(1,0,1)$; and $sd6=(0,0,2)$.

N	Conf.	C_x	C_y	C_z	R_x	R_y	R_z
1	s	0.5	0.5	0.5	1	1	1
2	s	1	1	1	1	1	1
3	$p1$	2.5	1.5	1.5	1.4	0.84	0.84
4	$p1$	4	2	2	1.58	0.79	0.79
5	$p2$	4.5	3.5	2.5	1.32	1.02	0.73
6	$p2$	5	5	3	1.18	1.18	0.71
7	$p3$	5.5	5.5	4.5	1.06	1.06	0.87
8	$p3$	6	6	6	1	1	1
9	$sd1$	8.5	6.5	6.5	1.19	0.91	0.91
10	$sd1$	11	7	7	1.35	0.86	0.86
11	$sd2$	12.5	8.5	7.5	1.34	0.91	0.80
12	$sd2$	14	10	8	1.34	0.96	0.77
13	$sd3$	14.5	12.5	8.5	1.25	1.08	0.73
14	$sd3$	15	15	9	1.18	1.18	0.71
15	$sd4$	15.5	16.5	10.5	1.11	1.18	0.75
16	$sd4$	16	18	12	1.05	1.19	0.79
17	$sd5$	17.5	18.5	13.5	1.07	1.13	0.82
18	$sd5$	19	19	15	1.08	1.08	0.85
19	$sd6$	19.5	19.5	17.5	1.03	1.03	0.93
20	$sd6$	20	20	20	1	1	1

2. Surface plasma resonances

The dipole photoabsorption spectra of small alkali clusters are well described in the Drude model (Sec. VIII.F). For spherical clusters the frequencies are given by

$$\omega_M=\left[\frac{4\pi\rho e^2}{3\varepsilon_\infty m}\right]^{1/2}, \tag{B2}$$

where ρ is the electronic density, m the electronic mass, e the electronic charge, and ε_∞ the core contribution to the dielectric function (Kittel, 1976). It should be noted that in many calculations ε_∞ is taken to be unity. Although the core correction is small, it is not negligible [i.e., for Na $\varepsilon_\infty\approx1.05$ and for K $\varepsilon_\infty\approx1.2$, as determined from optical constants (Raether, 1965, p. 84; see also Kittel, 1976); however, many calculations ignore the core polarizability shifts]. Often the electronic density is related to the polarizability α (Sec. V), i.e., $\rho=(3N/4\pi\alpha)$, so that the surface plasma resonances can be related to the measured polarizabilities. Here we estimate the density from the effective electronic cluster radius $R^*=(R_0+\delta)$ as in Sec. V.B and Appendix A.

A straightforward extension allows the resonances along the three axes to be calculated; however, the depolarization factors for the ellipsoid must be taken into account (de Heer, Knight, Chou, and Cohen, 1987). From the general expression for the depolarization factors (Stoner, 1945), it can be shown that to lowest order

$$\omega_{Mi}(R_i)=\omega_{M0}\left[1-\frac{3}{5}\frac{R_i-R_0}{R_0}\right], \tag{B3}$$

where the equilibrium shape R_i/R_0 is determined in Appendix A.2, and ω_{M0} is found from Eq. (B2) with the corrected density $\rho^*=\rho(R/R^*)^3$.

Whereas this model nicely describes the location of the surface plasma resonances, as shown in Sec. VII.F, it does not describe the experimental widths. They are, however, easily obtained from the model presented here.

The shape dependence of the resonance [Eq. (B3)] combined with the shape dependence of the total energy for the quadrupole and monopole vibrations gives a prediction for the resonance shape. This is illustrated in Fig. 56, which shows the total-energy surfaces for Na_8 before and after electronic excitation (here only the quadrupole vibration is included). Since the probability that the cluster has a configuration given by R_x,R_y,R_z is proportional to the Boltzmann factor, $P(R_x,R_y,R_z)=K\exp[-E_{\text{tot},0}(R_x,R_y,R_z)/kT]$ where T is the temperature of the cluster. With the assumption that the electronic excitation is vertical (i.e., involves no change in the shape of the cluster), the quadrupole vibrations give rise to a Gaussian line shape as shown below.

For small variations about the equilibrium configuration, for quadrupole vibrations (i.e., subject to $R_xR_yR_z=R_0^3$),

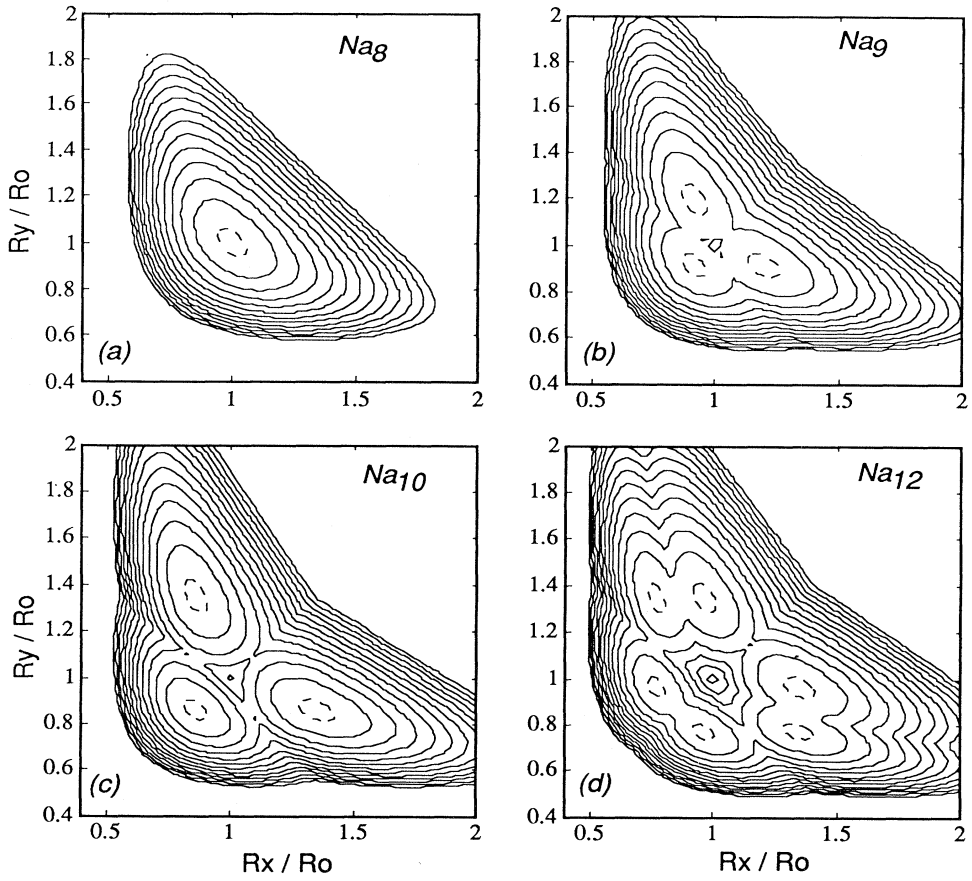

FIG. 55. Total-energy surfaces of several sodium clusters as a function of R_x and R_y, calculated in the ellipsoidal shell model. Contours are spaced every 0.2 eV. The dashed line corresponds to the 0.025-eV (room-temperature) contour. Na_8 is spherical, Na_9 and Na_{10} are spheroidal, and Na_{12} is ellipsoidal. From these figures the extent of the thermal tails in photoionization efficiency spectra are estimated as described in the text.

$$E_{\rm tot}(R_x+\delta R_x,R_y+\delta R_y)=E_{\rm tot}(R_x,R_y)+\frac{3}{4}\left\{\frac{C_yC_z}{C_x}-\frac{1}{4}\left[\frac{C_yC_z}{C_x^2}\right]^{1/3}C_z\right\}\delta R_x^2+\left\{\frac{C_y}{R_y^2}\delta R_y+\frac{C_z}{2}\delta R_x\right\}^2$$
$$=E_{\rm tot}(R_x,R_y)+K_{\rm quad}(x)\delta R_x^2+\left\{\frac{C_y}{R_y^2}\delta R_y+\frac{C_z}{2}\delta R_x\right\}^2, \tag{B4}$$

where for convenience $R_0=1$ and $h\omega_0=1$.

The surface-plasmon energy ω_{Mx} is given by

$$\omega_{Mx}(R_x+\delta R_x,R_y+\delta R_y)=\omega_{M0}\left[1-\frac{3R_x}{5}\right]-\frac{3\omega_{M0}}{5}\delta R_x$$
$$=\omega_{Mx}(R_x)-\frac{3\omega_{M0}\delta R_x}{5}, \tag{B5}$$

where ω_{M0} is defined in Eq. (B2). Hence

$$\delta R_x=-\frac{5\delta\omega_{Mx}}{3\omega_{M0}}. \tag{B6}$$

The probability of a deformation $\delta R_x,\delta R_y$ is given by the Boltzmann factor

$$P(\delta R_x,\delta R_y)=K\exp-\frac{E_{\rm tot}}{kT}=K\exp\left[-\frac{K_{\rm quad}(x)\delta R_x^2}{kT}\right]\exp\left\{-\frac{[(C_y/R_y^2)\delta R_y+(C_z/2)\delta R_x]^2}{kT}\right\}. \tag{B7}$$

Integration with respect to δR_y is trivial and yields a constant. Substituting δR_x from Eq. (B6) then gives the surface-plasmon absorption spectrum of this component,

$$P_x(\omega)=K'\exp-K^*_{\rm quad}(x)\left[\frac{\omega_{Mx}(R_x)-\omega}{\omega_{M0}}\right]^2\Big/kT\ ,$$
$$K^*_{\rm quad}(x)=\left[\frac{C_yC_x}{C_x}-\frac{1}{4}\left[\frac{C_yC_z}{C_x^2}\right]^{1/3}C_z\right]\ . \tag{B8}$$

Likewise, the monopole contribution gives a Gaussian with

$$K^*_{\rm mono}(x)=\tfrac{25}{4}(C_xC_yC_z)^{1/3}h\omega_0\ . \tag{B9}$$

Combining these two contributions results in a Gaussian line shape corresponding to oscillations along the x axis,

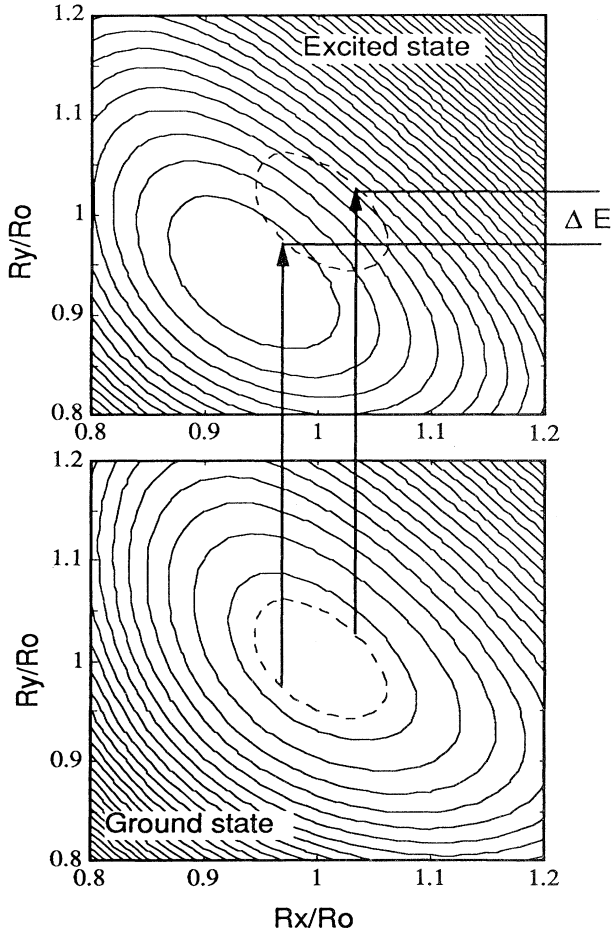

FIG. 56. Total-energy surfaces for Na_8 and the plasmon-excited Na_8^* as calculated in the ellipsoidal shell model. Contours are spaced every 0.05 eV. Note the important shape change caused by the plasmon excitation. The dashed line corresponds to the 0.025-eV (room-temperature) contour. Vertical arrows indicate the photoexcitation process and ΔE ($\approx$0.25 eV) the thermal width of the plasma resonance.

$$P_x(\omega)=K'\exp-K^*_{\rm tot}(x)\left[\frac{\omega_{px}(R_x)-\omega}{\omega_{p0}}\right]^2\Big/kT\ ,$$
$$K^*_{\rm tot}(x)=\{[K^*_{\rm mono}(x)]^{-1}+[K^*_{\rm quad}(x)]^{-1}\}^{-1}\ ; \tag{B10}$$

hence

$$P(\omega)=K'\sum P_x(\omega)\ . \tag{B11}$$

Analogous equations are found for the y and z modes. Note that for the spherical clusters ($C_x=C_y=C_z$), $(K_{\rm tot}/K_{\rm quad})^{1/2}=0.87$, so that about 87% of the width is due to the quadrupole vibrations and 13% to the monopole vibrations.

The calculated surface plasmons for clusters 1–20 together with the experimental data are presented in Fig. 57. The experimental cluster temperatures are estimated to be 300 K, consistent with estimates for the evaporative ensemble generally used to estimate the cluster temperatures from the source used in these experiments (Klots, 1988).

It is clear that this model, which uses only the bulk r_s value and the spillout factor $\delta=1.6$ a.u. as parameters, gives remarkable predictions in not only the positions but also the widths of the surface plasmons. Note, however, that the calculated cross sections have been normalized to 50% of the total oscillator strength, consistent with experiment, although the Drude model predicts 100% (Sec. VIII.D). The missing strength is thought to be primarily in volume plasma resonances not yet observed and in the ionization continuum. These effects are not contained in the simplified model presented here.

3. Interference effects between single-particle and plasmon states

The optical absorption spectra of small alkali clusters often have more structure than is predicted by the Drude model. Several calculations have shown that single-particle excitations often nearly coincide with the surface plasmon, resulting in a coupled state (Yannouleas *et al.*, 1989). Due to this coupling, the single-particle excitation may acquire considerable oscillator strength, so that the plasmon is fragmented (Sec. VIII.G). The fragmenting effect is well understood, but less attention has been paid to the actual line shape that results from these coupled states. Often the calculated stick spectrum resulting for the ground-state cluster shape is convolved with a smoothing function to mimic thermal broadening of the resonances. However, as shown by de Heer (1992), the coupling of the single-particle state with the surface plasmon may be quite sensitive to the instantaneous shape of the cluster, especially when the single-particle state is nearly degenerate with the surface plasmon. The thermal shape oscillations then give rise to line shapes that cannot be described by simple smoothing functions. This effect is illustrated below.

As before, both the single-particle and the surface-

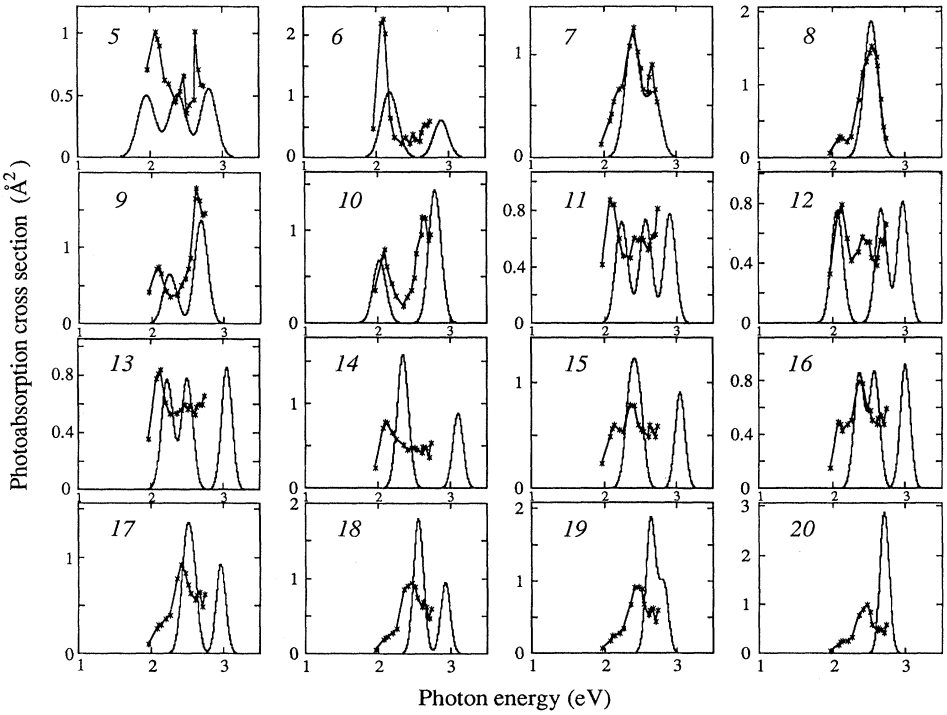

FIG. 57. Measured (*) and calculated photoabsorption spectra of Na_N clusters. The numbers in the figures correspond to the number of atoms in the cluster N. The spectra have been calculated using $r_s=4$ and $\delta=1.6$ a.u. for a temperature $T=300$ K.

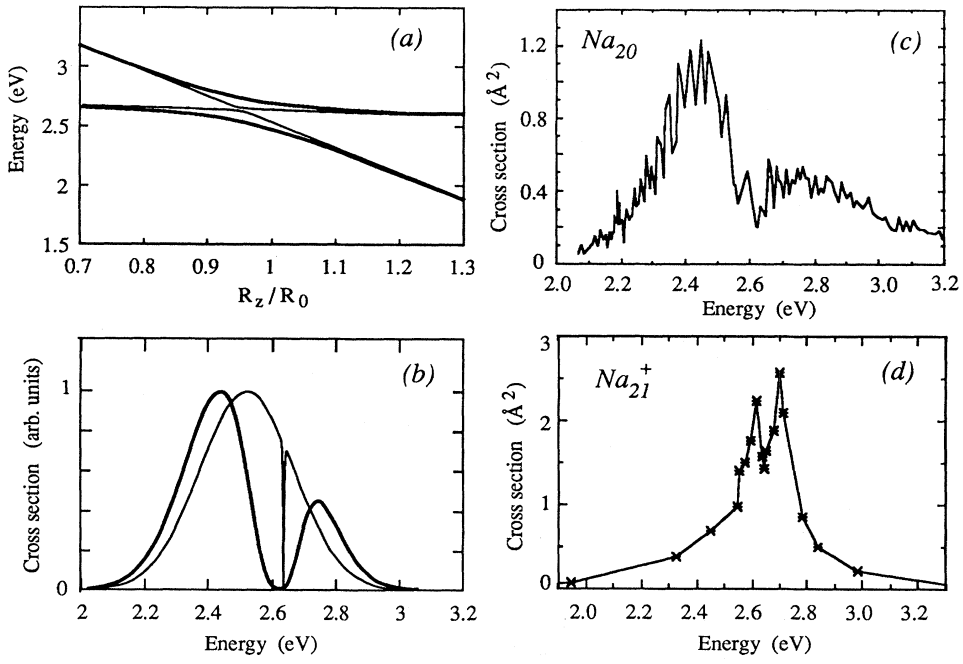

FIG. 58. Demonstration of the thermally broadened line shapes resulting from a single-particle/plasmon coupled state: (a) the energy eigenvalues as a function of the cluster shape parameter R_z, for weak couplings (fine line) and for stronger couplings (bold line); (b) the resulting photoabsorption spectrum for weak and strong coupling; (c) the experimental Na_{20} spectrum as an example of a coupled plasmon/single-particle spectrum, which clearly has an asymmetric profile, as predicted in the model; (d) experimental Na_{21}^+ plasmon, clearly showing a holelike feature (after Bréchignac, Cahuzac, Carlier, de Frutos, and Leygnier, 1992).

plasmon energies are a function of the shape, presented here as a normal coordinate R. In the idealized decoupled case, the surface-plasmon excited state $E_M(R)$ and the single-particle excited state $E_{sp}(R)$ may be written in lowest order as

$$E_M(R)=E_M(R_0)+K_M(R-R_0)\ ,$$
$$E_{sp}(R)=E_{sp}(R_0)+K_{sp}(R-R_0)\ , \tag{B12}$$

where (R_0-R) is a displacement from ground-state equilibrium shape R_0, and $E_M(R_0)$ and $E_{sp}(R_0)$ represent the vertical excitation energies from the ground-state equilibrium position.

If the coupling between the single-particle excitation and the surface plasmon is γ, the Hamiltonian that describes the coupled state is

$$H=\begin{bmatrix} E_M(R) & \gamma \\ \gamma & E_{sp}(R) \end{bmatrix}\ . \tag{B13}$$

An example of the eigenvalues $E_1(R)$ and $E_2(R)$ is shown in Fig. 58(a).

Assuming that in the uncoupled case the surface plasmon has all of the oscillator strength, the single-particle excitation acquires its oscillator strength by virtue of the coupling with the surface plasmon. Hence, writing the coupled wave functions (ϕ_1,ϕ_2) in terms of the decoupled ones (ϕ_M,ϕ_{sp}), we have

$$\phi_1(R)=a(R)\phi_M+b(R)\phi_{sp}\ ,$$
$$\phi_2(R)=c(R)\phi_M+d(R)\phi_{sp}\ . \tag{B14}$$

The coefficients are found by diagonalizing Eq. (B13). However, note that the oscillator strengths of the two states are $a^2(R)$ and $c^2(R)$, respectively. These are proportional to the photon absorption cross sections for the two states.

The total energy of the cluster in the ground state can be written as

$$E_{tot}(R)=E_{tot}(R_0)+K_{tot}(R_0-R)^2\ , \tag{B15}$$

from which the thermal distribution of R can be found as before. Hence the distribution of $a(R)$ and $c(R)$ is found, which can be transformed into $a(E_1)$ and $c(E_2)$. From these the photoabsorption cross sections are determined as explained above. Figure 58(b) shows an example of the resulting line shape for the coupled state.

An interesting feature is that when the plasmon/single-particle coupling is very weak [Figs. 58(a) and 58(b), thin line], the single-particle excitation is manifested as a rather sharp holelike feature in the Gaussian absorption profile. In fact, such features have been observed experimentally [Bréchignac, Cahuzac, Carlier, de Frutos, and Leygnier, 1992; see Fig. 58(d)]. For a slightly stronger coupling the hole broadens to give two separate peaks [Figs. 58(a) and 58(b), bold line], neither of which has a Gaussian shape. The experimental Na_{20} spectrum (Pollack *et al.*, 1991) is reproduced in Fig. 58(c) for comparison; it displays features corresponding with the model presented here.

The reason for the anomalous shapes is quite clear: the coupled state causes an energy gap in the excitation spectrum as a function of R [see Fig. 58(a)]. The strength of the coupling between the plasmon and the single-particle excitation is closely related to the width of the hole. Here the calculations have been simplified by assuming a normal coordinate R; however, the main features persist when using the parameters from the three-dimensional harmonic-oscillator model. In any case it is clear that the thermal line shapes of the single-particle/plasmon coupled excitation should be expected to be non-Gaussian. Alternatively, it may be concluded that, in general, highly asymmetric experimental line shapes indicate a coupled excitation.

APPENDIX C: PHOTOELECTRON SPECTRA AND THE ELLIPSOIDAL SHELL MODEL

Photoelectron spectra of alkali clusters have been obtained by Bowen's group (McHugh *et al.*, 1989; Eaton *et al.*, 1992) by measuring the energies of electrons that are photodetached from a cluster, as discussed in Sec. VII.A. They noticed a qualitative correspondence of the peaks in photoelectron spectra with the single-particle energy levels calculated in the ellipsoidal shell model and concluded that the photoelectron spectra in fact reflect the single-particle energy levels of the clusters. To find the thermal widths of the spectroscopic features, we proceed in an analogous way to that used for the plasmons.

The single-particle energies as a function of the cluster shape are given in Eq. (A7). It is instructive to consider K_8^-, which becomes K_8 upon ionization. The former is an ellipsoidal 9-electron system, which becomes a spherical 8-electron system when the electron occupying the highest occupied orbital is removed. (Note that the final equilibrium shape depends on which electron is removed.) The total-energy surfaces for the initial and final states are shown in Fig. 59, where the cluster undergoes quadrupole oscillations. The energy contour for 0.025 eV ($\approx$300 K) on the ground-state energy surface is highlighted to indicate the amplitude of the vibrations. Projecting this contour onto the final-state hypersurface gives an impression of the width of the photoelectron peak corresponding to this transition due to thermal quadrupole oscillations. A more qualitative evaluation follows.

Consider an electron in the configuration c_x,c_y,c_z [where $c_x=n_x+\frac{1}{2}$, etc.; see Eq. (A3)]. The variation of its energy with shape when the cluster undergoes a quadrupole oscillation (i.e., $R_xR_yR_z=R_0^3$) is given by

$$\delta E^{sp}_{quad}=\left[c_zR_y-\frac{c_x}{R_x^2}\right]\delta R_x+\left[c_zR_x-\frac{c_y}{R_y^2}\right]\delta R_y\ , \tag{C1a}$$

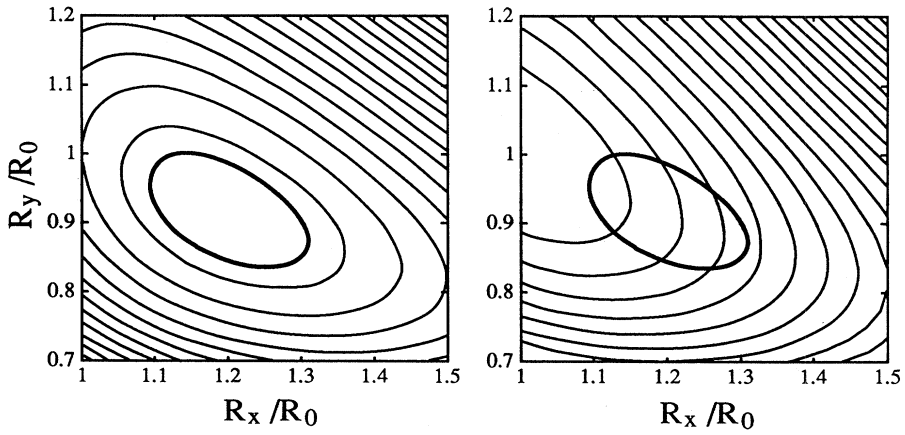

FIG. 59. Total-energy hypersurfaces for the quadrupole shape oscillations for the K_8^- cluster (left) and the K_8 cluster (right). The contours are spaced by 0.05 eV, and the bold contour corresponds to 0.025 eV ($\approx$300 K) of K_8^-. Note that when the bold contour is projected on the K_8 surface, it spans an energy range of about 0.15 eV, which corresponds to the thermal linewidth associated with this mode. The monopole contribution is comparable.

while for the monopole vibration (i.e., $\delta R_x/R_x = \delta R_y/R_y = \delta R_z/R_z$) it is

$$\delta E^{\rm sp}_{\rm mono} = \left[\frac{c_x}{R_x}+\frac{c_y}{R_y}+\frac{c_z}{R_z}\right]\frac{\delta R_x}{R_x}\ , \tag{C1b}$$

where for convenience $R_0 = h\omega_0 = 1$.

The photoelectron spectrum for this electron is determined analytically, as shown below, giving rise to a Gaussian line shape from combining the monopole and quadrupole contributions (see below).

Calculating the width of the single-particle excitations is essentially similar to deriving the plasmon shapes. For quadrupole vibrations, the variation in the single-particle energy level with $c_x c_y c_z$ is

$$\begin{aligned}\delta E_x^{\rm sp}(\delta R_x,\delta R_y) &= \left[c_z R_y - \frac{c_x}{R_x^2}\right]\delta R_x \\ &\quad + \left[c_z R_x - \frac{c_y}{R_z^2}\right]\delta R_y \\ &= a\,\delta R_x + b\,\delta R_y \\ &= (a^2+b^2)^{1/2} X\ ,\end{aligned} \tag{C2}$$

which defines the normal coordinate X. Likewise, the normal coordinate Y is defined by

$$Y = (-b\,\delta R_x + a\,\delta R_y)/(a^2+b^2)^{1/2}\ . \tag{C3}$$

The variation in the total energy expressed in these coordinates is

$$\delta E_{\rm tot}(X,Y) = \left[\alpha\frac{\gamma^2}{4\beta}\right]X^2 + \beta\left[Y+\frac{\gamma}{2\beta}X\right]^2\ , \tag{C4}$$

where

$$\begin{aligned}&\alpha = (p\cos^2\phi + q\sin^2\phi + r\sin\phi\cos\phi)\ ,\\ &\beta = (p\sin^2\phi + q\cos^2\phi - r\sin\phi\cos\phi)\ ,\\ &\gamma = -\{(p-q)\sin 2\phi + r\cos 2\phi\}\ ,\\ &p = C_x/R_x^3,\quad q = C_y/R_y^3,\quad r = C_z\ ,\\ &\phi = \arccos\{a/(a^2+b^2)^{1/2}\}\ ;\end{aligned}$$

proceeding as for the plasmons, one finds

$$K_{\rm quad} = \frac{\left[\alpha - \dfrac{\gamma^2}{4\beta}\right]}{(a^2+b^2)^{1/2}}\ . \tag{C5a}$$

The monopole contribution to the width is found to be

$$K_{\rm mono} = \frac{E_{\rm tot}}{E_{\rm sp}^2}\ , \tag{C5b}$$

where

$$E_{\rm sp} = \frac{c_x}{R_x}+\frac{c_y}{R_y}+\frac{c_z}{R_z}\ .$$

Combining the two contributions gives a Gaussian

$$\begin{aligned}&P(E) = K'\exp -K_{\rm tot}\left[\frac{E_{\rm sp}-E}{E_{\rm sp}}\right]^2\Big/kT\ ,\\ &K_{\rm tot}(x) = \{[K_{\rm mono}(x)]^{-1} + [K_{\rm quad}(x)]^{-1}\}^{-1}\ .\end{aligned} \tag{C6}$$

Thermal contributions from higher vibrational modes have been ignored but are expected to be less important.

The calculated spectra for potassium anions are shown in Fig. 60 together with the experimental data. No attempt has been made to estimate the transition strengths, which are taken to be constant for all transitions. The cluster temperature is taken to be 250 K, consistent with

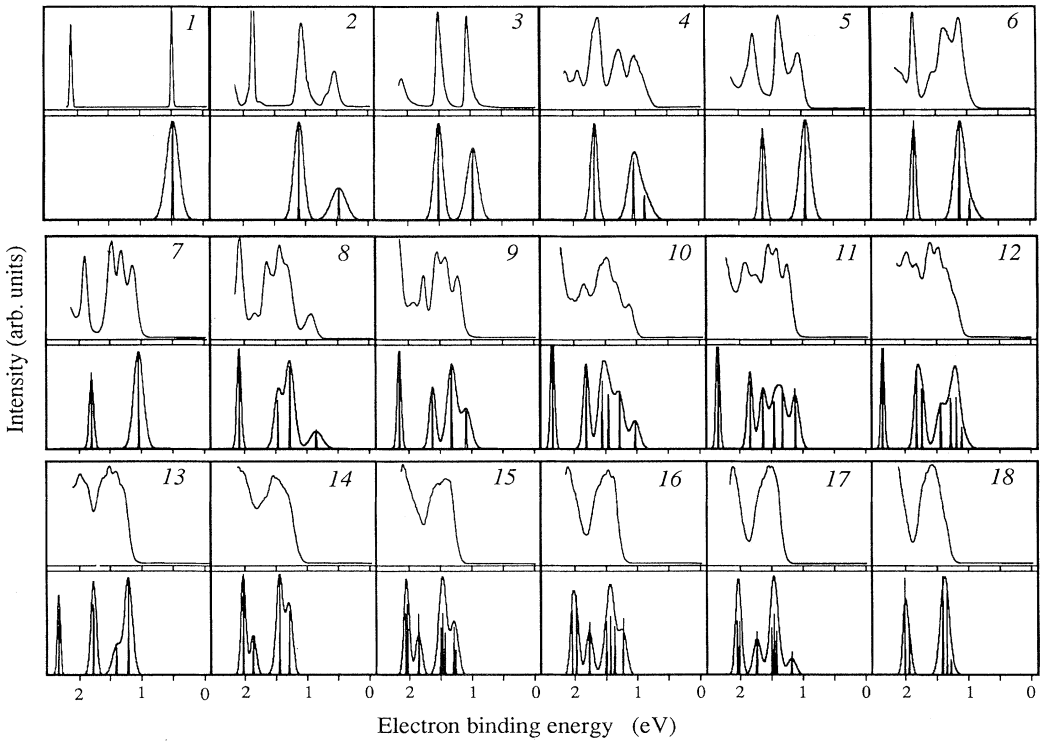

FIG. 60. Measured photoelectron spectra of K_N^- clusters (upper figures) from Eaton *et al.* (1992) and those measured in the three-dimensional oscillator model (lower figures). The numbers in the figures correspond to the number of atoms N. For the calculated spectra $rs=4.86$ and $\delta=1.6$ a.u., corresponding to potassium and $T=250$ K. The stick spectra have been calculated for $T=1$ K.

the expected cluster temperature. This model does not provide a value for the electron affinity; the spectra have been shifted so that the electron affinities correspond with the experimentally determined values. However, the semiclassical expression for the electron affinities (Sec. VI.E) may be used as well.

This model clearly gives a very reasonable description not only of the position of the peaks but also of their widths, although they are somewhat broader than experimentally observed. However, it is seen that in several cases the experimental spectra have more structure than calculated. For example, in this model the spherical 7^- cluster has one triply degenerate level due to the $1p$ levels; in the experimental spectrum, however, the three levels are resolved. This is due to crystal-field effects, as borne out by calculations that include the ionic cores (Fig. 54). It is important to note that the simple single-particle picture accounts for much of the observed structure and, in several cases, gives detailed agreement with experiment. Further structure is explained as being due to crystal-field effects. This suggests that higher-order excitations are of secondary importance for the spectra.

A further important point is that the linewidths are very reasonably reproduced, indicating that the elastic properties are probably reasonably well estimated. Although this was already clear from the calculated plasmon widths, here, in contrast with the plasmons, the monopole contribution is important and in some cases accounts (in lowest order) for all of the width.

REFERENCES

Alameddin, G., J. Hunter, D. Cameron, and M. M. Kappes, 1992, Chem. Phys. Lett. **192**, 122.

Anderson, J. B., 1974, in *Molecular Beams and Low Density Gas Dynamics,* edited by P. Wegener (Dekker, New York), p. 1.

Anderson, J. B., and J. B. Fenn, 1985, Phys. Fluids **8**, 780.

Ashcroft, N. W., and N. D. Mermin, 1976, *Solid State Physics* (Holt, Rinehart and Winston, New York).

Balian, R., and C. Bloch, 1972, Ann. Phys. (NY) **69**, 76, and earlier references quoted therein.

Baumert, T., C. Röttgermann, C. Rothenfusser, T. Thalweiser, V. Weiss, and G. Gerber, 1992, Phys. Rev. Lett. **69**, 1512.

Beck, D. E., 1984, Phys. Rev. B **30**, 6935.

Begemann, W., S. Deihöfer, K. H. Meiwes-Broer, and H. O. Lutz, 1986, Z. Phys. D **3**, 183.

Begemann, W., K. H. Meiwes-Broer, and H. O. Lutz, 1986, Phys. Rev. Lett. **56**, 2248.

Begemann, W., K. H. Meiwes-Broer, and H. O. Lutz, 1989, J. Phys. (Paris) **50**, C2-133.

Bergmann, T., H. Limberger, and T. P. Martin, 1988, Phys. Rev. Lett. **60**, 1767.

Bergmann, T., and T. P. Martin, 1989a, Rev. Sci. Instrum. **60**, 347.

Bergmann, T., and T. P. Martin, 1989b, Rev. Sci. Instrum. **60**,

792.
Berkowitz, J., 1979, *Photoabsorption, Photoionization and Photoelectron Spectroscopy* (Academic, New York).
Bernath, M., M. S. Hansen, P. F. Bortignon, and R. A. Broglia, 1992, unpublished
Berry, M. V., 1984, Proc. R. Soc. London Ser. A **392**, 45.
Bertsch, G. F., 1990, Comput. Phys. Commun. **60**, 247.
Bertsch, G. F., and W. Ekardt, 1985, Phys. Rev. B **32**, 7659.
Bertsch, G. F., N. Oberhofen, and S. Stringari, 1991, Z. Phys. D **20**, 123.
Bertsch, G. F., and D. Tománek, 1989, Phys. Rev. B **40**, 2749.
Beswick, J. A., and J. Jortner, 1990, Chem. Phys. Lett. **168**, 246.
Bhaskar, N. D., R. P. Frueholz, C. M. Klimcak, and R. A. Cook, 1987, Phys. Rev. B **36**, 4418.
Bjørnholm, S., J. Borggreen, O. Echt, K. Hansen, J. Pedersen, and H. D. Rasmussen, 1991, Z. Phys. D **19**, 47.
Blanc, J., M. Broyer, J. Chevaleyre, P. Dugourd, H. Kuhling, P. Labastie, M. Ulbricht, J. P. Wolf, and L. Wöste, 1991, Z. Phys. D **19**, 7.
Bohr, A., and B. Mottelson, 1975, *Nuclear Structure II* (Benjamin, New York).
Bonacic-Koutecky, V., P. Fantucci, and J. Koutecky, 1988, Phys. Rev. B **37**, 4369.
Bonacic-Koutecky, V., P. Fantucci, and J. Koutecky, 1989, J. Chem. Phys. **91**, 3792.
Bonacic-Koutecky, V., P. Fantucci, and J. Kouctecky, 1991, Chem. Rev. **91**, 1035.
Bondybey, V. E., and J. H. English, 1982, J. Chem. Phys. **76**, 2165.
Boustani, I., W. Pervestorf, P. Fantucci, V. Bonacic-Koutecky, and J. Koutecky, 1987, Phys. Rev. B **35**, 9437.
Brack, M., 1989, Phys. Rev. B **39**, 3533.
Brack, M., 1993, this issue, Rev. Mod. Phys. **65**, 677.
Brack, M., O. Genzken, and K. Hansen, 1991, Z. Phys. D **19**, 51.
Bréchignac, C., and P. Cahuzac, 1985, Chem. Phys. Lett. **117**, 365.
Bréchignac, C., P. Cahuzac, F. Carlier, M. de Frutos, and J. Leygnier, 1990, Phys. Rev. Lett. **64**, 2893.
Bréchignac, C., P. Cahuzac, F. Carlier, M. de Frutos, and J. Leygnier, 1992, Chem. Phys. Lett. **186**, 28.
Bréchignac, C., P. Cahuzac, F. Carlier, and J. Leygnier, 1989a, Chem. Phys. Lett. **164**, 433.
Bréchignac, C., P. Cahuzac, F. Carlier, and J. Leygnier, 1989b, Phys. Lett. **63**, 1368.
Bréchignac, C., P. Cahuzac, M. de Frutos, N. Kabaili, J. Leygnier, J. P. Roux, and A. Sarfati, 1992a, in *Physics and Chemistry of Finite Systems: From Clusters to Crystals,* NATO Advanced Study Institute, Series C, edited by P. Jena *et al.* (Kluwer Academic, Dordrecht/Boston), Vol. 2, p. 853.
Bréchignac, C., P. Cahuzac, M. de Frutos, N. Kabaili, J. Leygnier, J. P. Roux, and A. Sarfati, 1992b, Phys. Rev. Lett. **68**, 3916.
Bréchignac, C., P. Cahuzac, M. de Frutos, J. P. Roux, and K. Bowen, 1992, in *Physics and Chemistry of Finite Systems: From Clusters to Crystals,* NATO Advanced Study Institute, Series C, edited by P. Jena *et al.* (Kluwer Academic, Dordrecht/Boston), Vol. 1, p. 369.
Bréchignac, C., P. Cahuzac, J. Leygnier, R. Pflaum, J. P. Roux, and J. Weiner, 1989, Z. Phys. D **12**, 199.
Bréchignac, C., P. Cahuzac, J. Leygnier, and J. Weiner, 1989, J. Chem. Phys. **90**, 1492.
Broyer, M., 1989, Phys. Scripta, **T26**, 84.
Broyer, M., G. Delacrétaz, P. Labastie, R. L. Whetten, J. P. Wolf, and L. Wöste, 1986, Z. Phys. D **3**, 131.
Broyer, M., G. Delacrétaz, P. Labastie, J. P. Wolf, and L. Wöste, 1989, Phys. Rev. Lett. **57**, 1851.
Broyer, M., G. Delacrétaz, G. Q. Ni, R. L. Whetten, J. P. Wolf, and L. Wöste, 1989a, Phys. Rev. Lett. **62**, 2100.
Broyer, M., G. Delacrétaz, G. Q. Ni, R. L. Whetten, J. P. Wolf, and L. Wöste, 1989b, J. Chem. Phys. **90**, 843.
Car, R., and M. Parrinello, 1985, Phys. Rev. Lett. **55**, 2471.
Cheshnovsky, O., K. J. Taylor, J. Conceicao, and R. E. Smalley, 1990, Phys. Rev. Lett. **64**, 1785.
Cheshnovsky, O., S. H. Yang, C. L. Pettiette, M. J. Craycraft, and R. E. Smalley, 1987, Rev. Sci. Instrum. **58**, 2131.
Chou, M. Y., A. Cleland, and M. L. Cohen, 1984, Solid State Commun. **52**, 645.
Clemenger, K., 1985a, Phys. Rev. B **32**, 1359.
Clemenger, K., 1985, Ph.D. thesis (University of California, Berkeley).
Clemenger, K., 1991, Phys. Rev. B **44**, 12991.
Comisarow, M. B., and N. M. M. Nibbering, 1986, Int. J. Mass Spectrom. Ion Processes **72**, 1.
Cooper, J. W., 1962, Phys. Rev. **128**, 681.
Dam, N., and W. A. Saunders, 1991, Z. Phys. D **19**, 85.
de Heer, W. A., 1985, Ph.D. thesis (University of California, Berkeley).
de Heer, W. A., 1982, in *Clustering Phenomena in Atoms and Nuclei,* edited by M. Brenner, T. Lönnroth, and F. B. Malik (Springer, New York), p. 14.
de Heer, W. A., W. D. Knight, M. Y. Chou, and M. L. Cohen, 1987, in *Solid State Physics,* edited by H. Ehrenreich and D. Turnbull (Academic, New York), Vol. 40, p. 93.
de Heer, W. A., and P. Milani, 1990, Phys. Rev. Lett. **65**, 3356.
de Heer, W. A., and P. Milani, 1991, Rev. Sci. Instrum. **62**, 670.
de Heer, W. A., P. Milani, and A. Châtelain, 1989, Phys. Rev. Lett. **63**, 2834.
de Heer, W. A., K. Selby, V. Kresin, J. Masui, M. Vollmer, A. Chatelain, and W. D. Knight, 1987, Phys. Rev. Lett. **59**, 1805.
Delacrétaz, G., J. D. Ganiere, R. Monot, and L. Wöste, 1982, Appl. Phys. B **29**, 55.
Delacrétaz, G., E. R. Grant, R. L. Whetten, L. Wöste, and J. F. Zwanziger, 1986, Phys. Rev. Lett. **56**, 2598.
Delacrétaz, G., and L. Wöste, 1985, Surf. Sci. **156**, 770.
de Shalit, A., and H. Feshbach, 1974, *Theoretical Nuclear Physics* (Wiley, New York), Vol. 1.
Devaty, R. P., and A. J. Sievers, 1990, Phys. Rev. B **41**, 7421.
Dugourd, P. 1991, Ph.D. thesis (Université de Lyon).
Dugourd, P., D. Rayane, P. Labastie, B. Vezin, J. Chevaleyre, and M. Broyer, 1992, in *Physics and Chemistry and Finite Systems: From Clusters to Crystals,* NATO Advanced Study Institute, Series C, edited by P. Jena *et al.* (Kluwer Academic, Dordrecht/Boston), Vol. 1, p. 555.
Eaton, J. G., L. H. Kidder, H. W. Sarkas, K. M. McHugh, and K. Bowen, 1992, in *Physics and Chemistry of Finite Systems: From Clusters to Crystals,* NATO Advanced Study Institute, Series C, edited by P. Jena *et al.* (Kluwer Academic, Dordrecht/Boston), Vol. I, p. 493.
Echt, O., K. Sattler, and E. Recknagel, 1981, Phys. Rev. Lett. **47**, 1121.
Ehrenreich, H., and H. R. Philipp, 1962, Phys. Rev. B **128**, 1622.
Ekardt, W., 1984a, Phys. Rev. Lett. **52**, 1925.
Ekardt, W., 1984b, Phys. Rev. B **29**, 1558.
Ekardt, W., 1985a, Phys. Rev. B **31**, 6360.
Ekardt, W., 1985b, Phys. Rev. B **32**, 1961.
Ekardt, W., and Z. Penzar, 1988, Phys. Rev. B **38**, 4273.

Ekardt, W., and Z. Penzar, 1991, Phys. Rev. B **43**, 1322.
Ekardt, W., Z. Penzar, and A. Rubio, 1990, Phys. Rev. B **42**, 5040.
Engelking, P. C., 1987, J. Chem. Phys. **87**, 936.
Ernst, W., and S. Rakowsky, 1993, Z. Phys. D **26**, 137.
Fallgren, H., and T. P. Martin, 1990, Chem. Phys. Lett. **168**, 233.
Fayet, P., J. P. Wolf, and L. Wöste, 1986, Phys. Rev. B **33**, 6792.
Ganteför, G., M. Gausa, K. H. Meiwes-Broer, and H. O. Lutz, 1988a, Faraday Discuss. Chem. Soc. **86**, 197.
Ganteför, G., M. Gausa, K. H. Meiwes-Broer, and H. O. Lutz, 1988b, Z. Phys. D **9**, 253.
Ganteför, G., K. H. Meiwes-Broer, and H. O. Lutz, 1988, Phys. Rev. A **37**, 2716.
Ganteför, G., H. R. Siekmann, H. Ol. Lutz, and K. H. Meiwes-Broer, 1990, Chem. Phys. Lett. **165**, 293.
Gerber, G., T. Baumert, T. Thalweiser, and V. Weiss, 1993, Z. Phys. D **26**, 131.
Gerber, W. H., and E. J. Schumacher, 1978, J. Chem. Phys. **69**, 1962.
Göhlich, H., T. Lange, T. Bergmann, and T. P. Martin, 1990, Phys. Rev. Lett. **65**, 748.
Guyon, P. H., and J. Berkowitz, 1971, J. Chem. Phys. **54**, 1814.
Hagena, O. F., 1991, Z. Phys. D **20**, 425.
Hall, W. D., and J. C. Zorn, 1974, Phys. Rev. A **10**, 1141.
Harbich, W. A., S. Fredrigo, and J. Buttet, 1992, Chem. Phys. Lett. **195**, 613.
Herrmann, A., E. Schumacher, and L. Wöste, 1978, J. Chem. Phys. **68**, 2327.
Herzberg, G., 1966, *Electronic Spectra of Polyatomic Molecules* (Van Nostrand Reinhold, New York).
Hill, D. L., and J. A. Wheeler, 1953, Phys. Rev. **89**, 1102.
Homer, M., J. L. Persson, E. C. Honea, and R. L. Whetten, 1992, Z. Phys. D **22**, 441.
Homer, M., *et al.*, 1993, private communication.
Honea, E. C., M. L. Homer, J. L. Persson, and R. L. Whetten, 1991, Chem. Phys. Lett. **171**, 147.
Inagaki, T., L. C. Emerson, E. T. Arakawa, and M. W. William, 1976, Phys. Rev. B **13**, 2305.
ISSPIC* 1, 1977, J. Phys. (Orsay) **38**, C2.
ISSPIC 2, 1981, Surf. Sci. **106**.
ISSPIC 3, 1985, Surf. Sci. **156**.
ISSPIC 4, 1989, Z. Phys. D **12**.
ISSPIC 5, 1991, Z. Phys. D **19**, 20
ISSPIC 6, 1993, Z. Phys. D (in press).
Jackschath, C., I. Rabin, and W. Schulze, 1992, Z. Phys. D **22**, 517.
Jackson, J. D., 1975, *Electromagnetic Fields and Waves,* 2nd Ed. (Wiley, New York).
Jahn, H. A., and E. Teller, 1937, Proc. R. Soc. London Ser. A **161**, 220.
Jarrold, M. F., and J. E. Bower, 1992, J. Chem. Phys. **96**, 9180.
Jarrold, M. F., J. E. Bower, and J. S. Krauss, 1987, J. Chem. Phys. **86**, 3876.
Jarrold, M. F., and V. A. Constant, 1991, Phys. Rev. Lett. **67**, 2994.
Jarrold, M. F., U. Ray, J. E. Bower, and K. M. Creegan, 1990, J. Chem. Soc. Faraday Trans. **86**, 2537.
Jena, P., S. N. Khanna, and B. K. Rao, 1992, Eds., *Physics and Chemistry of Finite Systems: From Clusters to Crystals,* NATO Advanced Study Institute, Series C, Vol. 374 (Kluwer, Dordrecht).
Jena, P., B. K. Rao, and S. N. Khanna, 1987, Eds., *Physics and Chemistry of Small Clusters,* NATO, ASI Series B, Vol. 158 (Plenum, New York).
Kappes, M. M., R. W. Kunz, and E. Schumacher, 1982, Chem. Phys. Lett. **91**, 413.
Kappes, M. M., M. Schar, U. Röthlisberger, C. Yeretzian, and E. Schumacher, 1988, Chem. Phys. Lett. **143**, 251.
Katakuse, I., T. Ichihara, Y. Fujita, T. Matsuo, T. Sakurai, and H. Matsuda, 1985, Int. J. Mass Spectrom. Ion Processes **67**, 229.
Katakuse, I., T. Ichihara, Y. Fujita, T. Matsuo, T. Sakurai, and H. Matsuda, 1986, Int. J. Mass Spectrom. Ion Processes **69**, 109.
Katakuse, I., H. Ito, and T. Ichihara, 1990, Int. J. Mass. Spectrom. Ion Processes **97**, 47.
Kawabata, A., and R. Kubo, 1966, J. Phys. Soc. Jpn. **21**, 1765.
Kawai, R., and J. H. Weare, 1990, Phys. Rev. Lett. **65**, 80.
Kittel, C., 1976, *Introduction to Solid State Physics,* 5th Ed. (Wiley, New York).
Klots, C. E., 1985, J. Chem. Phys. **83**, 854.
Klots, C. E., 1988, J. Chem. Phys. **92**, 5864.
Klots, C. E., 1991, Z. Phys. D **20**, 105.
Knight, W. D., K. Clemenger, W. A. de Heer, W. A. Saunders, M. Y. Chou, and M. L. Cohen, 1984, Phys. Rev. Lett. **52**, 2141; **53**, 510(E).
Knight, W. D., K. Clemenger, W. A. de Heer, and W. A. Saunders, 1985a, Phys. Rev. B **31**, 2539.
Knight, W. D., W. A. de Heer, K. Clemenger, and W. A. Saunders, 1985b, Solid State Commun. **53**, 445.
Köller, L., J. Tiggesbäumker, and K. H. Meiwes-Broer, 1992, unpublished.
Kreibig, U., 1970, Z. Phys. **234**, 307.
Kreibig, U., and L. Genzel, 1985, Surf. Sci. **156**, 678.
Kreibig, U., and P. Zacharias, 1970, Z. Phys. **231**, 128.
Kresin, V., 1989a, Phys. Rev. B **39**, 3042.
Kresin, V., 1989b, Phys. Rev. B **40**, 12 507.
Kresin, V., 1990, Phys. Rev. B **42**, 3247.
Kresin, V., 1992, Phys. Rep. **220**, 1.
Kruit, P., and F. H. Read, 1983, J. Phys. E **16**, 313.
Kubo, R., 1962, J. Phys. Soc. Jpn. **17**, 975.
Lang, N. D., and W. Kohn, 1971, Phys. Rev. B **3**, 1215.
Lang, N. D., and W. Kohn, 1973, Phys. Rev. B **7**, 3541.
Larson, R. A., S. K. Neoh, and D. R. Herschbach, 1984, Rev. Sci. Instrum. **45**, 1511.
Lauritsch, G., P.-G. Reinhard, J. Meyer, and M. Brack, 1991, Phys. Lett. A **160**, 179.
Leopold, D. G., J. H. Ho, and W. C. Lineberger, 1987, J. Chem. Phys. **86**, 1715.
Lermé, J., M. Pellarin, J. L. Vialle, B. Baguenard, and M. Broyer, 1992, Phys. Rev. Lett. **68**, 2818.
Limberger, H. G., and T. P. Martin, 1988, J. Phys. Chem. **90**, 2979.
Lindsay, D. M., Y. Wang and T. F. George, 1987, J. Chem. Phys. **86**, 3500.
Lipparini, E., and A. Vittori, 1990, Z. Phys. D **17**, 57.
Longuet-Higgins, H. C., U. Öpic, M. H. L. Pryce, F. R. S. Sack, and R. A. Sack, 1958, Proc. R. Soc. London Ser. A **244**, 1.
Longuet-Higgins, H. C., 1961, Adv. Spectrosc. **2**, 429.
Mackay, A. L., 1962, Acta Crystallogr. **15**, 1916.
Maisse, L. I., and R. Glang, 1970, *Handbook of Thin Film Technology* (McGraw-Hill, New York), Chap. 1.

*International Symposiun on Small Particles and Inorganic Clusters.

Makov, G., A. Nitzan, and L. E. Brus, 1988, J. Chem. Phys. **88**, 5076.
Mandich, M. L., and W. D. Reents, 1989, Z. Phys. D **12**, 555.
Markus, R. A., 1952, J. Chem. Phys. **20**, 364.
Martin, T. P., and T. Bergmann, 1989, J. Chem. Phys. **90**, 6664.
Martin, T. P., T. Bergmann, H. Göhlich, and T. Lange, 1990a, Chem. Phys. Lett. **172**, 209.
Martin, T. P., T. Bergmann, H. Göhlich, and T. Lange, 1990b, Phys. Rev. Lett. **65**, 748.
Martin, T. P., T. Bergmann, H. Göhlich, and T. Lange, 1991a, Chem. Phys. Lett. **176**, 343.
Martin, T. P., T. Bergmann, H. Göhlich, and T. Lange, 1991b, Z. Phys. D **19**, 25.
Martin, T. P., T. Bergmann, and N. Mallnowski, 1990, J. Chem. Soc. Faraday Trans. **86**, 2489.
Martin, T. P., S. Bjørnholm, J. Borggreen, C. Bréchignac, P. Cahuzac, K. Hansen, and J. Pedersen, 1991, Chem. Phys. Lett. **186**, 53.
Martin, T. P., U. Naher, T. Bergmann, H. Göhlich, and T. Lange, 1991, Chem. Phys. Lett. **183**, 119.
Martin, T. P., U. Näher, H. Göhlich, and T. Lange, 1992, Chem. Phys. Lett. **196**, 113.
Martins, J. L., J. Buttet, and R. Car, 1985, Surf. Sci. **156**, 649.
Martins, J. L., R. Car, and J. Buttet, 1981, Surf. Sci. **106**, 265.
McHugh, K. M., J. G. Eaton, G. H. Lee, H. W. Sarkas, L. H. Kidder, J. T. Snodgrass, M. R. Manaa, and K. H. Bowen, 1989, J. Chem. Phys. **91**, 3792.
Meiwes-Broer, K. H., 1993, in *Advances in Metal and Semiconductor Clusters,* edited by M. Duncan (JAI, Greenwich), Vol. 1, p. 37.
Mie, G., 1908, Ann. Phys. (Leipzig) **25**, 377.
Milani, P., and W. A. de Heer, 1990, Rev. Sci. Instrum. **61**, 1835.
Milani, P., and W. A. de Heer, 1991, Phys. Rev. B **44**, 8346.
Milani, P., W. A. de Heer, and A. Chatelain, 1991, Z. Phys. D **19**, 133.
Milani, P., I. Moullet, and W. A. de Heer, 1990, Phys. Rev. A **42**, 5150.
Miller, T. M., and B. Bederson, 1977, in *Advances in Atomic and Molecular Physics,* edited by D. R. Bates and I. Estermann (Academic Press, New York), Vol. 13, p. 1.
Moullet, I., and J. L. Martins, 1990, J. Chem. Phys. **92**, 527.
Moullet, I., J. L. Martins, F. Reuse, and J. Buttet, 1990, Phys. Rev. B **42**, 11 598.
Nakamura, M., Y. Ishii, A. Tamura, and S. Sugano, 1991, Z. Phys. D **19**, 153.
Nilsson, S. G., 1955, K. Dan. Vidensk. Selsk. Mat. Fys. Medd. **29**, No. 16.
Nishioka, H., K. Hansen, and B. R. Mottelson, 1990, Phys. Rev. B **42**, 9377.
Pacheco, J. M., and R. A. Broglia, 1989, Phys. Rev. Lett. **62**, 1400.
Pacheco, J. M., R. A. Broglia, and B. R. Mottelson, 1991, Z. Phys. D **21**, 289.
Paul, W., H. P. Reinhard, and U. von Zahn, 1958, Z. Phys. **152**, 143.
Pedersen, J., S. Bjørnholm, J. Borggreen, K. Hansen, T. P. Martin, and H. D. Rasmussen, 1991, Nature **353**, 733.
Pellarin, M., B. Baguenard, M. Broyer, J. Lermé, and J. L. de Vialle, 1992, ISSPIC 6 book of abstracts, abstract T88.
Pellarin, M., B. Baguenard, M. Broyer, J. Lermé, and J. L. de Vialle, 1993, Z. Phys. D (Suppl.) **26**, 137.
Penzar, Z., and W. Ekardt, 1991, Z. Phys. D **19**, 109, and references therein.
Perdew, J. P., 1988, Phys. Rev. B **37**, 6175.
Persson, J. L., 1991, Ph.D. thesis (University of California, Los Angeles).
Persson, J. L., R. L. Whetten, H.-P. Cheng, and R. S. Berry, 1991, Chem. Phys. Lett. **186**, 215.
Pettiette, C. L., S. H. Yang, M. J. Craycraft, J. Conceicao, R. T. Laaksonen, O. Cheshnovsky, and R. E. Smalley, 1988, J. Chem. Phys. **88**, 5377.
Pines, D., 1964, *Elementary Excitations in Solids* (Benjamin, New York).
Pollack, S., C. R. C. Wang, and M. M. Kappes, 1991, J. Chem. Phys. **94**, 2496.
Preston, M. A., and R. K. Bhaduri, 1975, *Structure of the Nucleus* (Addison-Wesley, Reading, MA).
Puska, M. J., R. M. Nieminen, and M. Manninen, 1985, Phys. Rev. B **31**, 3486.
Rabin, I., C. Jackschath, and W. Schulze, 1991, Z. Phys. D **19**, 153.
Rademann, K., 1989, Ber. Bunsenges. Phys. Chem. **95**, 563.
Rademann, K., B. Kaiser, U. Even, and F. Hensel, 1987, Phys. Rev. Lett. **59**, 2319.
Raether, H., 1965, in *Springer Tracts in Modern Physics,* edited by G. Höhler, Vol. 38 (Springer-Verlag, Berlin), p. 84.
Ramsey, N. F., 1969, *Molecular Beams* (Clarendon, Oxford).
Ray, U., M. F. Jarrold, J. E. Bower, and J. S. Krauss, 1989, J. Chem. Phys. **91**, 2912.
Rayane, D., P. Melinon, B. Tribollet, B. Chabaud, A. Hoareau, and M. Broyer, 1989, J. Chem. Phys. **91**, 3100.
Reinhard, P.-G., M. Brack, and O. Genzken, 1990, Phys. Rev. A **41**, 5568.
Reuse, F., S. N. Khanna, V. de Coulon, and J. Buttet, 1990, Phys. Rev. B **41**, 11743.
Rice, O. K., and H. G. Ramsperger, 1927, J. Am. Chem. Soc. **49**, 1672.
Riley, S. J., E. K. Parks, C. R. Mao, L. G. Pobo, and S. Wexler, 1982, J. Phys. Chem. **86**, 3911.
Robbins, E. J., R. E. Leckenby, and P. Willis, 1967, Adv. Phys. **16**, 739.
Röthlisberger, U., and W. Andreoni, 1991, J. Chem. Phys. **94**, 8129.
Rubio, A., L. C. Balbas, and J. A. Alonso, 1990, Solid State Commun. **75**, 139.
Rubio, A., L. C. Balbas, and J. A. Alonso, 1991, Z. Phys. D **19**, 93.
Saito, Y., K. Minami, T. Ishida, and T. Noda, 1989, Z. Phys. D **11**, 87.
Sattler, K., J. Mühlbach, and E. Recknagel, 1980, Phys. Rev. Lett. **45**, 821.
Saunders, W. A., 1986a, Proc. SPIE Int. Soc. Opt. Eng.
Saunders, W. A., 1986b, Ph.D. thesis (University of California, Berkeley).
Saunders, W. A., 1990, Phys. Rev. Lett. **64**, 3046.
Saunders, W. A., K. Clemenger, W. A. de Heer, and W. D. Knight, 1985, Phys. Rev. B **32**, 1466.
Saunders, W. A., and N. Dam, 1991, Z. Phys. D **20**, 111.
Saunders, W. A., and S. Fredrigo, 1989, Chem. Phys. Lett. **156**, 14.
Schriver, K. E., J. L. Persson, E. C. Honea, and R. L. Whetten, 1990, Phys. Rev. Lett. **64**, 2539.
Schulze, W., B. Winter, and I. Goldenfeld, 1988, Phys. Rev. B **38**, 2937.
Scoles, G., 1988, *Atomic and Molecular Beam Methods* (Oxford University Press, New York), Vol. 1.
Seidl, M., K. H. Meiwes-Broer, and M. Brack, 1991a, J. Chem.

Phys. **95**, 1295.
Seidl, M., M. E. Spina, and M. Brack, 1991b, Z. Phys. D **19**, 101.
Selby, K., V. Kresin, J. Masui, M. Vollmer, W. A. de Heer, A. Scheidemann, and W. D. Knight, 1991, Phys. Rev. B **43**, 4565.
Selby, K., M. Vollmer, J. Masui, V. Kresin, W. A. de Heer, and W. D. Knight, 1989, Phys. Rev. B **40**, 5417.
Siekmann, H. R., C. Luder, J. Fachrmann, H. O. Lutz, and K. H. Meiwes-Broer, 1991, Z. Phys. D **20**, 417.
Smalley, R. E., 1983, Laser Chem. **2**, 167.
Smith, N. V., C. T. Chen, and M. Weinert, 1989, Phys. Rev. B **40**, 7565.
Snider, D. R., and R. S. Sorbello, 1983, Phys. Rev. B **28**, 5702.
Stoner, E. C., 1945, Philos. Mag. **36**, 803.
Sudraud, P., C. Collinex, and J. van der Walle, 1979, J. Phys. D **13**, L203.
Sugano, S., 1991, *Microcluster Physics* (Springer, Berlin).
Taylor, K. J., C. L. Pettiette-Hall, O. Cheshnovsky, and R. E. Smalley, 1992, J. Chem. Phys. **96**, 3319.
Tiggesbäumker, J., L. Köller, H. O. Lutz, and K. H. Meiwes-Broer, 1992, Chem. Phys. Lett. **190**, 42.
Upton, T. H., 1986, Phys. Rev. Lett. **56**, 2168.
Upton, T. H., 1987, J. Chem. Phys. **86**, 7052.
von Halden, G., M. T. Hsu, P. R. Kemper, and M. T. Bowers, 1991, J. Chem. Phys. **95**, 3832.
Wagner, A., and T. M. Hall, 1979, J. Vac. Sci. Technol. **16**, 1871.
Wanczek, K. P., 1984, Int. J. Mass Spectrom. Ion Processes **60**, 11.
Wang, C. R. C., S. Pollack, and M. M. Kappes, 1990, Chem. Phys. Lett. **166**, 26.
Wang, Y., T. F. George, D. M. Lindsay, and A. C. Beri, 1987, J. Chem. Phys. **86**, 3493.
Watanabe, K., 1954, J. Chem. Phys. **9**, 1564.
Weisskopf, V., 1937, Phys. Rev. **52**, 295.
Whetten, R. L., *et al.*, 1992, unpublished.
Wigner, E. P., 1948, Phys. Rev. **73**, 1002.
Wiley, W. C., and I. H. McLaren, 1955, Rev. Sci. Instrum. **26**, 1150.
Wood, D. M., 1981, Phys. Rev. Lett. **46**, 749.
Wood, D. M., and N. Ashcroft, 1982, Phys. Rev. B **25**, 6255.
Yannouleas, C., 1992, Chem. Phys. Lett. **193**, 587.
Yannouleas, C., and R. A. Broglia, 1991a, Phys. Rev. A **44**, 5793.
Yannouleas, C., and R. A. Broglia, 1991b, Europhys. Lett. **15**, 843.
Yannouleas, C., and R. A. Broglia, 1992, Ann. Phys. (NY) **217**, 105.
Yannouleas, C., R. A. Broglia, M. Brack, and P. F. Bortignon, 1989, Phys. Rev. Lett. **63**, 255.
Yannouleas, C., J. M. Pachecco, and R. A. Broglia, 1990, Phys. Rev. B **41**, 6088.